

Optical Coherence Tomography for Material Characterization

Ping LIU

基于光学相干断层扫描的材料无损检测

刘 平

Optical Coherence Tomography for Material Characterization

Proefschrift

ter verkrijging van de graad van doctor
aan de Technische Universiteit Delft,
op gezag van de Rector Magnificus prof. ir. K.C.A.M. Luyben,
voorzitter van het College voor Promoties,
in het openbaar te verdedigen op Maandag 8 December 2014 om 10:00 uur

door

Ping LIU

Master of Science in Mechanical Engineering,
Nanjing University of Aeronautics and Astronautics, China
geboren te Jiangsu, China

Dit proefschrift is goedgekeurd door de promotor:

Prof. dr. ir. R. Benedictus

Copromotor: Dr. R. M. Groves

Samenstelling promotiecommissie:

Rector Magnificus

Prof. dr. ir. R. Benedictus

Dr. R. M. Groves

Prof. dr hab. P. Targowski

Prof. dr. A.G.J.M. van Leeuwen

Prof. dr. ir. Lucas J. van Vliet

Prof. dr. ir. S. van der Zwaag

Dr. P. H. Tomlins

voorzitter

Technische Universiteit Delft, promotor

Technische Universiteit Delft, copromotor

Nicolaus Copernicus University

Universiteit van Amsterdam

Technische Universiteit Delft

Technische Universiteit Delft

Queen Mary University of London

ISBN: 978-94-6186-393-5

Copyright © 2014 by Ping Liu

All rights reserved. No part of the material protected by the copyright notice may be reproduced or utilized in any form or by any means, electronic or mechanical, including photocopying, recording or by any information storage and retrieval system, without the prior permission of the author.

Printed in the Netherlands by Uitgeverij BOXPress, 's-Hertogenbosch

To my Family

Summary

Optical coherence tomography (OCT) is a non-invasive, contactless and high resolution imaging method, which allows the reconstruction of two or three dimensional depth-resolved images in turbid media. In the past 20 years, OCT has been extensively developed in the field of biomedical diagnostics, while OCT in the non-destructive testing (NDT) field is lagging far behind.

The aim of this thesis is to use OCT as a novel NDT technique for material structure characterization and damage detection. Besides an overview of the OCT fundamentals and developments, the thesis is mainly driven by three tasks: instrument design, signal processing, and applications.

An integrated OCT system working at a wavelength of 1550 nm has been built. It combines time domain (TD) and Fourier domain (FD) OCT to make the both types of measurement available in one instrument. TD-OCT has the advantage of a large A-scan range and high SNR, while FD-OCT system has tremendous superiority in fast imaging due to no movement of the reference mirror. These two kinds of measurement can be implemented based on the user request in the developed hybrid OCT system, e.g. improved imaging depth or speed.

In TD-OCT, the envelope detector was selected as the ideal method for the demodulation of each axial signal. A bandpass filter and 2D median filter are applied before and after demodulation, respectively, to reduce OCT system and speckle noise. In FD-OCT, raw data was first processed to remove the influence from the optical source and dark noise of the CCD detectors. It was then linearly resampled to convert to evenly spaced intervals of wavenumber, instead of wavelength. With an inverse Fourier transform, one depth profile was recovered and a cross-sectional image was constructed by accumulating a series of depth profiles. The quality of cross-sectional images can be further improved by merging multiple images with different pathlength offsets.

The application of the designed OCT system was mainly focused on glass fiber composites and the microstructure of the specimens was displayed by either cross-sectional or volumetric images. Special attention was given to delamination growth in a glass fiber composite for wind turbine blade applications. The glass fiber composite was tested by incremental loading. Volumetric images obtained by OCT were further processed to reconstruct 3D crack surface profiles, from which a full field view of the delamination crack was given, providing substantial information for the study of crack growth in the composites. Additionally, the study explored the use of optical coherence elastography (OCE) for the deformation measurement of glass fiber composites, for the first time to the best of our knowledge. The developed OCE system based on speckle tracking was first evaluated by a test of ridge body translation. Then experiments were implemented for a set of glass fiber composites under tensile testing and three point bending. The results show that OCE can measure the internal displacements of a glass fiber composite in the range from a few micrometers to hundreds of micrometers.

Besides, other applications are also presented in the thesis. These include defects and thickness measurement of polymer coating and the microstructure characterization of a wooden-panel painting. The results show the designed OCT system also has high potential for these alternative applications. Recommendations for further improvement to the OCT design and the applications are presented at the end of the thesis.

Contents

Summary	vii
1 Introduction	1
1.1 Non-destructive Testing	1
1.2 Research Motivation	3
1.3 Thesis Outline	6
References	8
2 Fundamentals and Developments of Optical Coherence Tomography	13
2.1 Introduction	13
2.2 Fundamentals of Optical Coherence Tomography	14
2.2.1 Time-domain Optical Coherence Tomography	14
2.2.2 Fourier-domain Optical Coherence Tomography	17
2.2.3 Resolution of Optical Coherence Tomography	19
2.3 Performance Comparison of TD-OCT and FD-OCT	21
2.3.1 General Performance	22
2.3.2 Spectral Requirement	23
2.3.3 Signal to Noise Ratio	24
2.4 Developments of Optical Coherence Tomography	26
2.4.1 Light Source	26
2.4.2 OCT Scanners	28
2.4.3 Swept Source Optical Coherence Tomography	30
2.4.4 Full Field Optical Coherence Tomography	31
2.4.5 New Imaging Concepts	32
2.5 Discussion and Conclusions	33
References	36

3	Development of a Hybrid OCT System	43
3.1	Introduction	43
3.2	System Overview	43
3.3	Detail of components	46
3.3.1	Light Source	46
3.3.2	Optical Fiber	48
3.3.3	Interferometer	49
3.3.4	Polarizer and Polarization Maintaining Fiber	50
3.3.5	Circulator and Optical Switch	51
3.3.6	Collimator and Focusing Lens	53
3.3.7	Optical Delay Line and Reflector	53
3.3.8	Balanced Detector and DAQ Board	54
3.3.9	Spectrometer	56
3.3.10	Translation Stages	58
3.4	Instrument Control Software	60
3.5	Conclusions	61
	References	61
4	Design of Signal Processing	65
4.1	Introduction	65
4.2	Signal processing in TD-OCT	66
4.2.1	Bandpass Filter	67
4.2.2	Demodulation	69
4.2.3	Imaging smoothing	74
4.3	Signal processing in FD-OCT	75
4.3.1	Reflection-mode measurement	76
4.3.2	Resampling	77
4.3.3	Inverse Fourier transform	78
4.3.4	Axial scan smoothing	78
4.4	Image Display	80
4.5	System Evaluation	81
4.5.1	A-scan Accuracy and Linearity	81

4.5.2	Signal to Noise Ratio	82
4.6	Discussion	84
4.7	Conclusions	85
	References	86
5	OCT for Monitoring the Delamination Growth in Glass Fiber Composite	89
5.1	Introduction	89
5.2	Sample Construction	90
5.3	Experimental Setup	91
5.4	Results	92
5.4.1	Static Test	92
5.4.2	Incremental Loading Test	95
5.5	Discussion	100
5.6	Conclusions	102
	References	102
6	OCT Elastography for Measuring the Deformation within Glass Fiber Composite	105
6.1	Introduction	105
6.2	Methods	107
6.2.1	Experimental Setup	107
6.2.2	Image Processing Techniques	108
6.3	Results	109
6.3.1	Rigid Body Translation	109
6.3.2	Tensile Test	111
6.3.3	Three Point Bending	114
6.4	Discussion	116
6.5	Conclusions	118
	References	118
7	Further Non-destructive Testing Applications	123
7.1	Introduction	123
7.2	Defects and Thickness Measurement of Polymer Coatings	124
7.2.1	Introduction	124

7.2.2	Detection and measurement of microcracks	124
7.2.3	Thickness Measurement.....	126
7.2.4	Discussion	127
7.3	Study of Front and Back Faces of a Wooden Panel Painting	129
7.3.1	Introduction.....	129
7.3.2	Sample Description	129
7.3.3	Front Face Characterization	131
7.3.4	Back Face Characterization	133
7.3.5	Discussion	135
7.4	Conclusions.....	137
	References	137
8	Conclusions and Recommendations.....	141
8.1	Conclusions.....	141
8.1.1	Conclusions from Instrument Design	141
8.1.2	Conclusions from Signal Processing	142
8.1.3	Conclusions from Applications.....	142
8.2	Recommendations.....	144
8.2.1	Recommendations for Instrument Design	144
8.2.2	Recommendations for Signal Processing.....	144
8.2.3	Recommendations for Applications.....	145
	Samenvatting.....	147
	Acknowledgements	149
	About the Author.....	151
	List of Publications.....	153

1

Introduction

1.1 Non-destructive Testing

Materials are evolving faster today than at any time in history. Radical material advances enable engineers to improve the performance of existing products and to create new products that will make our lives safer, more convenient or more sustainable [1]. For example, composites, a mixture of two or more different materials, are increasingly applied in aerospace and wind energy industries for their exceptional strength and stiffness-to-density ratios. In the newest commercial aircrafts such as Airbus A350XWB [2], up to 53% by weight of the airframe is constructed by composite materials, which, compared with a metallic fuselage, contributes to lower overall aircraft weight and higher fuel efficiency, along with reduced corrosion and fatigue, as well as lower maintenance costs. Composite materials are also boosting the development of wind energy that currently accounts for 3.5 % of the world's electricity demand and grows rapidly at 16% per annum [3]. In the Netherlands, wind turbines have been installed with a total capacity of 2, 693 MW at the end of 2013 [4]. In 2020, this should be further developed to 6,000 MW onshore and 6,000 MW of offshore wind energy [5], which will cover nearly one third of total electricity consumption in the Netherlands. Wind turbine blades are extensively manufactured with composites that can bear gravity and wind loadings for long life cycle due to their low density and high stiffness [6].

During the development of materials, both scientists and engineers need to know what properties each material has and how they might be changed. Only very rarely can the answers be deduced using our bare hands and the naked eye, so the study of materials inevitably involves testing materials — measuring their properties and looking at their microstructure. Also during the manufacture and in-service period, testing of materials

becomes an indispensable step to control manufacturing processes, ensure product integrity and reliability, and make efficient use of products during their lift time.

In science and industry, materials can be tested both in destructive and non-destructive ways. Destructive tests are often used to determine the physical properties of materials such as tensile strength, fracture toughness and impact resistance, while non-destructive testing (NDT) [7] can in many cases evaluate materials and structures for discontinuities and differences in characteristics. As the name implies, NDT does not damage or permanently alter the product being inspected. Therefore, it is a highly valuable technique that can save both money and time in material research, production and maintenance.

NDT can be performed by a wide group of techniques based on penetrating medium or equipment used. Taking the aerospace industry as an example, ultrasonic inspection, radiography, and eddy current testing are largely utilized to evaluate the health condition of the aircraft structures [8]. Ultrasonic inspection [9] uses high frequency acoustic wave to detect subsurface flaws. Either the reflection or the attenuation of the sound energy can be measured to analyze the presence and location of discontinuities which could indicate defects such as voids, cracks, and delaminations. Alternatively, radiography [10] relies on the examination of variations in transmitted intensity of X-rays or gamma radiation arising from difference in the absorption coefficients of a defect and surrounding structure. Radiography is widely used to test the imperfections in welded parts of structures [11]. Lastly, eddy current [12] testing introduces an electrical current to detect defects within conductive materials since the flow of the eddy current is influenced by the presence of flaws. Eddy current technique is an effective method to detect the corrosion in multilayered structures [13]. Besides, optical NDT techniques such as shearography [14] and thermography [15] also show potential for subsurface defects measurement of aerospace structures. However, with the development of material science, NDT with a single method of damage determination cannot satisfy the modern tests. Material researchers expect the ability to access the depth features of materials, and to rebuild the internal structures virtually without damaging the specimen, to provide substantial information for material property evaluation.

Currently, ultrasonic testing, and x-ray computed tomography (x-ray CT) [16] are the dominant NDT techniques for structural imaging. Ultrasonic testing can estimate the internal structure of materials by detecting the echo when ultrasonic pulse waves are directed into specimens. Its high penetrating power allows a detection of tens of millimeters depth. But a major drawback is the low spatial resolution that is practically on the order of hundreds of micrometers [17]. In contrast, x-ray CT can provide 3D reconstructed images with

submicrometer resolution¹, but it has a complex design with a large instrument size and requires large amounts of computation, which is impossible for real time and in situ imaging. Therefore, new NDT techniques are still needed in the field of structural imaging.

1.2 Research Motivation

In the past two decades, an imaging technique named optical coherence tomography (OCT) [18] has become one of the hot topics in biomedical science. OCT is basically analogous to ultrasonic B-scan except that it uses light instead of sound. Fig. 1.1 shows one example of how OCT is performed [19]. A cross-sectional image is acquired by a succession of axial depth scans of optical backscattering or backreflection profiles at different transverse locations. The axial profiles provide the optical pathlength difference and intensity of backscattered or backreflected light. For the purpose of visualization, two-dimensional OCT data can be displayed as a gray scale or false color image. A volumetric OCT image can be performed in a same way with two orthogonal transverse scans. The working principle of OCT is based on low coherence interferometry which will be introduced in detail in chapter 2.

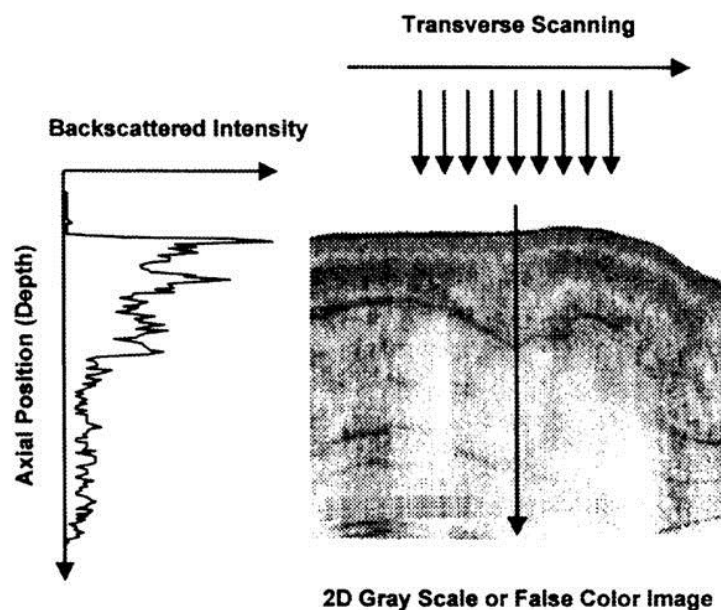


Fig. 1.1: Image generation in OCT. Cross-sectional images are constructed by measuring depth-resolved intensity of backreflected light at different transverse positions [19].

¹ Up to 0.2 μm spatial resolution can be achieved by x-ray CT scanners, e.g. Phoenix nanotom S designed by General Electric Company.

The greatest advantage of OCT is that it has a good compromise between the spatial resolution and penetration depth [19], as shown in Fig. 1.2. Typically, image resolutions of 1~15 μm can be achieved with OCT measurement, one or two orders of magnitude higher than the ones with conventional ultrasonic scan. Confocal microscopy [20], by using point illumination and a spatial pinhole to eliminate out-of-focus light in specimens, can have submicrometer resolution. But the image penetration of confocal microscopy is limited to a few hundred micrometers in general scattering media, which is much lower than with OCT that can penetrate 2~3 mm correspondingly. Besides, OCT has merits such as contactless measurement, relatively simply setup and computation, fast scan and display.

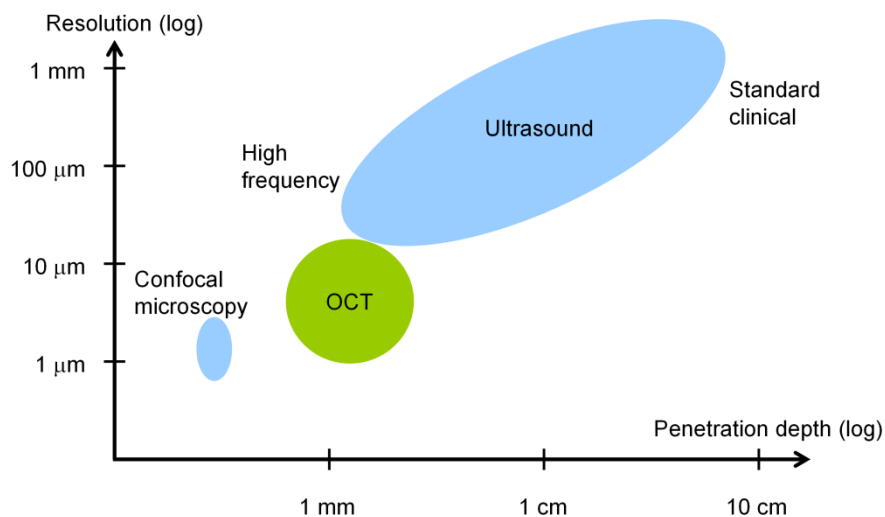


Fig. 1.2: Comparison of resolution and imaging depth for ultrasound, OCT, and confocal microscopy [19].

All the advantages make OCT an important tool for biomedical examination, and it has developed rapidly in the past 20 years, which can be deduced from the yearly publications in the PubMed database [21], summarized in Fig. 1.3. Besides, from the categorized publications, it can be seen that OCT is widely used in the biomedical field, e.g. ophthalmology, cardiovascular, gastroenterology and endoscopy, etc. Driven by these applications, OCT techniques are evolved rapidly as well. Recent developments of OCT techniques have led to enhanced sensitivity and imaging speed [22], to improved resolution [23], and to different imaging concepts [24-26]. Also there is a growing number of commercial companies [27] offering OCT scanners, showing a promising market for OCT technology.

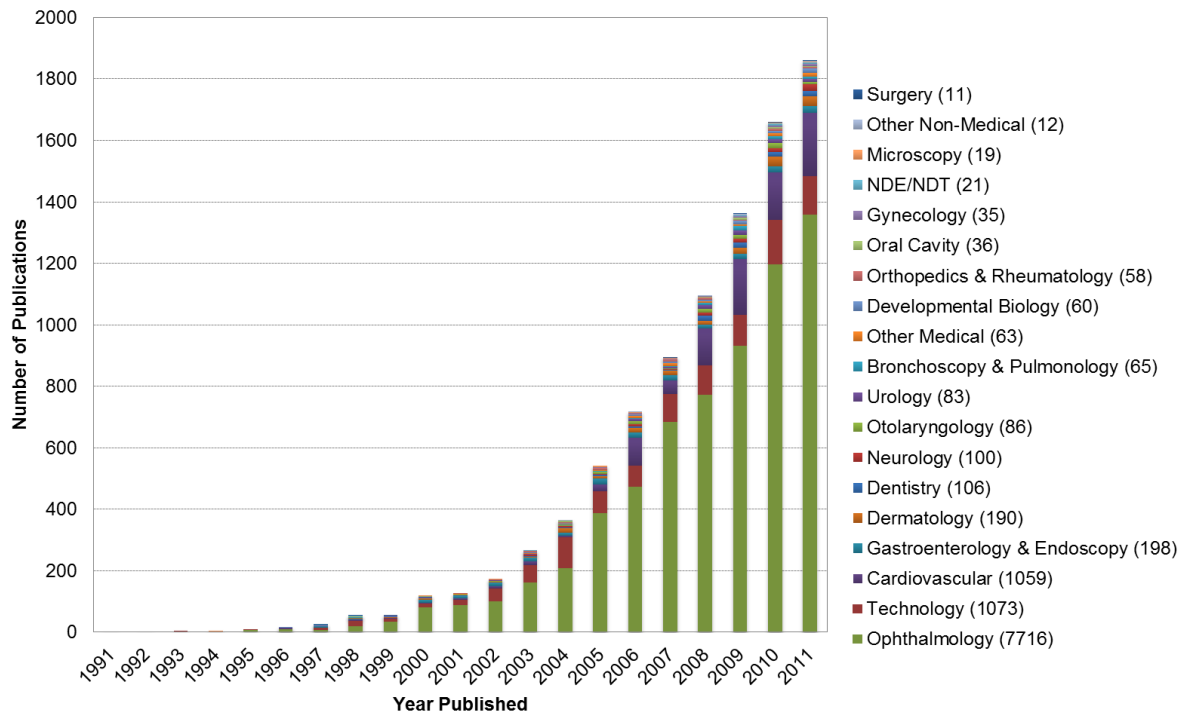


Fig. 1.3: Yearly OCT publications in PubMed categorized by application [21].

However, OCT in the NDT field, compared with the biomedical counterparts, is much lagging behind. Only a few research groups apply the technology to material testing, and therefore the progress in this field is slow. Two reviews of alternative OCT applications and technique developments beyond biomedicine were published by Stifter in 2007 [28] and Nemeth in 2013 [29]. Recent examples include the measurement of layer thickness in multi-layered foils [30], pharmaceutical tablets [31], the characterization of paper [32], ceramics [33], printed electronics [34], applications with polymer-based materials [35] and for artwork conservation [36]. However, so far these results are very initial and they have not made full use of the recent progress in OCT technology. For example, some NDT applications were implemented with commercial OCT systems which are designed for biomedical use. Due to the property differences between engineering materials and biomedical tissues, such as light absorption and scattering, commercial OCT instruments designed for biomedical applications are not exactly suitable for material characterization. In some applications which used customized OCT systems, not enough attention was paid to signal and image processing, which should be an important step to guarantee the image quality. Besides, rarely has research linked OCT with mechanical testing of materials. For example, monitoring crack growth or

evaluating displacement distributions within glass fiber composites under mechanical loadings has never been reported.

Therefore, the aim of this study is to use OCT as a novel NDT tool for material characterization. This includes:

1. Development of a state-of-art OCT system specialized for material characterization.
2. Design of a series of signal processing algorithm for improved image quality.
3. To study subsurface structure and structural changes of materials using OCT combined with mechanical loading.
4. To explore new imaging concepts, such as elastography [37], giving access to material mechanical properties.

Since the work is carried out in Aerospace NDT laboratory, Delft University of Technology (TU Delft), the primary testing objects are highly related with aerospace and wind energy products, such as glass fiber composites and polymer coatings. Some alternative specimens, e.g. oil paintings and wood were also considered for the OCT measurements.

1.3 Thesis Outline

The objective of the thesis is to design a novel OCT system for the non-destructive testing of materials, especially for composite materials. The scope of the thesis work includes an overview of OCT fundamentals and developments, the design of a customized setup and signal processing algorithms, and a selection of applications.

Chapter 2 starts with an introduction of OCT theory. Two dominant OCT modalities, time-domain OCT (TD-OCT) and Fourier-domain OCT (FD-OCT) are compared from the view of principle and performance. Recent developments of OCT techniques are also reviewed in this chapter.

Chapter 3 describes the customized OCT setup developed at TU Delft. The most attractive feature of the setup is that it couples TD-OCT and FD-OCT in one system allowing applications to select the strength of one or other of the techniques. The selection of components used in the system, such as light source, fiber polarizer, collimator, balanced detector, optical delay line (ODL), and translation stage, are discussed and justified in detail.

Chapter 4 focuses on signal processing algorithms for TD-OCT and FD-OCT. In TD-OCT, three techniques are discussed for the demodulation of axial signals. Their

performance is compared by using both simulated and experimental OCT data. While in FD-OCT, a series of signal processing algorithms are applied for improved signal and image quality. The whole OCT system, including hardware and software, has now been described. So at the end of this chapter, a selection of experiments are made to verify the performance of the customized OCT system.

Chapter 5 presents the results of material characterization using the customized OCT system. The investigated object is a glass fiber composite for the manufacture of a wind turbine blade. The measurements focus on internal microstructure and defects such as delamination. Special attention is given to delamination growth in the glass fiber composite. A succession of OCT volumetric images were obtained from a delaminated specimen under incremental loadings. They were further processed to reconstructed 3D crack surfaces to reveal the propagation of the delamination. The results are discussed and related to the performance of the composite materials.

Chapter 6 expands OCT applications to elastography (OCE), which is a technique typically for the measurement of volumetric deformation and strain within biomedical tissues [38]. In this study, an OCE system for the first time was designed for deformation measurement of glass fiber composites under different mechanical loadings. The advantages and possible further improvements for the OCE application on glass fiber composites are discussed.

Chapter 7 shows some further non-destructive testing applications with OCT. The customized OCT system has been used to test polymer coatings, giving the information such as thickness and microcracks in the coating materials. A wooden panel painting was investigated to characterize the varnish layer, the pigments and some crack defects. The back face of the painting was also studied by 3D reconstruction of the surface profile.

Chapter 8 discusses the research of this thesis. Conclusions and recommendations for further study are also presented.

References

- [1] W. F. Smith, and J. Hashemi, [Foundations of materials science and engineering], McGraw-Hill Publishing (2006).
- [2] Intelligent airframe, <http://www.a350xwb.com/advanced/fuselage/>.
- [3] [Half-year report 2013], The World Wind Energy Association (2013).
- [4] [Wind in power: 2013 European statistics], The European Wind Energy Association (2014).
- [5] Wind energy facts, <http://www.nwea.nl/windenergie-de-feiten>.
- [6] P. Brøndsted, H. Lilholt, and A. Lystrup, “Composite materials for wind power turbine blades,” *Annual Review of Materials Research*, 35, 505-538 (2005).
- [7] C. Hellier, [Handbook of nondestructive evaluation], McGraw-Hill (2001).
- [8] W. Staszewski, C. Boller, and G. R. Tomlinson, [Health monitoring of aerospace structures: smart sensor technologies and signal processing], John Wiley & Sons (2004).
- [9] J. Krautkramer, and H. Krautkrâmer, [Ultrasonic testing of materials], Cambridge University Press (1990).
- [10] R. Halmshaw, [Industrial radiology: theory and practice], Springer (1995).
- [11] T. W. Liao, and Y. Li, “An automated radiographic NDT system for weld inspection: Part II—Flaw detection,” *NDT & E International*, 31(3), 183-192 (1998).
- [12] B. Auld, and J. Moulder, “Review of advances in quantitative eddy current nondestructive evaluation,” *Journal of Nondestructive Evaluation*, 18(1), 3-36 (1999).

-
- [13] R. Smith, and G. Hugo, "Transient eddy current NDE for ageing aircraft-capabilities and limitations," *Insight: Non-Destructive Testing and Condition Monitoring*, 43(1), 14-25 (2001).
- [14] D. Francis, R. P. Tatam, and R. M. Groves, "Shearography technology and applications: a review," *Measurement Science and Technology*, 21(10), 102001 (2010).
- [15] C. Meola, G. M. Carlomagno, A. Squillace *et al.*, "Non-destructive evaluation of aerospace materials with lock-in thermography," *Engineering Failure Analysis*, 13(3), 380-388 (2006).
- [16] P. J. Schilling, B. R. Karedla, A. K. Tatiparthi *et al.*, "X-ray computed microtomography of internal damage in fiber reinforced polymer matrix composites," *Composites Science and Technology*, 65(14), 2071-2078 (2005).
- [17] A. Ng, and J. Swanevelder, "Resolution in ultrasound imaging," *Continuing Education in Anaesthesia, Critical Care & Pain*, mkr030 (2011).
- [18] D. Huang, E. Swanson, C. Lin *et al.*, "Optical coherence tomography," *Science*, 254(5035), 1178-1181 (1991).
- [19] B. E. Bouma, and G. J. Tearney, [Handbook of optical coherence tomography], Marcel Dekker (2002).
- [20] J. Pawley, [Handbook of biological confocal microscopy], Springer (2010).
- [21] Historical statistics of academic publications in the field of optical coherence tomography,
<http://www.octnews.org/articles/4061333/some-historical-statistics-of-academic-publication/>.
- [22] B. Potsaid, B. Baumann, D. Huang *et al.*, "Ultrahigh speed 1050nm swept source/Fourier domain OCT retinal and anterior segment imaging at 100,000 to 400,000 axial scans per second," *Optics Express*, 18(19), 20029 (2010).

- [23] N. Nishizawa, "Ultrahigh resolution optical coherence tomography," Opto-Electronics and Communications Conference (OECC), 2012 17th, 584-585 (2012).
- [24] E. Dalimier, and D. Salomon, "Full-field optical coherence tomography: a new technology for 3D high-resolution skin imaging," *Dermatology*, 224(1), 84-92 (2012).
- [25] E. Götzinger, B. Baumann, M. Pircher *et al.*, "Polarization maintaining fiber based ultra-high resolution spectral domain polarization sensitive optical coherence tomography," *Optics Express*, 17(25), 22704-22717 (2009).
- [26] C. Sun, B. Standish, and V. X. Yang, "Optical coherence elastography: current status and future applications," *Journal of Biomedical Optics*, 16(4), 043001 (2011).
- [27] OCT market, <http://www.sweptlaser.com/OCT-market>.
- [28] D. Stifter, "Beyond biomedicine: a review of alternative applications and developments for optical coherence tomography," *Applied Physics B*, 88(3), 337-357 (2007).
- [29] A. Nemeth, G. Hanneschlager, E. Leiss *et al.*, [Optical coherence tomography – applications in non- destructive testing and evaluation], Intech (2013).
- [30] G. Hanneschläger, A. Nemeth, C. Hofer *et al.*, "Optical coherence tomography as a tool for non destructive quality control of multi-layered foils," *Proceedings of the 6th NDT in Progress*, (2011).
- [31] S. Zhong, Y.-C. Shen, L. Ho *et al.*, "Non-destructive quantification of pharmaceutical tablet coatings using terahertz pulsed imaging and optical coherence tomography," *Optics and Lasers in Engineering*, 49(3), 361-365 (2011).
- [32] E. Alarousu, [Low coherence interferometry and optical coherence tomography in paper measurements], University of Oulu (2006).
- [33] J. Veilleux, C. Moreau, D. Lévesque *et al.*, "Optical coherence tomography for the inspection of plasma-sprayed ceramic coatings," *Journal of Thermal Spray Technology*, 16(3), 435-443 (2007).

- [34] J. Czajkowski, T. Prykäri, E. Alarousu *et al.*, “Optical coherence tomography as a method of quality inspection for printed electronics products,” *Optical Review*, 17(3), 257-262 (2010).

- [35] D. Stifter, K. Wiesauer, M. Wurm *et al.*, “Investigation of polymer and polymer/fibre composite materials with optical coherence tomography,” *Measurement Science and Technology*, 19(7), 074011 (2008).

- [36] P. Targowski, B. Rouba, M. Góra *et al.*, “Optical coherence tomography in art diagnostics and restoration,” *Applied Physics A*, 92(1), 1-9 (2008).

- [37] J. Ophir, I. Cespedes, H. Ponnekanti *et al.*, “Elastography: a quantitative method for imaging the elasticity of biological tissues,” *Ultrasonic Imaging*, 13(2), 111-134 (1991).

- [38] J. M. Schmitt, “OCT elastography: imaging microscopic deformation and strain of tissue,” *Optics Express*, 3(6), 199-211 (1998).

2

Fundamentals and Developments of Optical Coherence Tomography

2.1 Introduction

Optical coherence tomography (OCT) is a contactless and non-destructive technique for high-resolution imaging of microstructure within scattering media. Originally developed for the imaging of the human retina in 1991 [1], nowadays OCT not only finds widespread biomedical applications, but its techniques have also evolved dramatically. The first OCT modality was realized in time domain (TD-OCT) based on a low coherence interferometer, similar to those used in industrial metrology for measuring the thickness of thin films [2] and refractive index [3]. In order to improve the imaging speed, Fourier domain OCT (FD-OCT) was developed afterwards as a new generational OCT system which has the advantage that no moving parts are needed to obtain axial scans [4]. The spectral intensity detected by a spectrometer at one shot is then Fourier transformed into time domain to reconstruct the depth-resolved optical structure of a sample. Lately, new functional OCT configurations, such as polarization sensitive OCT (PS-OCT) [5] and Doppler OCT (DOCT) [6] were developed to give access to additional structural information like birefringence and fluid flow. Besides, the development of OCT components, e.g. light source and optical scanners also promote OCT into a high resolution and high speed structural imaging technique [7, 8].

In this chapter, OCT principles are introduced first. The fundamentals of two main categories of OCT instrumentation, TD-OCT and FD-OCT are described in detail. These

two OCT modalities are also compared by the performance such as imaging speed, spectral requirement and signal to noise ratio (SNR). Then the recent technique developments of OCT are reviewed. The evolution of OCT light source, scanners and new imaging concept are introduced. Further OCT developments for NDT application are recommended at the end of this chapter.

2.2 Fundamentals of Optical Coherence Tomography

2.2.1 Time-domain Optical Coherence Tomography

In OCT, the first step in constructing a tomographic image is the measurement of light backreflected from within the material or tissue. A typical TD-OCT is based on the Low-coherence interferometer, as shown in Fig. 2.1(a). Light emitted from the optical source is divided by a beamsplitter into reference and sample beams. The beam reflected from the reference mirror is recombined at the beamsplitter with the one reflected from the sample, and finally the interference signal is collected by a photo detector. A single axial profile of optical reflectivity versus depth into the sample is obtained by rapidly translating the reference mirror and synchronously recording the magnitude of the resulting interference signal, as shown in Fig. 2.1(b). The envelope of the interference signal represents one axial profile of optical reflectivity in a sample.

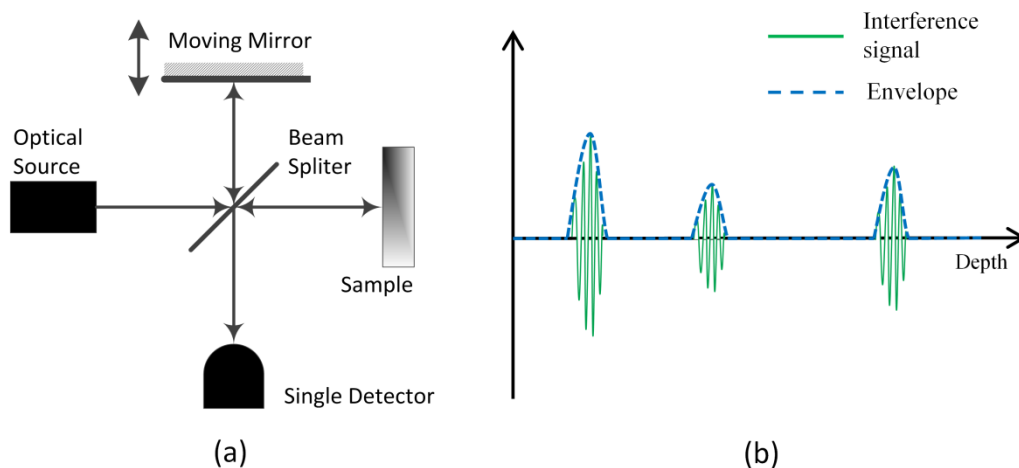


Fig. 2.1: (a) Schematic diagram of typical TD-OCT system and (b) one A-scan signal. The envelope of the modulated signal represents axial profile of sample optical reflectivity that comprises one vertical line in the tomogram.

The optical source for OCT should be a low-coherent light that consists of a finite bandwidth of frequency. An ideal one is a near infrared light source with Gaussian distribution (Section 2.3.2 and 2.4.1), as shown in Fig. 2.2. Under this condition, the reference and sample electric fields, E_r and E_s in an interferometer can be expressed as functions of frequency ω and time t [9]:

$$E_r(\omega, t) = A_r(\omega) \exp[-j(2\beta_r(\omega)l_r - \omega t)] \quad (2.1)$$

and

$$E_s(\omega, t) = A_s(\omega) \exp[-j(2\beta_s(\omega)l_s - \omega t)] \quad (2.2)$$

where $A_r(\omega)$ and $A_s(\omega)$ are the electric field amplitudes. l_r and l_s are the pathlengths of reference and sample arms respectively. t is a time during the sweeping of the reference mirror. $\beta_r(\omega)$ and $\beta_s(\omega)$ are the propagation constants which are frequency dependent.

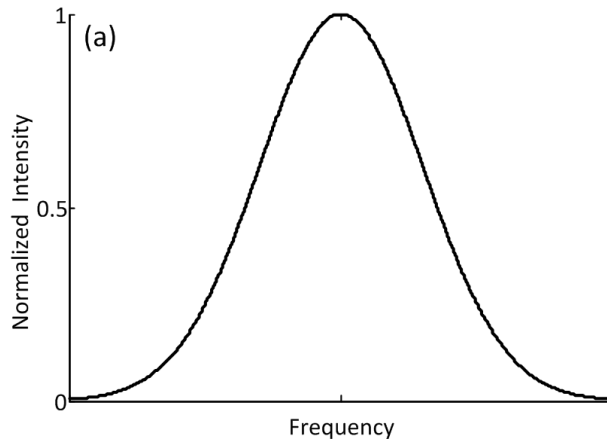


Fig. 2.2: A Gaussian optical source for OCT configuration.

Assuming that the sample and reference arms consist of uniform, linear, non-dispersive material, the propagation constants in each arm are the same and can be rewrite as a first-order Taylor expansion [10]:

$$\beta_r(\omega) = \beta_s(\omega) = \beta(\omega_0) + \beta'(\omega_0)(\omega - \omega_0) \quad (2.3)$$

where $\beta(\omega_0)$ is the propagation constant at the center frequency ω_0 . Then the phase mismatch $\Delta\phi(\omega) = 2\beta_s(\omega)l_s - 2\beta_r(\omega)l_r$ is determined solely by the pathlength mismatch $\Delta l = l_s - l_r$ through:

$$\Delta\phi(\omega) = \beta(\omega_0)(2\Delta l) + \beta'(\omega_0)(\omega - \omega_0)(2\Delta l) \quad (2.4)$$

For a 50/50 beamsplitter in an OCT configuration, the intensity collected by the photo detector I can be expressed as [11]:

$$\begin{aligned} I &= \left| \frac{1}{\sqrt{2}} E_r + \frac{1}{\sqrt{2}} E_s \right|^2 \\ &= \frac{1}{2} |E_r|^2 + \frac{1}{2} |E_s|^2 + \text{Re}\{E_r^* E_s\} \\ &= \frac{1}{2} (I_r + I_s) + \text{Re}\{E_r^* E_s\} \end{aligned} \quad (2.5)$$

where I_r and I_s , are the mean intensities returning from the reference and sample arms of the interferometer respectively, and comprise the DC components in the interference signal. The second term of the equation, $\text{Re}\{E_r^* E_s\}$, represents the amplitude of the interference fringes that carry information about sample structure. As the interference signal is proportional to the sum of the interference from each monochromatic wave component, Eq. 2.5 can be further expressed as [10]:

$$I \propto \text{Re} \left\{ \int_{-\infty}^{\infty} E_r^*(\omega, t) E_s(\omega, t) \frac{d\omega}{2\pi} \right\} = \text{Re} \left\{ \int_{-\infty}^{\infty} S(\omega) \exp[-j\Delta\phi(\omega)] \frac{d\omega}{2\pi} \right\} \quad (2.6)$$

where the definition $S(\omega) = A_r^*(\omega) A_s(\omega)$ has been used. Taking account of the propagation constant and the phase mismatch given in Eq. 2.3 and 2.4, the detected intensity can be further written as:

$$I \propto \text{Re} \left\{ \exp[-j\omega_0 \Delta\tau_p] \int_{-\infty}^{\infty} S(\omega - \omega_0) \exp[-j(\omega - \omega_0) \Delta\tau_g] \frac{d(\omega - \omega_0)}{2\pi} \right\} \quad (2.7)$$

where the phase delay mismatch $\Delta\tau_p$ and the group delay mismatch $\Delta\tau_g$ are defined as:

$$\Delta\tau_p = \frac{\beta(\omega_0)}{\omega_0} (2\Delta l) = \frac{2\Delta l}{v_p} \quad (2.8)$$

and

$$\Delta\tau_g = \frac{\beta'(\omega_0)}{\omega_0} (2\Delta l) = \frac{2\Delta l}{v_g} \quad (2.9)$$

Thus, $v_p = \omega_0 / \beta(\omega_0)$ and $v_g = 1 / \beta'(\omega_0)$ are the phase and group velocity respectively.

Assume that the light source has a Gaussian power spectral density, $S(\omega - \omega_0)$, given by [12]:

$$S(\omega - \omega_0) = \frac{1}{\sigma_\omega \sqrt{2\pi}} \exp\left[-\frac{(\omega - \omega_0)^2}{2\sigma_\omega^2}\right] \quad (2.10)$$

where ω_0 is defined as the center frequency and σ_ω is the standard deviation of the light source frequency. Eq. 2.7 can be described as:

$$I \propto \text{Re} \left\{ \exp\left[-\frac{\sigma_\omega^2 \Delta\tau_g^2}{2}\right] \exp[-j\omega_0 \Delta\tau_p] \right\} \quad (2.11)$$

Eq. 2.11 indicates that the amplitude of the interference fringe contains a Gaussian envelope and a carrier, as shown in Fig. 2.1(b). The envelope falls off rapidly with increasing group delay mismatch $\Delta\tau_g$ and is modulated by a carrier that oscillates with increasing phase delay mismatch $\Delta\tau_p$. Thus, Eq. 2.11 defines the axial resolving properties of OCT system. The interference fringes can only be observed when the optical pathlengths of reference and sample arm are matched, and it reaches a maximum when the two pathlengths are identically equal. Therefore, by continuously translating the reference mirror to change the optical pathlength, a serial of short oscillatory pulses are detected, centered at times when the position of the reference mirror corresponds to the locations of backreflecting interfaces along one depth of a specimen. In this way, a single axial profile of sample optical reflectivity can be achieved, indicated by the envelope of the axial scan signal, as shown in Fig. 2.1(b). This axial profile is referred to as an A-scan that comprises one vertical line in the tomogram. By laterally scanning the penetration beam in either one or two orthogonal directions, a cross-sectional (B-scan) or volumetric image can be obtained finally. The axial and lateral resolutions of the image are determined by the coherence length of the light source and the spot size of the incident beam to the sample respectively, which are discussed in section 2.2.3 in detail.

2.2.2 Fourier-domain Optical Coherence Tomography

Recently the FD-OCT technique has experienced increased attention and has developed rapidly. The measurement principle is based on spectral interferometry, as depicted in Fig. 2.3. In FD-OCT, the reference mirror is kept still and the single light intensity detector used in TD-OCT is replaced by a spectrometer that separates the different wavenumbers k

($k = 2\pi / \lambda$). With an inverse Fourier transform of the detected spectral intensity, one depth profile can be obtained.

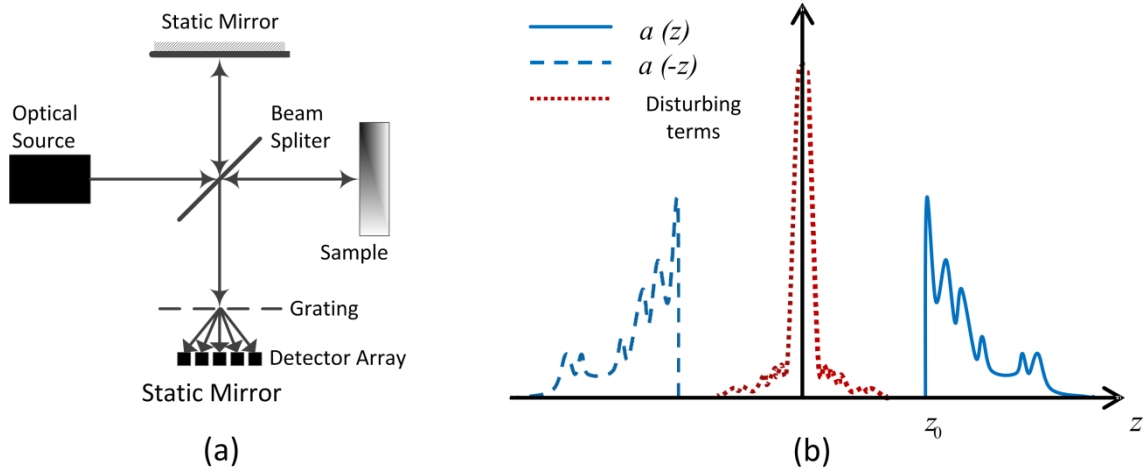


Fig. 2.3: (a) Schematic diagram of typical FD-OCT system and (b) one A-scan signal after inverse Fourier transform. The object signal starts from the offset z_0 .

Theoretically, the spectral intensity $I(k)$ acquired from a spectrometer can be expressed as [12]:

$$I(k) = G(k) \left| a_r \exp(i2kl_r) + \int_{z_0}^{\infty} a(z) \exp\{i2k(l_r + nz)\} dz \right|^2 \quad (2.12)$$

where $G(k)$ is the spectral intensity distribution of the light source. The first and second term within square brackets is the signal from the reference and the sample arm respectively. a_r is the reflection amplitude from the reference mirror which is a constant and is arbitrarily set at 1 for simplicity. $a(z)$ is the backscattering amplitude of the object signal that needs to be recovered. z_0 is the distance mismatch between reference plane and object surface. l_r and $(l_r + nz)$ are the optical pathlength in reference and sample arm. n is the average refractive index of the object. Since we are only interested in the pathlength difference, l_r can be defined as 0. With these assumptions the interference signal $I(k)$ can be written as:

$$\begin{aligned} I(k) &= G(k) \left| 1 + \int_{z_0}^{\infty} a(z) \exp(i2knz) dz \right|^2 \\ &= G(k) \left[1 + 2 \int_{z_0}^{\infty} a(z) \cos(2knz) dz + \int_{z_0}^{\infty} \int_{z_0}^{\infty} a(z) a(z') \exp\{-i2kn(z - z')\} dz dz' \right] \end{aligned} \quad (2.13a)$$

Since $a(z) = 0$ for all $z < z_0$, $a(z)$ can be replaced by the symmetrical expansion $\hat{a}(z) = a(z) + a(-z)$. Now Eq. 2.13a becomes:

$$I(k) = G(k) \left[1 + \int_{-\infty}^{+\infty} \hat{a}(z) \cos(2knz) dz + \frac{1}{4} \int_{-\infty}^{+\infty} \int_{-\infty}^{+\infty} \hat{a}(z) \hat{a}(z') \exp\{-i2kn(z-z')\} dz dz' \right] \quad (2.13b)$$

It can be seen that the third (autocorrelation) term describes the mutual interference of all elementary waves. By defining $R(\hat{a}(z)) = \int_{-\infty}^{+\infty} \hat{a}(z) \hat{a}(z') dz'$, Eq. 2.13b can be further written as:

$$I(k) = G(k) \left[1 + \int_{-\infty}^{+\infty} \hat{a}(z) \exp(-i2knz) dz + \frac{1}{4} \int_{-\infty}^{+\infty} R[\hat{a}(z)] \exp(-i2knz) dz \right] \quad (2.13c)$$

The second and third terms in Eq. 2.13c can be treated as the expressions of Fourier transform of $\hat{a}(z)$ and $R(\hat{a}(z))$ respectively. Therefore the spectral signal is finally deduced as:

$$I(k) = G(k) \left[1 + \frac{1}{2} F\{\hat{a}(z)\} + \frac{1}{8} F\{R[\hat{a}(z)]\} \right] \quad (2.14)$$

where F denotes the Fourier transform. Making use of the convolution property of Fourier transform $x(z) \otimes y(z) \xrightarrow{F} X(k)Y(k)$, the inverse Fourier transform (F^{-1}) of Eq. 2.14 can be calculated as:

$$\begin{aligned} F^{-1}\{I(k)\} &= F^{-1}\{G(k)\} \otimes \left[\delta(z) + \frac{1}{2} \hat{a}(z) + \frac{1}{8} R\{\hat{a}(z)\} \right] \\ &= A \otimes (B + C + D) \end{aligned} \quad (2.15)$$

where \otimes indicates convolution and $\delta(z)$ is the delta function. From this result the symmetric scattering amplitude $\hat{a}(z)$ and therefore $a(z)$ can be deduced. However, besides the signal term C , there are three disturbing terms, A , B and D . Since $A \otimes B$ and $A \otimes D$ are located around $z=0$, a small offset in z_0 (usually 200 μm is sufficient) can separate them from the signal term. Taking the spectral characteristic of the light source into account, the object signal can finally be deconvoluted from $A \otimes C$. Fig. 2.3(b) shows an example of the interferogram recorded with FD-OCT after inverse Fourier transform.

2.2.3 Resolution of Optical Coherence Tomography

In spite of the different image principles, the spatial resolution provided by TD-OCT and FD-OCT can be determined in the same way. In contrast to a conventional microscope, OCT has the advantage of independent axial and lateral resolution. The axial resolution of OCT is the Full-Width-Half-Maximum (FWHM) of the coherence length, as shown in Fig. 2.4(b).

Thus the axial resolution, Δz , is determined by light source parameters and the specimen refractive index, given by:

$$\Delta z = \frac{2 \ln 2}{n\pi} \left(\frac{\lambda_0^2}{\Delta\lambda} \right) \quad (2.16)$$

where λ_0 and $\Delta\lambda$ refer to the center wavelength and FWHM bandwidth of the optical source respectively, as shown in Fig. 2.4(a). n is the average refractive index of the object. The axial resolution is inversely proportional to the bandwidth of the light source, and thus broad bandwidth optical sources are required for high axial resolution. Following this definition, a typical superluminescent diode (SLD) centered at 800 nm with 60 nm FWHM, has a theoretical axial resolution of approximately 5 μm in the air.

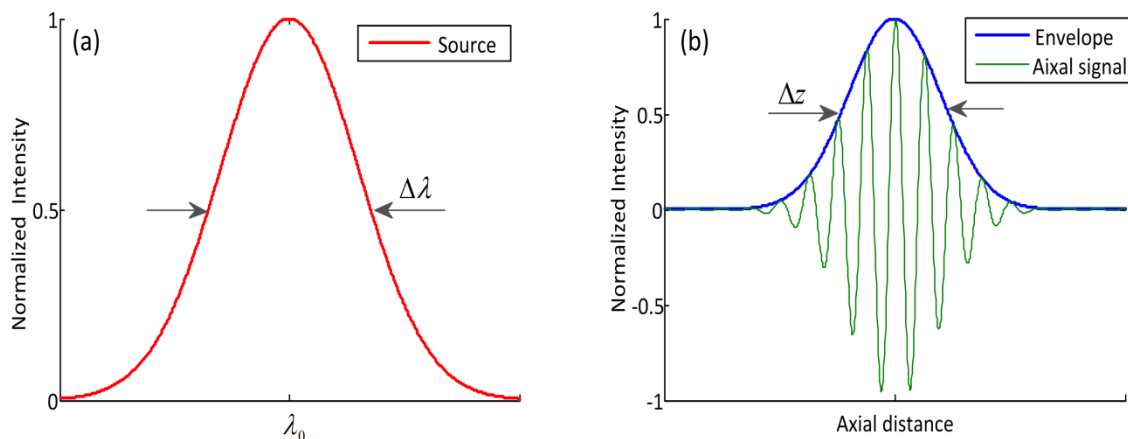


Fig. 2.4: (a) OCT light source and (b) corresponding interference signal. The axial resolution Δz is decided by the center wavelength λ_0 and bandwidth $\Delta\lambda$ of the light source.

The lateral resolution for OCT imaging, Δx , is the same as for conventional microscopy and is determined by the focusing properties of an optical beam, given by:

$$\Delta x = 0.61 \frac{\lambda_0}{NA} \quad (2.17)$$

where NA is the effective numerical aperture, which can be approximated as:

$$NA \approx \frac{d}{2f} \quad (2.18)$$

Here d is the spot size on the objective lens and f is its focal length. High lateral resolution (e.g. $1\ \mu\text{m}$) can be achieved by using a large numerical aperture and focusing the beam to a small spot size. However there is always a tradeoff between the lateral resolution Δx and the depth of focus b , given by:

$$b = \frac{2\lambda_0 n}{NA^2} \quad (2.19)$$

Fig. 2.5 shows schematically the relationship between the focused beam size and depth of focusing field with low and high numerical aperture focusing.

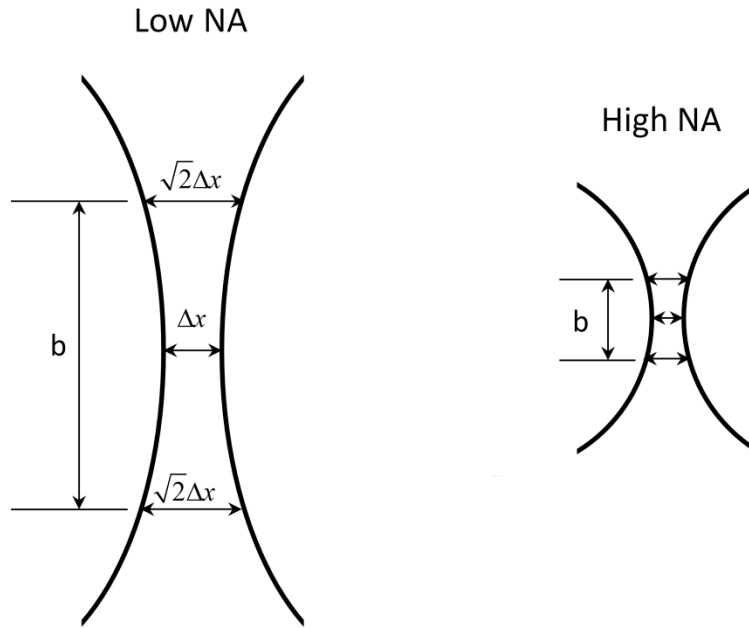


Fig. 2.5: The tradeoff between focused spot size and depth of focus for low and high numerical aperture focusing.

2.3 Performance Comparison of TD-OCT and FD-OCT

As introduced above, TD-OCT translates the reference mirror in a low-coherence interferometer to obtain the optical reflectivity versus depth, allowing the generation of structural maps within a specimen. Differently FD-OCT measures the spectrum of an interferometer output and recovers one depth profile by a Fourier transform. The spectrum intensity is usually obtained by a spectrometer which contains a detector array. It can also be realized by using a single detector and a tuneable light source in the interferometer, which refers to swept source OCT (SS-OCT) that will be introduced in section 2.4.3. The

following discussions mainly compare the performance of TD-OCT and FD-OCT using a spectrometer.

2.3.1 General Performance

A major advantage of a TD-OCT system is its simple design and hence the low cost of the instrument. It is also capable of unlimited axial scan which depends only on the translation range of the reference mirror. However, on the other hand, the movement of the reference mirror slows down the data acquisition process. To achieve real-time imaging, a complex design such as grating based optical delay line [13] (see section 2.4.2) or an area detector for full-field measurement (see section 2.4.4) is needed.

On the contrary, a main feature of FD-OCT is the lack of movable parts in the reference arm of the interferometer. The total distribution of scattering amplitude along one depth of the object is measured at once, which is much faster than TD-OCT and allows real-time monitoring of structure variations [4, 14].

However, in FD-OCT the depth measurement range, z_{max} , is highly reliant on the number of pixels in the detector array [15], given by:

$$z_{max} = \frac{\lambda_0^2}{4n\lambda_{full}} N \quad (2.20)$$

where λ_{full} and N are the full spectral bandwidth and total pixel number of the linear CCD detector respectively. If a detector array consists of 512 elements and the optical source is centered at 1550 nm with 160 nm full spectral bandwidth, then the maximum axial scan depth for a sample with 1.55 refractive index is only 1.24 mm. Eq. 2.20 indicates that the measurement range can be improved with an increased number of pixels in the detector array, but this brings an additional cost as well, a factor which is important to consider during an instrument design.

Besides, as discussed in section 2.2.3, a typical OCT system cannot provide a high lateral resolution with a long depth of focus that covers the whole axial scan range. To solve this problem, TD-OCT can track the focal depth by translating the focal lens along with the axial scan (movement of the reference mirror) [16]. However in FD-OCT this method is not possible since all the depth signal is acquired simultaneously. A possible solution could be to use advanced signal processing that acquire multiple images with different zones of focus and to fuse these images to create a single one with an extended focus depth [17].

2.3.2 Spectral Requirement

Another interesting difference is that of the spectral quality of the source. In TD-OCT, Eq. 2.11 represents the autocorrelation function for a Gaussian source. According to Wiener-Khinchine theory [18], the autocorrelation function is the inverse Fourier transform of the source power spectrum. Therefore, a source with a Gaussian spectrum ideally yields a Gaussian autocorrelation function, as shown in Fig. 2.4. This is critical for performing high-resolution imaging. If the light source has a noisy Gaussian or a non-Gaussian spectrum, the modulation or ripples in the light source can cause side peaks or echoes around the main reflection peaks in an axial signal. Two examples, a noisy Gaussian spectrum (SNR=30 dB) and a Gaussian spectrum with side lobes are shown in Fig. 2.6(a) and (d). The corresponding envelope of the axial signals, shown in Fig. 2.6(b) and (e), can be estimated by inverse Fourier transform. Fig. 2.6(c) and (f) are the envelopes displayed in logarithm scale, from which the deterioration of the signal can be clearly observed. The significant tails around the main reflection peak may prevent the detection of a weaker reflector nearby. However FD-OCT can compensate for non-Gaussian spectrum by dividing the interference spectrum by the light source spectrum (see Eq. 2.14). The light source spectrum $G(k)$ can be easily measured by the spectrometer in a FD-OCT system.

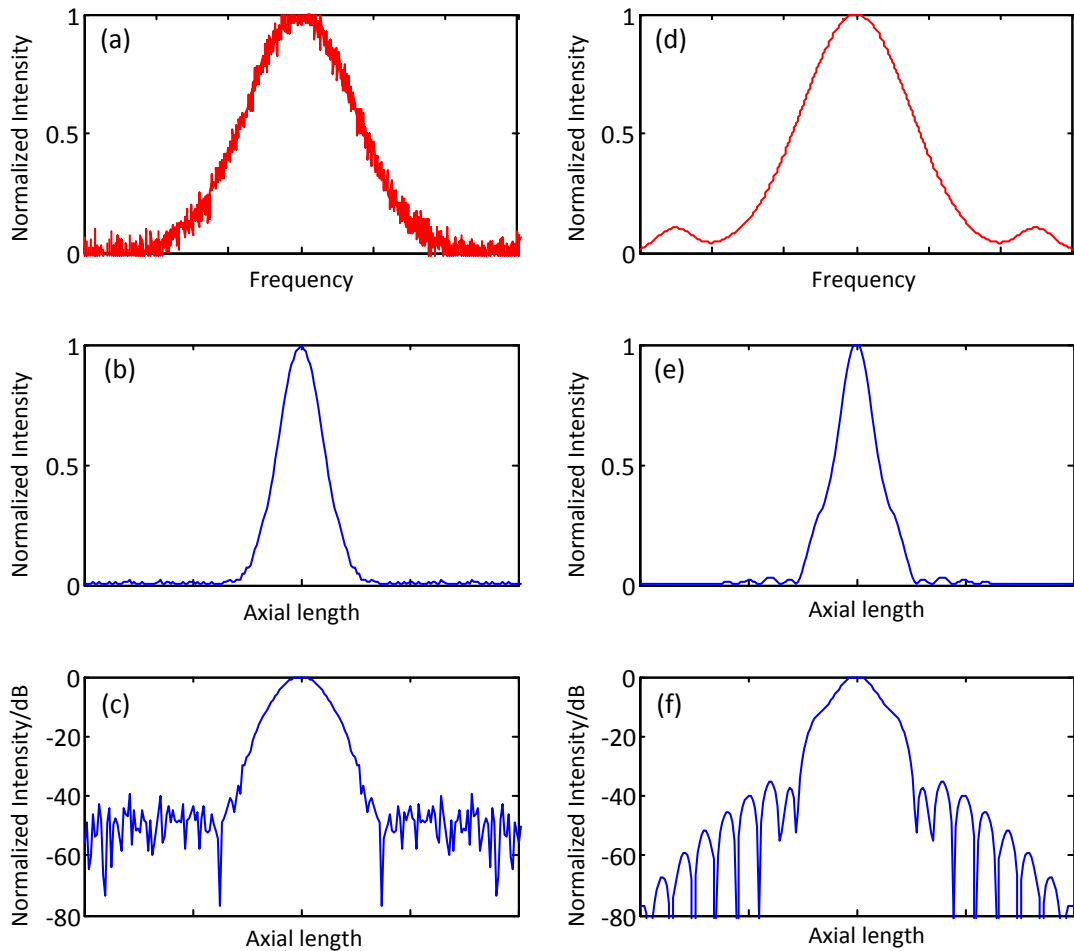


Fig. 2.6: Light sources with a noisy Gaussian spectrum (a) and a non-Gaussian spectrum (d), and the corresponding interference signals (b) and (e) from an OCT system. (c) and (f) are the interference signals in logarithmic scale.

2.3.3 Signal to Noise Ratio

In OCT the dominant sources of noise are shot noise, thermal noise, and relative intensity noise (RIN) [19]. Shot noise arises from current fluctuations due to the quantization of light and charge. The noise power is proportional to the electronic charge and the photocurrent. Thermal noise is generated by resistors in the receiver electronics. The noise current is approximately zero-mean white noise. The RIN, also mentioned as excess photon noise, refers to the fluctuations in output intensity of a light source due to the beating of various spectral components having random phase. For unpolarized broadband sources such as SLDs, the noise is only dependent on the spectral bandwidth of light source [20].

Signal to noise ratio (SNR), is a critical parameter to evaluate to the performance of an OCT imaging system. Several literature sources [12, 21-23] have deduced the theoretical SNR of TD and FD-OCT and a common expression is given by:

$$SNR_{TD} = 2 \frac{\eta \tau}{E_v} P_s \quad (2.21)$$

and

$$SNR_{FD} = M \frac{\eta \tau}{E_v} P_s = \frac{M}{2} SNR_{TD} \quad (2.22)$$

where η and E_v are the quantum efficiency and the photon energy respectively. τ is the acquisition time for a single photodetector measurement. P_s is the light power backreflected from a sample and M is the number of detectors in a spectrometer. From Eq. 2.22, it can be seen that FD-OCT has an enormous advantage in SNR by a factor $M/2$ improvement over TD-OCT. However, the theoretical SNR is calculated based on shot noise-limited detection whereby the thermal noise and the RIN become negligible. Achievement of this shot-noise-limited detection requires sufficient reference arm power to assure shot noise dominance which could have two limitations [24]. The first one is that the optical power from the reference arm can only be increased to the detector saturation level, and the second one is that the increase of the optical power may cause the RIN noise to dominate. An elaborated design on the interferometer and control of the reference arm power is crucial to achieve the optimal SNR of an OCT system.

Besides, it is also worth mentioning the mechanism to compensate for the noise. In TD-OCT, a dual balanced detector can be used to remove the RIN noise. Due to the movement of reference mirror, the Doppler shift is introduced, given by:

$$f_d = \frac{2v_m}{\lambda_0} \quad (2.23)$$

where f_d is the Doppler frequency and v_m is the velocity of reference mirror. The Doppler shift modulates the interference signal to a high frequency, which also offers certain advantages in noise reduction by bandpass filtering (see chapter 4). However, in FD-OCT [25], due to a different imaging principle, balanced detection and bandpass filter are not operable. On the contrary, the finite detector elements in FD-OCT will act as lowpass filters during Fourier transform, which allows in thermal noise, the RIN and the dc signal. A full evaluation of the SNR in TD and FD-OCT is presented in chapter 4.

A full performance comparison between these two OCT modalities is summarized in Table 2.1.

Table 2.1: Performance comparison between TD-OCT and FD-OCT

	TD-OCT	FD-OCT
Spatial resolution	High axial and lateral resolution decided by light source and spot size respectively; depth of focus can be modified.	Same as TD-OCT, but extended depth focusing needs advanced signal processing algorithms.
Imaging speed	Slow. A complex design is needed to reach 4000 A-scans/s [13].	Max. 500,000 A-scans/s [14] since no movement is needed for the reference mirror.
Depth scan range	Only decided by the moving range of the reference mirror.	Limited by the number of detector elements (normally less than 2 mm).
Spectral requirement	Non-Gaussian light source brings harmonic artifacts into the signal.	Influence of the spectrum can be eliminated by division.
SNR	Extensive noise elimination by: <ol style="list-style-type: none"> 1. Balanced detection 2. Bandpass filtering 	Higher than TD-OCT, but an elaborated system design is required to reach shot-noise-limited detection.

2.4 Developments of Optical Coherence Tomography

2.4.1 Light Source

In OCT, the light source has a large influence on the system performance. Generally, the requirements of light source for OCT imaging are: 1) short coherence length, and 2) emission in the near infrared. The first requirement, short coherence length determines the axial resolution of an OCT system. From Eq. 2.16 it can be seen that the broader the bandwidth, the better axial resolution that can be achieved. The second requirement, emission in the near infrared, is related to the penetration depth. OCT needs to operate in a spectral range in which

scattering and absorption occur less so that the penetration of light into the object is adequate. In studies carried out to date, the deepest penetration in both biomedical tissues and engineering materials has been achieved using sources with wavelengths between 1200 and 1800 nm [26-28]. As an example, in a report by M. Wurm et al [29], two OCT systems with center wavelengths of 840 and 1550 nm were used to characterize polymer foams with different pore sizes. As shown in Fig. 2.7, it can be seen 1550 nm OCT could provide a better penetration depth, compared with 840 nm OCT. However, it is also noted from Eq. 2.16 that the longer center wavelength can greatly decrease the axial resolution. A compromise between the axial resolution and penetration depth is needed especially when the bandwidth of the light source is not so broad.

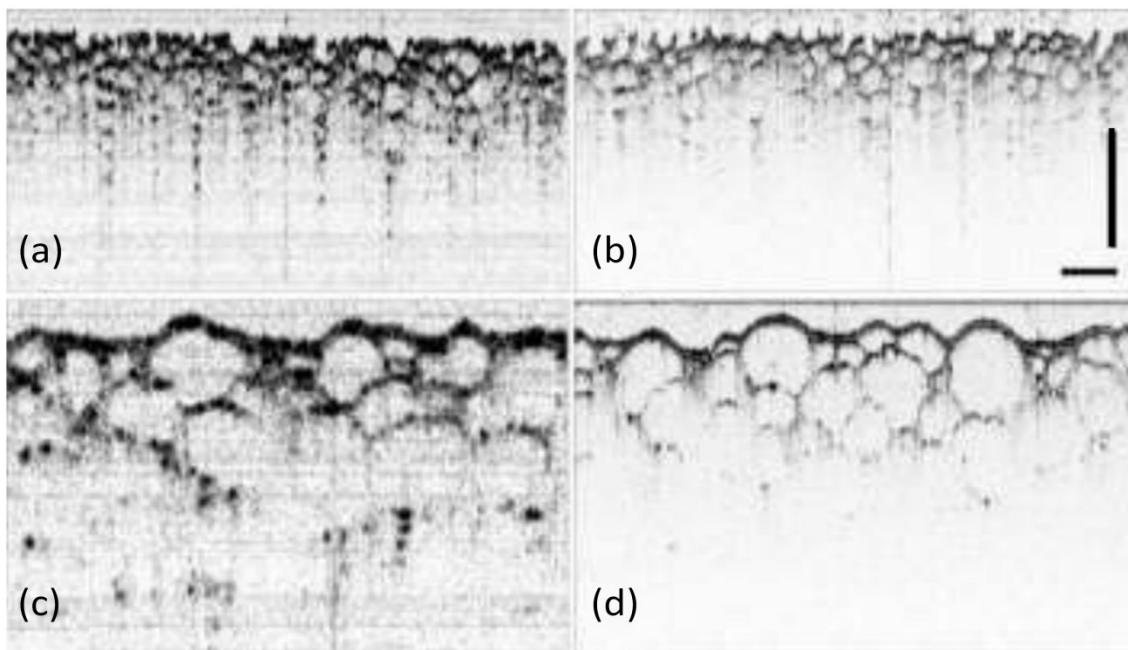


Fig. 2.7: OCT cross-sectional images taken from polymer foam samples with different pore sizes. images (a) and (c) are obtained using a light source with a center wavelength of 1550 nm, while images (b) and (d) are taken at 840 nm [29]. Scale bars vertical and horizontal in (b): 500 μm .

By far, the most commonly used broadband source for OCT is a superluminescent diode (SLD) because of its simplicity, high irradiance (1-20 mW), and relatively low cost [11, 19]. Usually these SLDs have broad spectra in the range 10-70 nm FWHM and with center wavelengths ranging from 675 to 1550 nm. This results in coherence lengths of typically 10-30 μm , which are not short enough for high axial resolution. It also explains why SLDs with longer center wavelengths have not been considered in an OCT system due to the greatly

deteriorated axial resolution¹. Recently some studies gave the solution of coupling multiple individual SLDs [30, 31]. For example, two SLDs with center wavelengths of 840 and 920 nm yield to a spectral FWHM of 155 nm and 3 μm axial resolution in the air.

At the cutting edge of broadband light generation, femtosecond lasers [32-34] which are titanium sapphire ($\text{Ti}:\text{Al}_2\text{O}_3$) and chromium forsterite ($\text{Cr}^{4+}\text{Mg}_2\text{SiO}_4$) lasers, are used in OCT, particularly when high resolution or source power is required. The $\text{Ti}:\text{Al}_2\text{O}_3$ laser usually has a center wavelength around 800 nm, and a peak power of approximately 400 mW. The bandwidth of the source can reach 300 nm, resulting in an axial resolution of less than 1 μm . Comparably, the $\text{Cr}^{4+}\text{Mg}_2\text{SiO}_4$ laser offers superior penetration in a turbid object with a longer center wavelength around 1300 nm. The source power can reach 300 mW and the bandwidth is 200 nm, allowing an axial resolution of below 4 μm . However, it is noted that femtosecond lasers are generally complex, unstable, and expensive. Since many studies are moving toward in-situ and even real-time imaging, a simple, compact, and robust system is essential for OCT. Further advancements for OCT sources could be reductions in complexity, size, and cost.

Besides, other sources, such as swept laser and thermal light are used for new imaging concepts, such as swept source OCT (SS-OCT) and full field OCT (FF-OCT), which are introduced in section 2.4.3 and section 2.4.4.

2.4.2 OCT Scanners

OCT imaging contains axial and lateral scans. Axial scanning, as introduced before, is performed differently in TD-OCT and FD-OCT setups. TD-OCT relies on an optical delay line (ODL) changing the reference pathlength, to determine the depth information of an object. The simplest version of an ODL is a mirror mounted on a linear translation stage, as shown in Fig. 2.8(a). The reference light is directed towards the mirror, and then reflected back to the interferometer system. A mechanical translation stage usually has more than enough working range to provide a sufficient axial scan. However, a major drawback is the low scan velocity. Although a commercial linear stage can move at a speed of 1m/s (LSQ Series, Zaber), the low repetition limits the overall imaging speed. Besides, translation stages with actuators such as dc motors, stepper motors, have some degree of nonlinearity in their motion, which could introduce image distortion.

¹ E.g., an SLD (FNPL-2000-2400-XXS, Frankfurt Laser Company, Germany) centered at 2350 nm with 35 nm FWHM results to an OCT axial resolution only 70 μm .

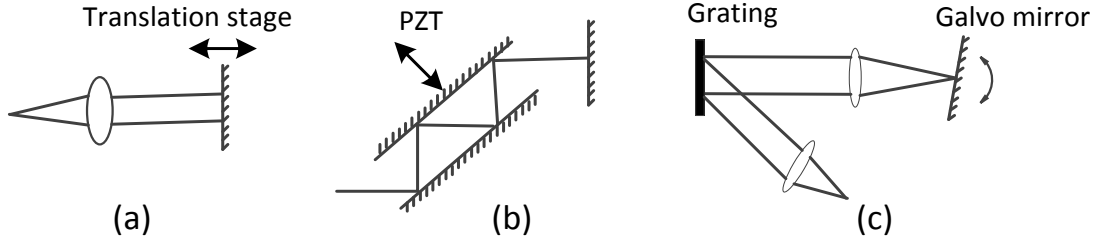


Fig. 2.8: Examples of ODL for scanning the reference pathlength in TD-OCT systems. (a) Linear translating mirror. (b) Parallel reflecting mirrors driven by a piezoelectric actuator. (c) Grating based ODL.

The development of faster scan methods has been studied in numerous papers. For example, by using a piezoelectric transducer to drive a parallel mirror system (Fig. 2.8 (b)), the scan range and velocity are amplified due to multiple reflections of the reference light. The maximum repetition rate is then greater than 100 scans/s and a 2-3 mm scanning range can be achieved [35]. Another advanced technique, the grating based optical delay line, was originally developed for femtosecond pulse measurement and has now been applied to OCT. As shown in Fig. 2.8(c), this system employs a grating and oscillating mirror to create an optical delay line that can achieve 4000 scans/s [13]. A major disadvantage of this ODL, besides complexity, is the power loss associated with the grating and the chromatic dispersion of the broadband source. Other rapid ODL scanning methods include a fiber stretcher [36], a continuous rotating cube [37] and a polygonal mirror [38]. However, fiber stretchers suffer from stretching hysteresis and sensitivity to temperature drift, while rotating devices have high nonlinearity in group delay.

In FD-OCT, there is no actual scanner for the axial scan since no movement of a reference mirror is needed. The axial scan rate of FD-OCT is only decided by the integration time of the linear detectors. So far, ultra-high-speed FD-OCT can work at 500,000 A-lines/s by employing two high-speed linear CMOS cameras, which enable 3D imaging within 0.72 s for a region covering $4 \times 4 \text{ mm}^2$ (500 A-lines along both directions) [14]. However, it is noted that the integration time τ is proportional to the SNR of a FD-OCT, given by Eq. 2.22. Therefore, in an ultra-high-speed FD-OCT, high power is needed to guarantee the signal quality [21].

For a lateral scan, TD-OCT and FD-OCT can share the same setup to move the sample beam laterally in two orthogonal directions. Simply, a lateral scan can be realized by a pair of translation stages. Typically they can provide a minimum step size of $0.1 \text{ }\mu\text{m}$ and a translation

range to hundreds of millimeters (LSQ Series, Zaber). But the weakness of translation stages is the low repetition as stated above. For ultrahigh-speed imaging, galvo scanners could be a choice to provide fast movement of the sample beam. Galvo scanners consist of galvanometer-based motors with optical mirrors mounted on shafts, as shown in Fig. 2.9. Galvanometer-based motors are limited-rotation DC motors that drive mirrors for laser beam scanning. Due to its light weight, currently galvo scanners are able to approach 250 Hz repetition rate within $\pm 12.5^\circ$ scanning angle (GVS series, Thorlabs GmbH). However due to the pair of deflections, the side effects of using a galvo system include [39]: 1) image distortion caused by the arrangement of mirrors, indicated by the pillow-shaped field shown in Fig. 2.9; 2) varying optical distance to the object surface; 3) varying spot size due to the off-axis beam. Therefore additional work for image correction is needed. These side effects can be reduced by using an F-theta or telecentric objective (e.g. LSM series, Thorlabs GmbH). Signal postprocessing [40] could also provide a solution for image deterioration.

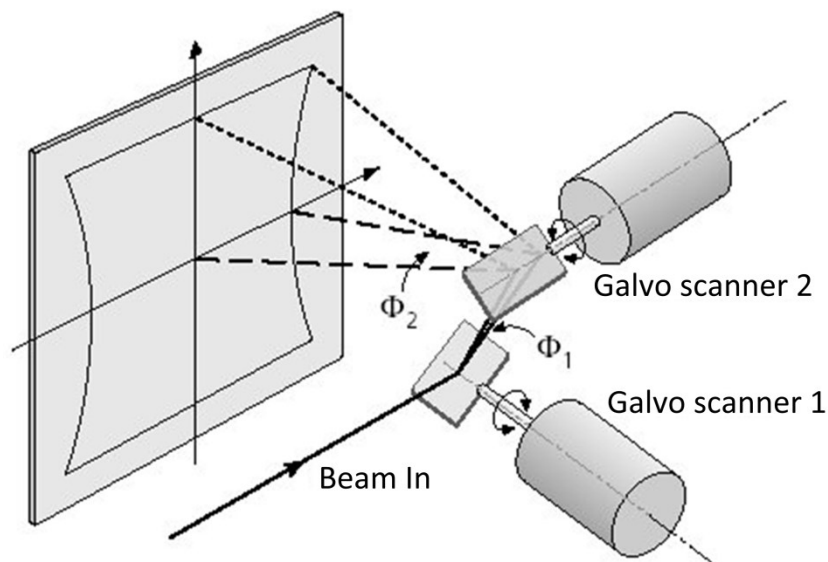


Fig. 2.9: Schematic of galvo scanning. A light beam is deflected by a pair of rotating galvo mirrors for two dimensional scanning [39].

2.4.3 Swept Source Optical Coherence Tomography

As described in section 2.3, OCT can also be performed using a swept source and a single detector in an interferometer system. This is called swept source OCT (SS-OCT) [41]. A schematic diagram of SS-OCT is shown in Fig. 2.10. As in FD-OCT, SS-OCT requires no movement of the reference mirror, however the interference spectra are measured by

sweeping the wavelength of the light source. Fourier transform is also utilized to recover the depth-resolved structure of an object.

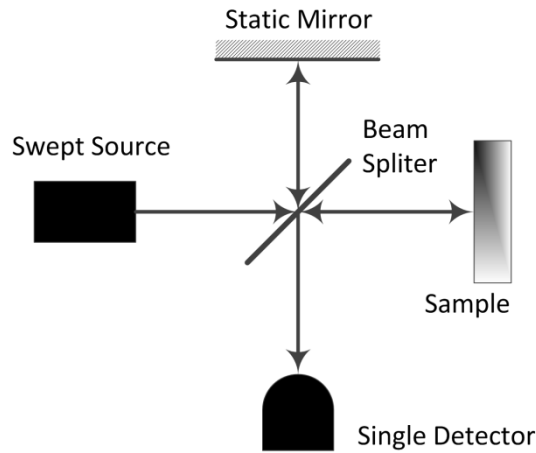


Fig. 2.10: Schematic diagram of FF-OCT system.

Compared with TD-OCT and FD-OCT, SS-OCT can be treated as a new generation OCT modality due to its superior performance. Similar to FD-OCT, one strength of SS-OCT is high-speed imaging. The introduction of Fourier-domain mode-locked (FDML) swept sources made A-scan rates of 326 kHz available for the first time [42]. Besides, SS-OCT also discards the drawbacks of FD-OCT, e.g. the spectral limitation of linear detectors and imaging depth limitations due to finite detector elements [43]. The only obstacle of SS-OCT is that the optical source has a high cost and so far is not so reliable in operation. Presently a swept source is only available for limited range of wavelengths that are mostly centered at 1000nm and 1300 nm, with a bandwidth around 100 nm [42, 44]. This limits the penetration depth and axial resolution for imaging high scattering materials. It is expected the available spectral range and bandwidth of swept sources will be expanded in the near future.

2.4.4 Full Field Optical Coherence Tomography

Fast imaging can also be achieved by avoiding lateral scans. In an alternative OCT concept called full field OCT (FF-OCT), a CCD area camera replaces the single detector in a TD-OCT system, to enable the capture of two-dimensional en face images in a single exposure. A schematic diagram of FF-OCT is shown in Fig. 2.11. As in TD-OCT, an axial scan is implemented by translating the reference mirror. However, due to the lack of lateral scans, a three-dimensional image can be acquired in 1 s [45]. The first FF-OCT system [46] was embedded in a commercial microscopy, using infrared LED light. The lateral resolution,

decided by the objective lens and camera pixel size, was $2\ \mu\text{m}$. The axial resolution, limited by the source bandwidth, was $8\ \mu\text{m}$. Presently, this technique has also been investigated using a halogen light source [45, 47]. A source of this type is inexpensive and has an ultra-broad spectrum (around 300 nm bandwidth), resulting in an axial resolution of $0.7\ \mu\text{m}$. However, the major limitation of this OCT modality is the small lateral field of view, which is around $1\times 1\ \text{mm}^2$ [48]. To achieve en face imaging of a larger object, an extra mechanical stage is required to move the sample laterally.

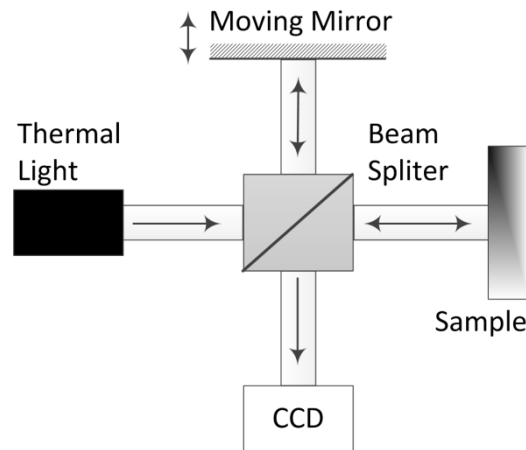


Fig. 2.11: Schematic diagram of FF-OCT system.

2.4.5 New Imaging Concepts

Besides high speed and high resolution, recording more information about the object is another direction for the development of new functional OCT modalities. For example, polarization sensitivity OCT (PS-OCT) [49], by measuring the polarization state of backreflected light from the object, gives access to additional physical parameters, like birefringence, and provides enhanced structural images that are difficult to resolve with traditional OCT techniques. One example in the NDT field is a PS-OCT system at 1550 nm that was used to investigate structural changes within bulk polymer samples during tension and fracture [50]. Spatially and temporally varying polarization patterns, due to defects and material inhomogeneities, were observed and were used to finally obtain internal stress distributions with the help of advanced image processing algorithms.

Doppler OCT (DOCT) [51], based on OCT combined with laser Doppler velocimetry (LDV), permits the quantitative imaging of fluid flow in scattering object, such as in-vivo monitoring of blood flow underneath the skin. Doppler OCT can provide this functional extension of OCT by measuring the Doppler frequency shift from moving objects. This

frequency shift can be used to determine the velocity of an object. The velocity resolution depends upon the detection electronics, scan angle and acquisition time. Recent developments [52] in this field have shown that a velocity resolution of just a few micrometers per second can be achieved.

OCT elastography (OCE) [53], is performed by speckle tracking of OCT images from an object under loading and measures the displacement field, from which the mechanical properties can be determined. Comparing with elastography based on techniques of ultrasound or magnetic resonance imaging (MRI), the most important advantage is that OCE can measure a displacement of only a few micrometers. This advantage makes OCE popular for numerous applications in the biomedical field, e.g. for measuring deformation and strain of atherosclerotic tissues, breast and brain tissues [54, 55], but OCE in material engineering field has not been reported. A detailed OCE principle description and its application for material characterization is presented in chapter 6.

2.5 Discussion and Conclusions

This chapter reviews the evolution of OCT in the past 20 years. Due to the ability to see through opaque objects and its inherent micrometer resolution, OCT has been considered as a vital measurement tool for tomographic imaging. Based on low coherence interferometry, OCT can be performed in both time domain (TD-OCT) and Fourier domain (FD-OCT). The principles of both techniques have been described and their performances were compared in detail. Generally, TD-OCT has an unlimited depth scan range and can easily achieve a high SNR with balanced detection and a bandpass filtering, while FD-OCT has an advantage in fast imaging due to no movement of the reference mirror.

The developments of OCT generally follow one principle — to obtain more information in less time. Obtaining ‘more information’ includes at first an improved resolution and penetration depth. This requires a high-quality light source that can provide a wide bandwidth for ultra-short coherence, and has a center wavelength around 1.2 - 1.8 μm to avoid strong absorption and scattering within the object. ‘More information’ can also be obtained by providing better or different contrast, such as PS-OCT and DOCT giving access to birefringence and fluid flow in objects respectively. ‘In less time’ implies high-speed imaging, which is crucial to dynamic studies and online inspection tasks. Currently real-time imaging is achievable by either TD-OCT with advanced ODL, or by new generational OCT

modalities, such as FD-OCT, SS-OCT and FF-OCT. The development of OCT modalities, together with light source and scanners are summarized in Table 2.2.

For future development of OCT, directions could be reductions in complex, size, and cost. Due to the need of in-situ imaging for biomedical studies or industrial tests, a compact and robust system, such as handheld OCT [56], is essential for this type of applications. It is also noted the most technique advances so far in OCT are driven by biomedical applications. Although some of them can be transferred or used directly for NDT applications, OCT specialized for NDT is needed for better measurement. For example, the incident power on a human tissue is limited to the microwatt range for safety reasons [57]. However in the NDT field, higher powers can be used for improved SNR. Besides, most biomedical tissues contain a lot of water that has strong absorption bands at, e.g. 1440 nm, 1930 nm, and generally the water absorption increases with the longer light wavelength [58], which limits the source selection for biomedical applications. However, this is not a problem in the NDT field [59] for solid materials, such as glass fiber composite. Light sources with longer wavelengths can be used for less scattering and hence better penetration depth.

Table 2.2: A summary of OCT development

	Function	Light Source	Scanner
TD-OCT	Structural imaging by sweeping reference mirror in a low-coherence interferometer.	Near infrared light with broad bandwidth: 1. SLD: simple and low cost. 2. Femtosecond: high power, wide bandwidth but complex.	Slow imaging due to the sweeping of the reference mirror. Advanced scanners such as gating based ODL can reach 4000 A-scans/s.
FD-OCT	Structural imaging using spectrometer combined with Fourier transform for A-scan in one shot.	Same as TD-OCT.	Fast imaging decided by the CCD integration time. 500,000 A-scans/s achieved.
SS-OCT	Structural imaging using swept source combined with Fourier transform for A-scan.	Swept source such as FDML, mostly centered at 1 and 1.3 μm .	Fast imaging decided by the sweeping rate of light source. 326,000 A-scans/s achieved.
FF-OCT	Structural imaging using area CCD for en face imaging in one shot.	Mostly halogen light which has a bandwidth more than 300 nm, providing submicrometer resolution.	Fast imaging decided by the integration time and the sweeping of reference mirror. A volumetric image can be acquired in 1s.
PS-OCT	Enhanced structural imaging with birefringence information by measuring polarization state.	Decided by the basic OCT modality used (TD, FD, SS or FF-OCT).	Decided by the basic OCT modality used.
DOCT	Flow velocity measurement using OCT combined with LDV	Decided by the basic OCT modality used.	Decided by the basic OCT modality used.
OCE	Mechanical properties measurement using OCT combined with elastography	Decided by the basic OCT modality used.	Decided by the basic OCT modality used.

References

- [1] D. Huang, E. Swanson, C. Lin *et al.*, "Optical coherence tomography," *Science*, 254(5035), 1178-1181 (1991).
- [2] T. Li, A. Wang, K. Murphy *et al.*, "White-light scanning fiber Michelson interferometer for absolute position-distance measurement," *Optics Letters*, 20(7), 785-787 (1995).
- [3] H. Maruyama, S. Inoue, T. Mitsuyama *et al.*, "Low-Coherence Interferometer System for the Simultaneous Measurement of Refractive Index and Thickness," *Applied Optics*, 41(7), 1315-1322 (2002).
- [4] M. Wojtkowski, R. Leitgeb, A. Kowalczyk *et al.*, "In vivo human retinal imaging by Fourier domain optical coherence tomography," *Journal of Biomedical Optics*, 7(3), 457-463 (2002).
- [5] J. T. Oh, and S. W. Kim, "Polarization-sensitive optical coherence tomography for photoelasticity testing of glass/epoxy composites," *Optics Express*, 11(14), 1669-1676 (2003).
- [6] J. A. Izatt, M. D. Kulkarni, S. Yazdanfar *et al.*, "In vivo bidirectional color Doppler flow imaging of picoliter blood volumes using optical coherence tomography," *Optics Letters*, 22(18), 1439-1441 (1997).
- [7] N. Nishizawa, "Ultrahigh resolution optical coherence tomography," *Opto-Electronics and Communications Conference (OECC)*, 2012 17th, 584-585 (2012).
- [8] W. Drexler, and J. G. Fujimoto, "State-of-the-art retinal optical coherence tomography," *Progress in Retinal and Eye Research*, 27(1), 45-88 (2008).
- [9] M. R. Hee, [Optical coherence tomography of the eye], Massachusetts Institute of Technology (1997).

- [10] B. E. Bouma, and G. J. Tearney, [Handbook of optical coherence tomography], Marcel Dekker (2002).
- [11] J. M. Schmitt, "Optical coherence tomography (OCT): a review," *IEEE Journal of Selected Topics in Quantum Electronics*, 5(4), 1205-1215 (1999).
- [12] M. E. Brezinski, [Optical coherence tomography: principles and applications], Academic Press (2006).
- [13] A. Rollins, S. Yazdanfar, M. Kulkarni *et al.*, "In vivo video rate optical coherence tomography," *Optics Express*, 3(6), 219-229 (1998).
- [14] L. An, P. Li, T. T. Shen *et al.*, "High speed spectral domain optical coherence tomography for retinal imaging at 500,000 A-lines per second," *Biomedical Optics Express*, 2(10), 2770-2783 (2011).
- [15] L. Sang-Won, J. Hyun-Woo, A. Yeh-Chan *et al.*, "Optimization for Axial Resolution, Depth Range, and Sensitivity of Spectral Domain Optical Coherence Tomography at 1.3 μm ," *Journal of the Korean Physical Society*, 55(6), 2354 (2009).
- [16] J. Czajkowski, T. Fabritius, J. Ulański *et al.*, "Ultra-high resolution optical coherence tomography for encapsulation quality inspection," *Applied Physics B*, 105(3), 649-657 (2011).
- [17] W. Drexler, U. Morgner, F. Kärtner *et al.*, "In vivo ultrahigh-resolution optical coherence tomography," *Optics Letters*, 24(17), 1221-1223 (1999).
- [18] J. W. Goodman, [Statistical optics], Wiley-Interscience (1985).
- [19] P. H. Tomlins, and R. K. Wang, "Theory, developments and applications of optical coherence tomography," *Journal of Physics D: Applied Physics*, 38(15), 2519-2535 (2005).
- [20] D. Derickson, [Fiber optic test and measurement], Prentice Hall (1998).

- [21] J. F. De Boer, B. Cense, B. H. Park *et al.*, "Improved signal-to-noise ratio in spectral-domain compared with time-domain optical coherence tomography," *Optics Letters*, 28(21), 2067-2069 (2003).
- [22] R. Leitgeb, C. Hitzenberger, and A. F. Fercher, "Performance of fourier domain vs. time domain optical coherence tomography," *Optics Express*, 11(8), 889-894 (2003).
- [23] J. G. Fujimoto, and D. Farkas, [Biomedical optical imaging], Oxford University Press (2009).
- [24] M. Wojtkowski, "High-speed optical coherence tomography: basics and applications," *Applied optics*, 49(16), D30-D61 (2010).
- [25] B. Liu, and M. E. Brezinski, "Theoretical and practical considerations on detection performance of time domain, Fourier domain, and swept source optical coherence tomography," *Journal of Biomedical Optics*, 12(4), 044007 (2007).
- [26] B. E. Bouma, L. E. Nelson, G. J. Tearney *et al.*, "Optical coherence tomographic imaging of human tissue at 1.55 μm and 1.81 μm using Er- and Tm-doped fiber sources," *Journal of Biomedical Optics*, 3(1), 76-79 (1998).
- [27] U. Sharma, E. W. Chang, and S. H. Yun, "Long-wavelength optical coherence tomography at 1.7 μm for enhanced imaging depth," *Optics Express*, 16(24), 19712-19723 (2008).
- [28] D. Stifter, "Beyond biomedicine: a review of alternative applications and developments for optical coherence tomography," *Applied Physics B*, 88(3), 337-357 (2007).
- [29] M. Wurm, K. Wiesauer, K. Nagel *et al.*, "Spectral-domain optical coherence tomography: a novel and fast tool for NDT," *IV NDT in Progress*, (2007).
- [30] H. Wang, M. W. Jenkins, and A. M. Rollins, "A combined multiple-SLED broadband light source at 1300nm for high resolution optical coherence tomography," *Optics Communications*, 281(7), 1896-1900 (2008).

- [31] T. Ko, D. Adler, J. Fujimoto *et al.*, “Ultra-high resolution optical coherence tomography imaging with a broadband superluminescent diode light source,” *Optics Express*, 12(10), 2112-2119 (2004).
- [32] B. Bouma, G. Tearney, I. Bilinsky *et al.*, “Self-phase-modulated Kerr-lens mode-locked Cr: forsterite laser source for optical coherence tomography,” *Optics Letters*, 21(22), 1839-1841 (1996).
- [33] H. Kuroda, M. Baba, M. Suzuki *et al.*, “A high speed three-dimensional spectral domain optical coherence tomography with $< 2 \mu\text{m}$ axial resolution using wide bandwidth femtosecond mode-locked laser,” *Applied Physics Letters*, 102(25), 251102 (2013).
- [34] B. J. Kaluzny, M. Gora, K. Karnowski *et al.*, “Imaging of the lens capsule with an ultra-high-resolution spectral optical coherence tomography prototype based on a femtosecond laser,” *British Journal of Ophthalmology*, 94(3), 275-277 (2010).
- [35] Y. Pan, E. Lankenou, J. Welzel *et al.*, “Optical coherence-gated imaging of biological tissues,” *IEEE Journal of Selected Topics in Quantum Electronics*, 2(4), 1029-1034 (1996).
- [36] L. Yan, X. S. Yao, L. Lin *et al.*, “Improved fast scanning delay line in optical coherence tomography applications utilizing fiber stretcher,” *Optical Engineering*, 47(10), 100501-100501-3 (2008).
- [37] J. Szydlo, N. Delachenal, R. Gianotti *et al.*, “Air-turbine driven optical low-coherence reflectometry at 28.6-kHz scan repetition rate,” *Optics Communications*, 154(1), 1-4 (1998).
- [38] N. Delachenal, R. Wälti, R. Gianotti *et al.*, “Robust and rapid optical low-coherence reflectometer using a polygon mirror,” *Optics Communications*, 162(4), 195-199 (1999).
- [39] Laser scanners, <http://www.zamisel.com/SSpostavka2.html>.
- [40] V. Westphal, A. Rollins, S. Radhakrishnan *et al.*, “Correction of geometric and

- refractive image distortions in optical coherence tomography applying Fermat's principle,” *Optics Express*, 10(9), 397-404 (2002).
- [41] S. Chinn, E. Swanson, and J. Fujimoto, “Optical coherence tomography using a frequency-tunable optical source,” *Optics Letters*, 22(5), 340-342 (1997).
- [42] R. Huber, D. Adler, V. Srinivasan *et al.*, “Fourier domain mode locking at 1050 nm for ultra-high-speed optical coherence tomography of the human retina at 236,000 axial scans per second,” *Optics Letters*, 32(14), 2049-2051 (2007).
- [43] P. Targowski, M. Góra, and M. Wojtkowski, “Optical coherence tomography for artwork diagnostics,” *Laser Chemistry*, 2006, 1-11 (2006).
- [44] Overview of polarization-maintaining single mode optical fiber, http://www.thorlabs.com/newgrouppage9.cfm?objectgroup_id=1596.
- [45] A. Dubois, G. Moneron, K. Grieve *et al.*, “Three-dimensional cellular-level imaging using full-field optical coherence tomography,” *Physics in Medicine and Biology*, 49(7), 1227 (2004).
- [46] E. Beaurepaire, A. C. Boccara, M. Lebec *et al.*, “Full-field optical coherence microscopy,” *Optics Letters*, 23(4), 244-246 (1998).
- [47] E. Dalimier, and D. Salomon, “Full-field optical coherence tomography: a new technology for 3D high-resolution skin imaging,” *Dermatology*, 224(1), 84-92 (2012).
- [48] A. Dubois, and A.-C. Boccara, [Full-field optical coherence tomography], Springer (2008).
- [49] J. F. de Boer, and T. E. Milner, “Review of polarization sensitive optical coherence tomography and Stokes vector determination,” *Journal of Biomedical Optics*, 7(3), 359-71 (2002).
- [50] D. Stifter, E. Leiss-Holzinger, Z. Major *et al.*, “Dynamic optical studies in materials testing with spectral-domain polarization-sensitive optical coherence

- tomography,” *Optics Express*, 18(25), 25712-25725 (2010).
- [51] V. Yang, M. Gordon, B. Qi *et al.*, “High speed, wide velocity dynamic range Doppler optical coherence tomography (Part I): System design, signal processing, and performance,” *Optics Express*, 11(7), 794-809 (2003).
- [52] R. A. Leitgeb, R. M. Werkmeister, C. Blatter *et al.*, “Doppler Optical Coherence Tomography,” *Progress in Retinal and Eye Research*, 41, 26-43 (2014).
- [53] J. M. Schmitt, “OCT elastography: imaging microscopic deformation and strain of tissue,” *Optics Express*, 3(6), 199-211 (1998).
- [54] J. Rogowska, N. Patel, J. Fujimoto *et al.*, “Optical coherence tomographic elastography technique for measuring deformation and strain of atherosclerotic tissues,” *Heart*, 90(5), 556-562 (2004).
- [55] C. Sun, B. Standish, and V. X. Yang, “Optical coherence elastography: current status and future applications,” *Journal of Biomedical Optics*, 16(4), 043001 (2011).
- [56] W. Jung, J. Kim, M. Jeon *et al.*, “Handheld optical coherence tomography scanner for primary care diagnostics,” *IEEE Transactions on Biomedical Engineering*, 58(3), 741-744 (2011).
- [57] W. Drexler, U. Morgner, R. K. Ghanta *et al.*, “Ultrahigh-resolution ophthalmic optical coherence tomography,” *Nature Medicine*, 7(4), 502-507 (2001).
- [58] G. M. Hale, and M. R. Querry, “Optical constants of water in the 200-nm to 200- μm wavelength region,” *Applied Optics*, 12(3), 555-563 (1973).
- [59] S. Zhong, Y.-C. Shen, L. Ho *et al.*, “Non-destructive quantification of pharmaceutical tablet coatings using terahertz pulsed imaging and optical coherence tomography,” *Optics and Lasers in Engineering*, 49(3), 361-365 (2011).

3

Development of a Hybrid OCT System

3.1 Introduction

As discussed in Chapter 2, current commercial OCT instruments are mostly designed for biomedical applications. These systems use light sources centered typically at 800 nm or 1300 nm, with an incident power in the microwatt range. These parameters are not suitable for a reasonable penetration depth of 2-3 mm or good SNR in scattering materials such as glass fiber composite. Recent reports [1, 2] have shown the detectable depth in polymer-based materials is enhanced or even doubled when a light source around 1550 nm is used, compared with one around 840 nm. Besides, in some case it is necessary to tailor an OCT system towards one particular application, e.g. inline characterization of specimens at the production site, or combining the OCT test with mechanical loadings. Most commercial OCT systems are desktop instruments that can have few degrees of freedom.

In this chapter, a customized OCT system for non-destructive testing, especially for polymer-based material characterization is described. An overview of the design is introduced first, including a schematic of the system. Then each component used in the system is described in detail, together with a discussion of their influence on the overall OCT system performance. The specific implementation of the measurement using the customized OCT system is given at the end of this chapter.

3.2 System Overview

For this study, a compact and robust fiber-optic OCT system was built as shown in Fig. 3.1 and Fig. 3.2. A key feature of the instrument is that it integrates TD-OCT and FD-OCT into

one system so the individual strengths of each design can give an advantage to different applications. Fig. 3.1 shows a schematic of the developed OCT system [3], and Fig. 3.2 is a photography showing the experimental setup on the optical table.

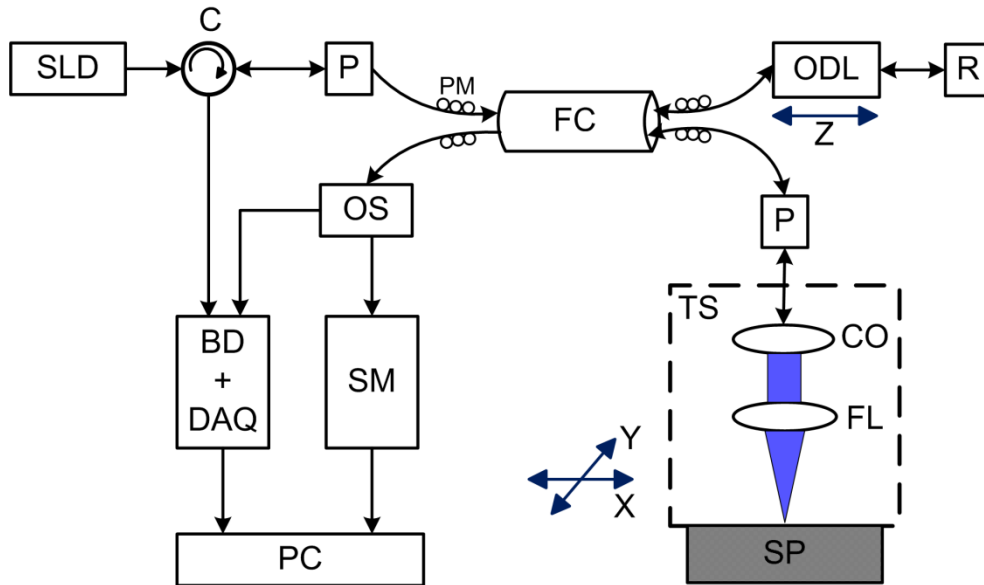


Fig. 3.1: Schematic setup of a hybrid TD-FD-OCT. Abbreviations: SLD, superluminescent diode; C, Circulator; P, polarizer; PM, polarization maintaining optical fibers; FC, fiber coupler; ODL, optical delay line; R, reflector; CO, collimator; FL, Focusing Lens; TS, translation stage; SP, sample; OS, optical switch; BD, balanced detector; DAQ, data acquisition board; SM, spectrometer; PC, personal computer. X and Y are the two orthogonal lateral directions indicating the movement of the translation stages, and Z is the axial direction indicating the movement of ODL.

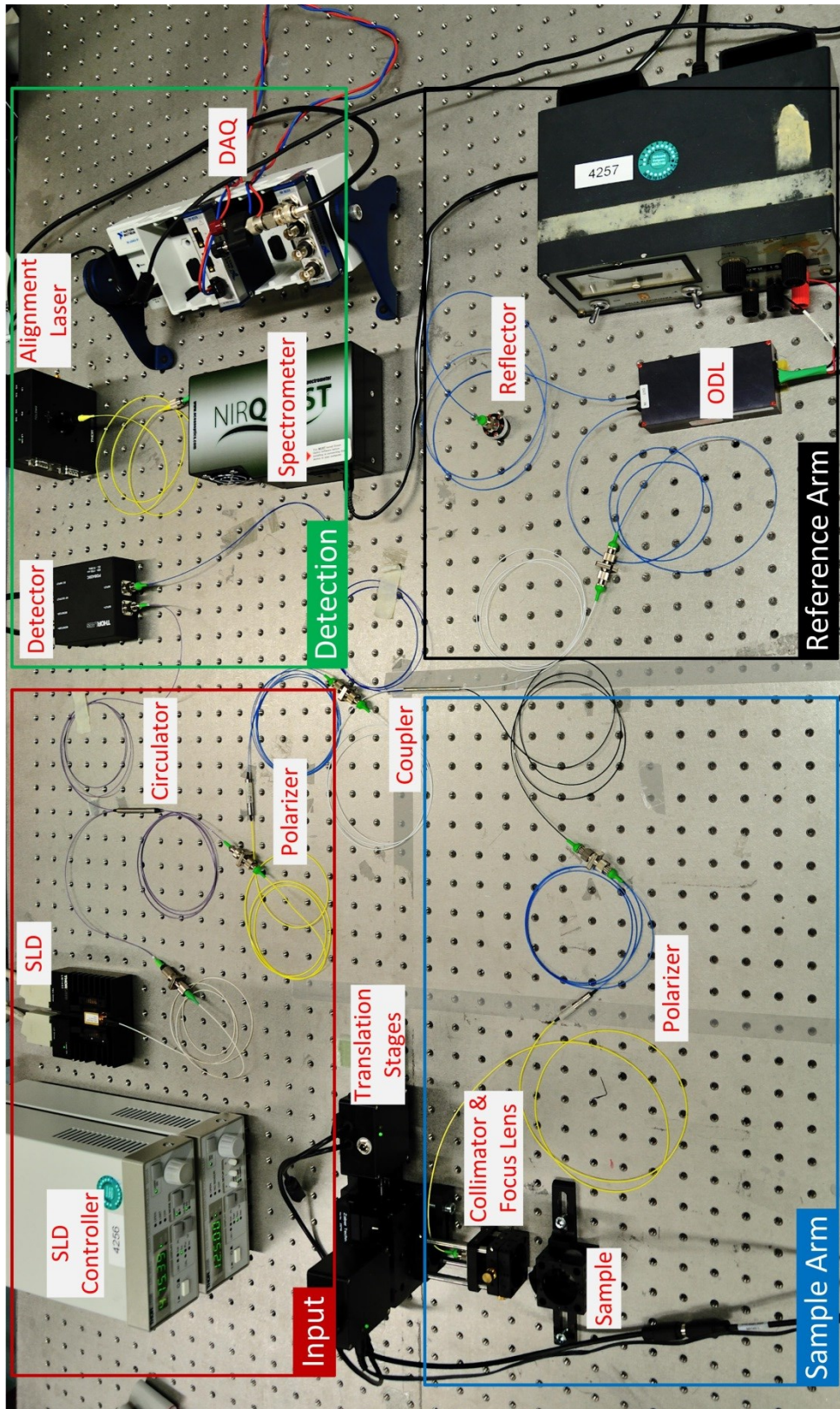


Fig. 3.2: Experimental setup on an optical table.

The technique is based on low coherence interferometry and is implemented in fiber optics. The light beam from a superluminescent diode (SLD, FESL-1550-20-BTF, Frankfurt

Laser Company, Germany), passes through a circulator (6015-3-APC, Thorlabs GmbH, Germany) and is linear polarized by an optical polarizer (FOP-21-11-1550, OZ Optics Ltd, Canada). It is then coupled with a fiber coupler (FUSED-22-1550-8/125-50/50-PM, OZ Optics Ltd, Canada) and divided into reference and sample arms with equal optical power. In the reference arm, light travels through an optical delay line (ODL-650-MC, OZ Optics Ltd, Canada) and arrives in front of a reflector (FORF-11P-1550, OZ Optics Ltd, Canada), where it is reflected back along the same path to the fiber coupler. In the sample arm, Light passing through a second polarizer is collimated by a collimation lens (F260APC-1550, Thorlabs GmbH, Germany) and then focused to the specimen by a achromatic doublet lens (AC254-030-C-ML, Thorlabs GmbH, Germany). It is then reflected from the sample and travels back to the same fiber coupler, where it is combined with backreflected reference light and is split again. Half of the light goes back to the circulator and is directed to one input of the balanced detector (PDB420C, Thorlabs GmbH, Germany). Another half goes to an optical switch (OSW22-1310E, Thorlabs GmbH, Germany), which based on the testing request could either direct the recombined light to the second input of the balanced detector for time-domain measurement or feed the light into a spectrometer (NIRQuest512, Ocean Optics Inc, US) for Fourier-domain measurement. During an experimental test, this can also be realized by simply connecting the output fiber with the balanced detector or spectrometer manually without the optical switch, as shown in Fig. 3.2.

For TD-OCT, using the scan of the reference mirror in an optical delay line to change the reference pathlength, a set of interferometric signals will be detected as a function of the reference mirror position. This set corresponds to the axial distribution of scattering interfaces within the specimen and is referred to as an A-scan. While for FD-OCT, spectral intensities are measured at one shot without the movement of reference mirror. In FD-OCT the A-scan signal is recovered by inverse Fourier transform, as described in section 2.2.2. By laterally shifting the probe beam with a pair of orthogonal translation stages (T-LS28M, Zaber Inc, Canada), a set of consecutive A-scans can be obtained. These A-scans are then combined to form a cross sectional image of the structure, which is named a B-scan. A volumetric image can be reconstructed as well by combining a succession of B-scans.

3.3 Detail of components

3.3.1 Light Source

The OCT system uses a fiber-coupled low-coherence superluminescent diode (SLD, FESL-1550-20-BTF, Frankfurt Laser Company, Germany) as the light source. The use of an

SLD is due to its advantages of simplicity, stability, and low cost, compared with its counterpart, e.g. femtosecond lasers, as discussed in chapter 2. SLD is also ideal for the design of a portable OCT system which enables the measurement in situ. Besides, the selected SLD can satisfy the power and wavelength requirement for the customized OCT system, as described below.

As shown in Fig. 3.2, the SLD is located in a diode mount (LM14S2, Thorlabs GmbH, Germany) which is driven by a temperature controller (TED200C, Thorlabs GmbH, Germany) and a current controller (CAB400, Thorlabs GmbH, Germany). The current controller can increase the current from 0 to 500 mA, resulting in a proportionally growing output power of the SLD, as shown in Fig. 3.3(a) [4]. The maximum power of light source is 20 mW, and the power of light finally emitted on the specimen is 2 mW. Besides the fiber coupler that directs half the power of the light to the reference arm, the power loss of the sample beam is mainly from the polarization control and the optical fiber connectors. However, a 2 mW sample beam is much stronger than the biomedical counterparts, resulting in a higher SNR that allows weak reflections from deep (e.g. 2-3 mm) of a scattering sample to be detected. A quantitative comparison of SNR with regard to source power is given in chapter 4.

The SLD has a center wavelength of 1550 nm, which is less scattering and gives deeper penetration in polymer-based material than the shorter wavelength used for biomedical applications [1]. The light source has a FWHM (Full Width at Half Maximum) of 60 nm. According to Eq. 2.16, it can provide a theoretical axial resolution of 17 μm in the air, and 11 μm in the polymer material with a 1.55 average refractive index taken into account. However, it is noted that the spectral distribution of the light source is not exactly a Gaussian shape but has small spectral ripples, as shown in Fig. 3.3(b) and (c) [4]. This type of imperfect light source could bring artifacts into the interference signal, which is evaluated in the next chapter.

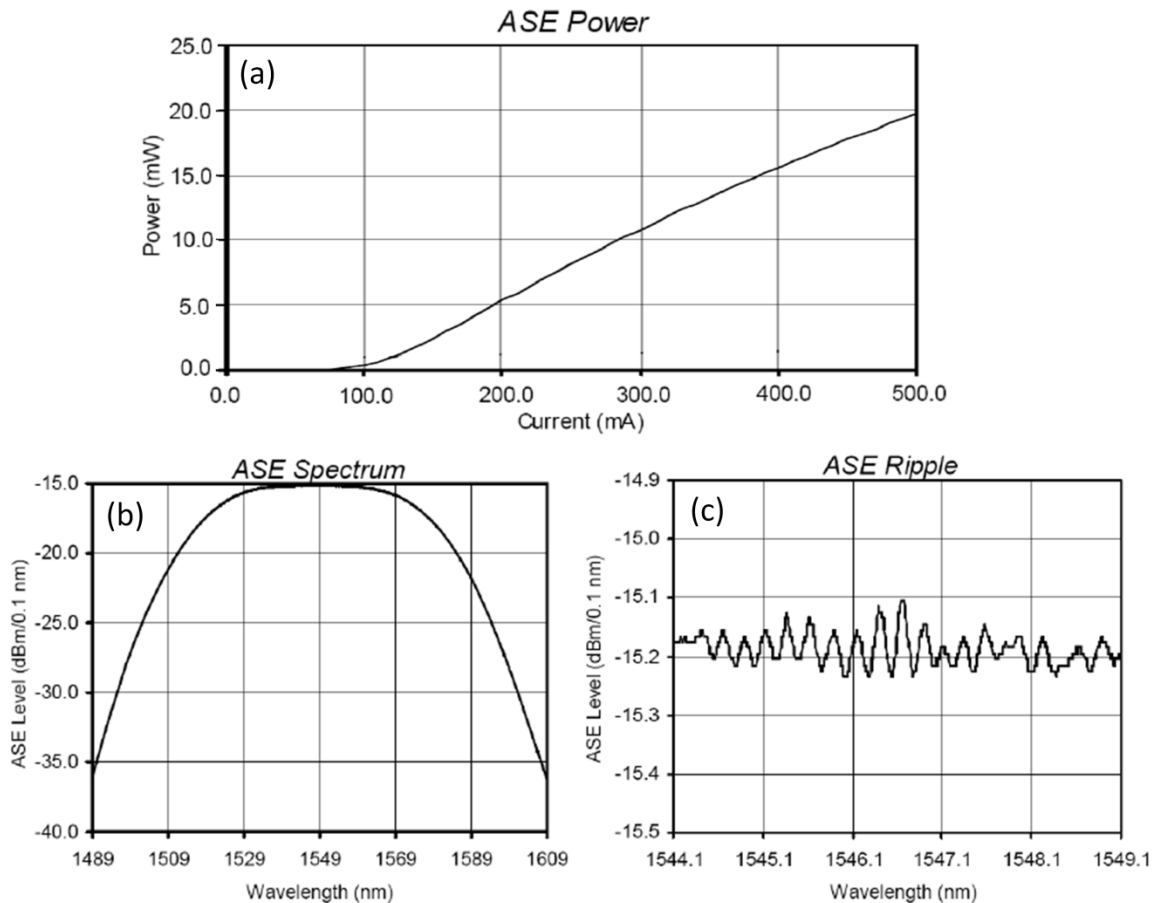


Fig. 3.3: Performance of the SLD [4], including (a) optical power, (b) spectrum distribution, and (c) spectrum ripple. ASE: amplified spontaneous emission.

3.3.2 Optical Fiber

Light emitted from SLD is conducted through single-mode fibers in the OCT system. The use of fiber optics instead of bulk optics in free space is due to their convenience and ease of alignment. The difference between single-mode and multimode fiber is shown in Fig. 3.4(a) [5]. Single-mode fiber only support one propagation mode due to its relatively small core (approximately 10 μm) and a small refractive index difference between core and cladding (for a larger critical angle during total internal reflection). Therefore single-mode fiber enables the spatial coherence of light to be retained, which is crucial for an interferometer system.

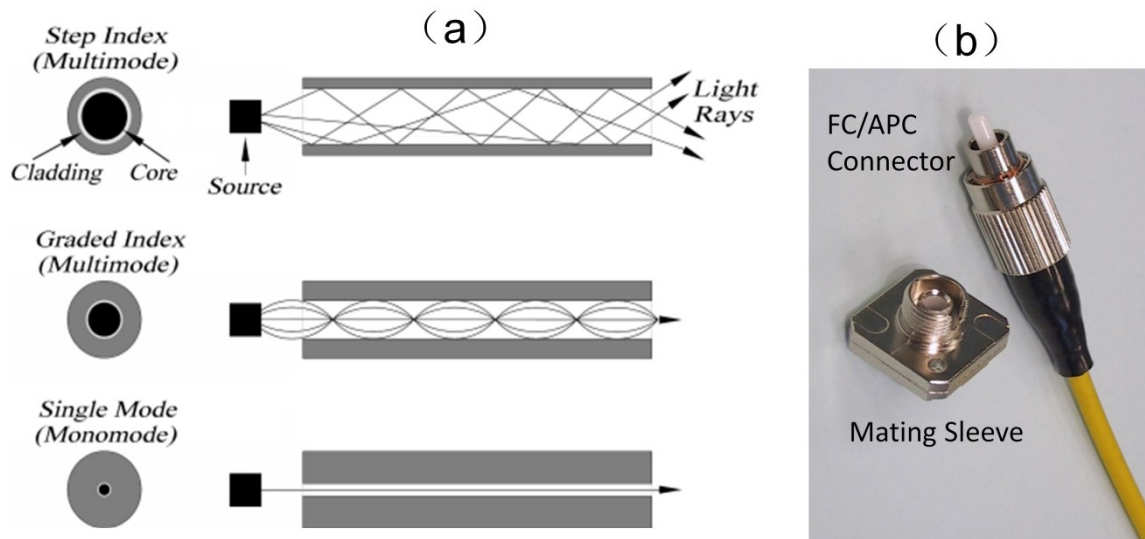


Fig. 3.4: (a) schematic diagrams for light transmitting in multimode and single mode fiber [5] and (b) a FC/APC fiber connector and a mating sleeve used in the OCT system to connect components.

To connect each component, FC/APC connectors and mating sleeves are used, as shown in Fig. 3.4(b). FC stands for ferrule connector while APC stands for angled physical contact. These connectors allow the surfaces of two connected fibers to be in direct contact with each other and the fiber end is polished at an angle. The physical contact can reduce the light power loss while the angled fiber end (with a 8° angled ceramic ferrule) can prevent reflected light traveling back to the fiber, which can eliminate artifacts in the interference signal. Additionally, to match the pathlengths of the reference and sample arms, a customized length of fiber is needed. A manual describing the customization of fibers with connectors is introduced in [6].

3.3.3 Interferometer

The interferometer configuration employed in the OCT system is a fiber-optic Michelson interferometer. The core of the interferometer system is a fiber coupler (FUSED-22-1550-8/125-50/50-PM, OZ Optics Ltd, Canada), which is equivalent to an optical beam splitter in free space. As shown in Fig. 3.2, a fiber coupler is generally a four-port device consisting of two fibers. These fibers are fused together, etched or polished over a small interaction region where the exchange of power between each fiber core occurs [7]. In the designed Michelson interferometer, the fiber coupler splits the power of the input light source equally between reference and sample arms and combines the backreflected reference

and sample light. It then divides the power of combined light into two halves again to the balanced detector or spectrometer.

It is noted that some interferometer designs based on a Mach-Zehnder interferometer have been proposed for OCT [8]. As shown in Fig. 3.5, OCT systems of this type utilize two fiber couplers to divide the optical source and to combine the backreflected reference and sample beams. The first fiber coupler could be unbalanced to direct more light power to the sample arm. This is done to optimize the imaging performance since the SNR of an OCT image is proportional to the power of sample backreflection (Eq. 2.21), which is substantially less than reference signal. However, this design requires an additional fiber coupler, compared with the Michelson interferometer. The velocity of the ODL, introduced in section 3.3.7, would also be cut to half due to the one-way reflection.

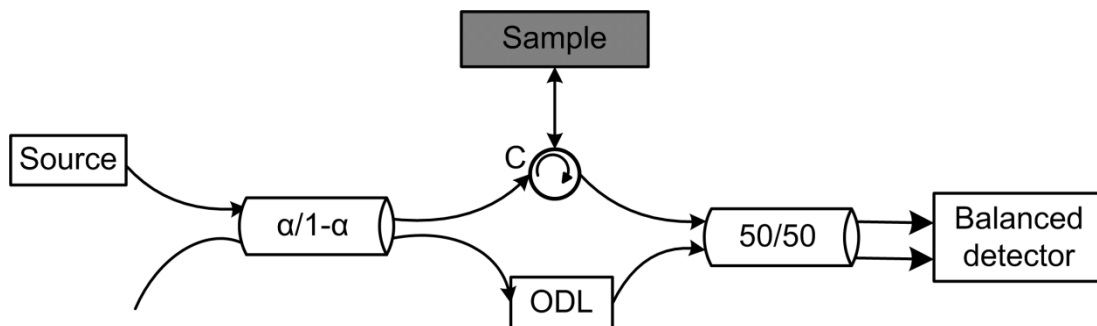


Fig. 3.5: Schematic diagram of a Mach-Zehnder interferometer. α denotes the light splitting ratio.

3.3.4 Polarizer and Polarization Maintaining Fiber

An electromagnetic wave, such as light, is composed of an electric field and a magnetic field that travel together at the same velocity and direction, but oscillate perpendicularly. Once we know the electric field we can easily determine the magnetic field. Thus we usually deal only with electrical field and define light polarization as the oscillation orientation of its electrical field. In an interferometer system, the matching of polarization states of the combined light is one of the elements that decide the interference quality. The interference signal is strongest when the two light beams have some polarization states. It decays with the increase of the polarization difference and vanishes if the two polarizations are perpendicular.

It is worth mentioning that standard optical fibers always exhibit random birefringence due to mechanical stress and geometric effects such as bending [9]. Birefringence could also occur in the tested specimens. It is a phenomenon that light travelling in certain types of

materials is split into two orthogonal polarization components with different velocities. As a consequence, in OCT, interferences could occur under both polarization states and be recorded at different depth locations, which brings in artifacts in the final structural image.

To obtain an interference signal with good quality, the light backreflected from the reference mirror and the specimen have to have the same polarization state. Therefore, a novel fiber polarizer (FOP-21-11-1550, OZ Optics Ltd, Canada) is employed after the SLD to restrict light to a linear polarization before going to the interferometer. A same fiber polarizer is used in the sample arm to polarize the backreflected sample light to its original state. As depicted in Fig. 3.6, a fiber polarizer of this type allows only the light components with one linear polarization state to be transmitted. The light components with an orthogonal polarization state are absorbed by a crystal or a thin film placed over the fiber core [10].

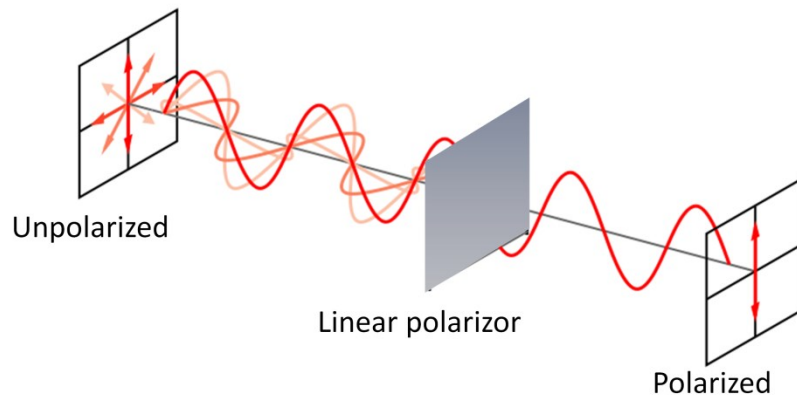


Fig. 3.6: A linear polarizer filters an unpolarized beam into one with a single linear polarization. Light travels from left to right and the arrows depict the electric field vector.

Besides, to retain the linear polarization state, all the single-mode fibers in the interferometer have to be polarization maintaining (PM). Generally PM fiber (PMF-1550-8/125-0.25-L, OZ Optics Ltd, Canada) has a pair of stress rods running parallel to the fiber core. These stress rods intentionally creates consistent birefringence pattern along its length, prohibiting coupling between the two orthogonal polarization directions [11].

3.3.5 Circulator and Optical Switch

A fiber optic circulator (6015-3-APC, Thorlabs GmbH, Germany) is a passive, three-port device that acts as a signal router. As shown in Fig. 3.7, light from the input fiber 1 is directed from port 1 to port 2, where light is coupled into the interferometer system, returned back, and

redirected to a third port. Light input into port 1 will not be coupled into the port 3 fiber, and light input into port 2 will not be coupled into the port 1 fiber. Therefore, the fiber circulator used in the system could play two functions. It directs the interference signal to the second input of the detector for balanced detection. It could also act as an optical isolator to resist light returning back to the source and protect the SLD module from being damaged by optical feedback.

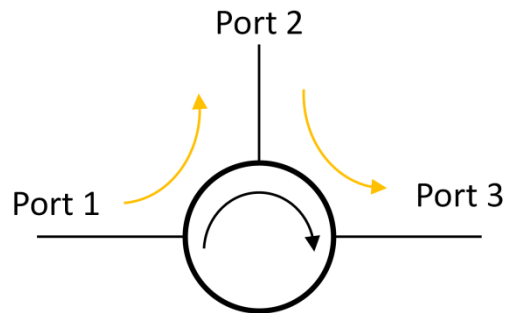


Fig. 3.7: Schematic diagram of an optical circulator.

Fig. 3.8 shows the fiber optical switch (OSW22-1310E, Thorlabs GmbH, Germany) used the hybrid OCT system. The light from the input fiber can be directed to either of the two output fibers by an optical switch with an integrated control circuit. The switching mechanism is based on silicon Micro-Electro-Mechanical Systems (MEMS) technology, which ensures exceptionally low crosstalk between channels, and is inherently fast (switching time $<1\text{ms}$) [12]. The switching can be easily operated by toggle button on the circuit board or be remotely controlled by software from a PC. In the final design of the integrated OCT prototype, the optical switch decides if TD-OCT or FD-OCT will be applied for the measurement by directing the interference signal to either the balanced detector or the spectrometer.

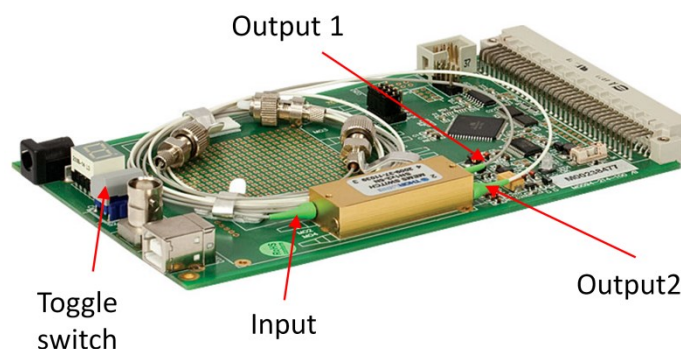


Fig. 3.8: A fiber optical switch with controlling circuit [12].

3.3.6 Collimator and Focusing Lens

At the end of the fiber in the sample arm, the light coming to free space is collimated by a collimator lens (F260APC-1550, Thorlabs GmbH, Germany), resulting in an output beam size of 3 mm diameter. The collimated light is then focused to the specimen by an achromatic doublet lens (AC254-030-C-ML, Thorlabs GmbH, Germany) with a 30 mm focal length. According to Eq. 2.17 to Eq. 2.19, the lateral resolution of this OCT system, decided by the spot size, is 20 μm and depth of focus is 1.24 mm. Therefore, to measure a specimen with 2-3 mm thickness, it is better to align the focus point in the middle depth to minimize the image deterioration caused by an out-of-focus measurement.

3.3.7 Optical Delay Line and Reflector

The optical delay line (ODL) in the hybrid OCT system has two functions: changing the reference pathlength for an axial scan in TD-OCT, and for placing a small offset z_0 for separating the disturbing terms in the FD-OCT signal as discussed in chapter 2. The selected ODL (ODL-650-MC, OZ Optics Ltd, Canada), as shown in Fig. 3.9 [13], is an electrically controlled, reflector-style, variable device consisting of an input fiber collimator and an output fiber coupler. The collimator projects light into free space inside the device and the coupler directs it to the output fiber. The width of the gap between the components determines the delay time through the device. The distance the light travels in free space is precisely controlled by reflecting the light from a pair of moveable mirrors, which are driven by a servo motor with a microprocessor. The microprocessor enables remote communication through an electrical device or PC.

The servo motor provides a resolution of 0.4 μm and a linear translation speed of 0.85 mm/s with maximum 25 mm travel range. In the customized OCT system shown in Fig. 3.1 and Fig. 3.2, the output of the ODL is connected to a reflector (FORF-11P-1550, OZ Optics Ltd, Canada) that enables the light to be reflected back to the entrance port of the ODL. Therefore, due to this dual path travel of light in the ODL, A-scan range and speed are doubled, which correspond to 50 mm and 1.7 mm/s respectively in air. This A-scan speed and its linearity are evaluated in chapter 4. According to Eq. 2.23, the Doppler frequency induced by the ODL is 2193 Hz. For a specimen with 2-3 mm thickness, each A-scan in TD-OCT will cost approximately 2 s.

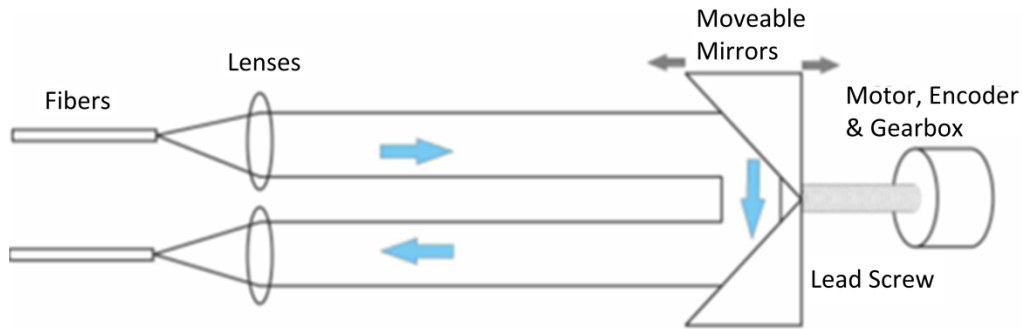


Fig. 3.9: Schematic diagram of the ODL used in the OCT system [13]. The output of the ODL is connected to a reflector that let the light travel back along the same path, which doubles the A-scan velocity and range during an OCT measurement.

In the fiber optical reflector (FORF-11P-1550, OZ Optics Ltd, Canada) shown in Fig. 3.10, a collimation lens and a static mirror are used to reflect partial light back to the fiber. The blocking screw in front of the mirror decides the attenuation of the backreflected light. Due to the strong backreflected light from the reference arm, it is sometimes necessary to attenuate the reference power to avoid saturation of the detectors.

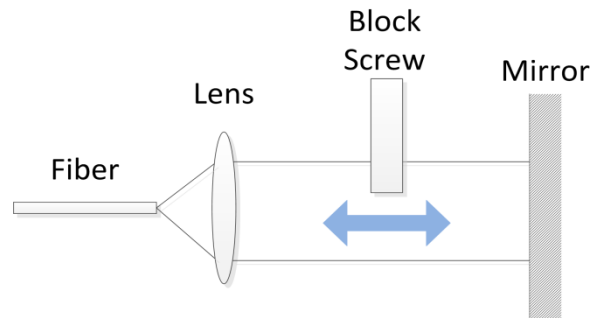


Fig. 3.10: Schematic diagram of the variable fiber optic reflector. The bidirectional arrow indicates light travelling ways.

3.3.8 Balanced Detector and DAQ Board

In TD-OCT, the interference signal is measured by a balanced photo detector (PDB420C, Thorlabs GmbH, Germany). The balanced detector consists of two photodiodes and an ultra-low-noise, high-speed transimpedance amplifier that generates an output voltage proportional to the difference between the photocurrents of the two photodiodes [14]. A schematic of the detector is shown in Fig. 3.11. The balanced photo detector acts as a balanced receiver by subtracting the two optical input signals from each other, resulting in the cancellation of common mode noise and hence gives an improved SNR of the interferometric

signal. As an example, Fig. 3.12 compares one A-scan signal acquired by the unbalanced and balanced detection (MONITOR+ and RF OUTPUT in Fig. 3.11) simultaneously. It can be seen clearly that the noise level is decreased significantly by balanced detection. A quantitative SNR of the system is calculated in the next chapter.

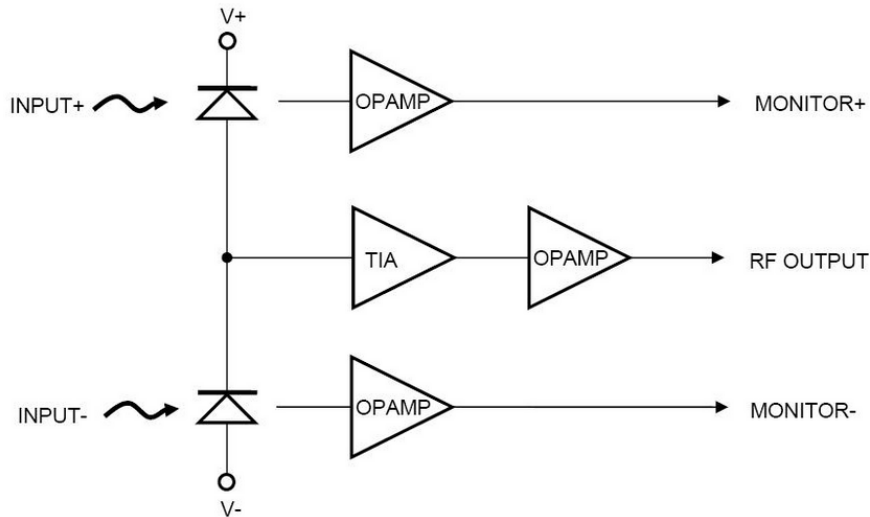


Fig. 3.11: Schematic diagram of the selected balanced detector [14]. The two optical input signals are subtracted from each other, resulting in the cancellation of common mode noise. Abbreviations: TIA: transimpedance amplifier, OPAMP, operational amplifier.

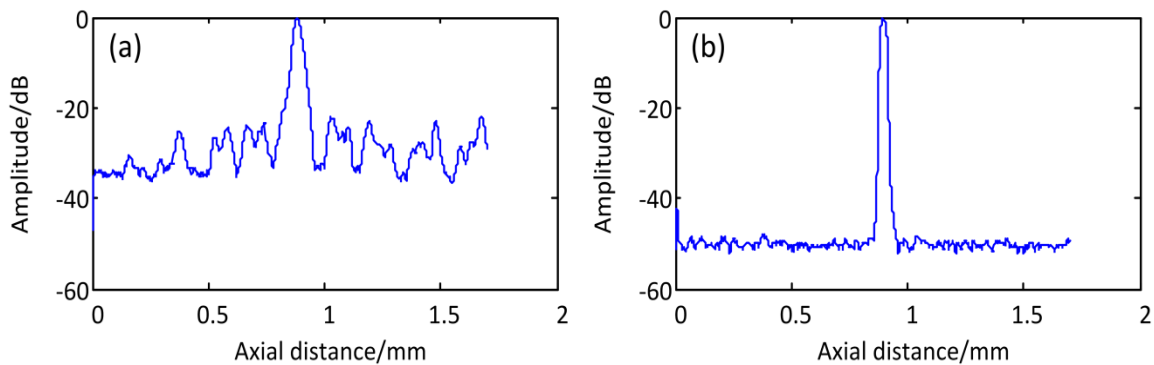


Fig. 3.12: A-scan signal acquired by (a) unbalanced and (b) balanced detection. The improvement of SNR with balanced detection can be clearly observed.

The analog voltages generated by the balanced detector need to be further captured and digitized by a data acquisition board (DAQ) before being sent to a computer. The selected DAQ board (NI 9233) can provide a 50 kS/s maximum sampling rate, which is suitable for measuring an interference signal with a modulation frequency around 2 kHz. The captured

signal is digitized with 24-bit resolution. Thus the maximum dynamic range for the displayed TD-OCT images is 72 dB, given by:

$$dy = 10\log(2^M) \quad (3.1)$$

where dy is the displayed image dynamic range and M is the bits for AD conversion. It has to be pointed out that the typically reported SNR of an OCT system above 80 dB refers to an analog signal [15]. In practice, the displayed image has a substantially reduced dynamic range due to the signal loss associated with the limitation of the AD conversion. From Eq. 3.1, it can be seen the displayed image dynamic range is proportional to the bit number M in a DAQ board.

3.3.9 Spectrometer

For FD-OCT, spectral irradiances are collected by a spectrometer (NIRQuest512, Ocean Optics Inc, US). Fig. 3.13 shows the schematic of the selected spectrometer [16]. The light source is brought into the instrument with a fiber optic cable connected to the optical probe. The amount of entering light is controlled by an adjustable slit and its wavelength range is restricted by a filter. After collimation by a mirror, the light is scattered for different wavelengths by a diffraction grating. The dispersed light falls onto a focusing mirror and is directed to an array of photodiodes, each of which responds only to the narrow range of wavelengths impinging on it. The photodiodes are connected to a charge-coupled device (CCD) that produces voltages. The voltages from each diode are converted to digital counts and sent to a dedicated computer with spectrum analysis software. The acquired spectrum is immediately displayed on the screen and saved in standard computer files.



Fig. 3.13: Light enters the spectrometer from a fiber optic cable connected to a probe (1). It is then conditioned by an adjustable slit (2), a filter (3), a collimating mirror (4), and a diffraction grating (5). The grating scatters the different wavelengths onto a focusing mirror (6) that directs the light via a collector lens (7) onto the detector array (8) [16].

The spectrometer used comprises a 512-element InGaAs array and an adjustable full spectral range for detection which is decided by the overall performance of the OCT system. In FD-OCT, the interval of image pixels in the axial direction δz is determined as the depth range z_{\max} (Eq. 2.20) divided by half of the total detector elements, given by:

$$\delta z = \frac{\lambda_0^2}{2\lambda_{full}} \quad (3.2)$$

The pixel interval δz should be smaller than half of the theoretical axial resolution Δz from Eq. 2.16 to satisfy the Nyquist sampling theory [17]. Therefore, the full spectral range λ_{full} detected by the spectrometer should satisfy:

$$\lambda_{full} \geq \frac{\pi}{2(\ln 2)} \Delta \lambda = 2.27 \Delta \lambda \quad (3.3)$$

Since the FWHM of the light source, $\Delta \lambda$ is 60 nm, λ_{full} is decided as 160 nm. Combined with 512-element detectors, a maximum detectible depth of 1.92 mm in the air can be achieved, according to Eq. 2.20. The detectible depth can be improved with more detectors (e.g. 1024 elements), but the cost would much higher as expensive InGaAs photodiodes are needed for the detection of near infrared light.

The minimum integration time set by this spectrometer is 1 ms, which means a maximum rate of 1000 A-scans/s can be achieved in the FD-OCT. For AD conversion, 16-bit resolution is used, resulting in a displayed image dynamic range of 48 dB, based on Eq. 3.1.

3.3.10 Translation Stages

For lateral scans, a pair of translation stages (T-LS28M, Zaber Inc, Canada) are used to shift the OCT probe beam in two orthogonal directions parallel to the specimen surface. These motorized stages provide 0.1 μm resolution and 28 mm travel range. The maximum translation speed is 6.5 mm/s. The units can be controlled by a PC via a single RS-232 serial port.

The use of translation stages instead of galvo mirrors could be for two reasons. Firstly, as reviewed in chapter 2, translation stages do not generate the image distortion that occurs in a galvo mirror system. So they are easy to use and no extra cost or work, e.g. telecentric lens or signal postprocessing is needed. The other reason is due to the fact that the A-scan rate in the designed OCT system is not ultra-high. The translation stages are fast enough to couple with the A-scan system. For example, considering the highest 1000 A-scans/s in FD-OCT, a cross-sectional image with 6.5 mm length can be acquired in 1s. The pixel interval in lateral direction is 6.5 μm , which enables a display of all the detailed structure of a specimen, considering 20 μm spot size of the sample beam.

A summary of the components and their performance in the OCT system are summarized in Table 3.1.

Table 3.1: Summary of the OCT Components and their performance in the integral OCT system

Components	Model and Manufacturer	Specifications	Performance in OCT
Light Source	FESL-1550-20-BTF, Frankfurt Laser Company, Germany	- 20 mW - $\lambda=1550$ nm , $\Delta\lambda =60$ nm - Close to Gaussian shape spectrum with small spectral ripples	- 2-3 mm penetration - 17 μ m axial resolution - Small artifacts in the interference signal
Interferometer	FUSED-22-1550-8/1 25-50/50-PM (coupler)	- Michelson interferometer - fiber optics - FC/APC connectors	- Simple setup - Easy for alignment - Low backreflection
Polarizer & PM Fibers	FOP-21-11-1550, OZ Optics Ltd, Canada	Linear polarization state	- High quality interference signal
Circulator & Optical Switch	6015-3-APC & OSW22-1310E, Thorlabs GmbH, Germany	- Circulator: one directional light transmission - Optical switch: fast switching (<1ms) and remote control.	- Isolation of light back to the source - Direct interference signal to the detectors
Collimator and Focusing Lens	F260APC-1550, and AC254-030-C-ML, Thorlabs GmbH, Germany	- Collimator: 3 mm collimating beam size - Focusing lens: 30 mm focus length	- 20 mm spot size (lateral resolution) - 1.24 μ m depth of focus
Optical Delay Line & Reflector	ODL-650-MC & FORF-13A-1550-S, OZ Optics Ltd, Canada	- 0.4 μ m step resolution - 0.85 mm/s with maximum 25 mm travel range - Variable backreflection - Polarization maintaining	- 1.7 mm/s A-scan speed with 50 mm scan range in TD-OCT. - Optimized imaging quality
Balanced Detector	PDB420C, Thorlabs GmbH, Germany	Balanced detection	- Improved SNR
DAQ	NI 9233, National Instruments Corp., US	- 50 KS/s Sampling rate - 24-bit AD conversion	- 72 dB displayed image dynamic range
Spectrometer	NIRQuest512, Ocean Optics Inc, US	- 512-element detectors, 160 nm detection bandwidth. - 1 ms minimum integration time - 16-bit AD conversion	- 1.92 mm axial detection range - Maximum 1000 A-scans/s in FD-OCT - 48 dB displayed image dynamic range
Translation Stages	T-LS28M, Zaber Inc, Canada	- Maximum 6.5 mm/s - 28 mm travel range	- Maximum 6.5 mm/s for lateral scan - 28x28 mm maximum imaging area.

3.4 Instrument Control Software

The implementation of the OCT measurement is based on a customized software coupled with the hybrid OCT setup. Fig. 3.14 describes the procedure for instrument control and data acquisition during the measurement. Generally, the measurement starts with instrument initialization, including locating the ODL and translation stage positions. If TD-OCT is selected for the testing, the ODL will sweep forward and back for A-scans with a range of approximately the thickness of the specimen. After finishing each A-scan, the translation stages will shift the objective beam one step laterally until it goes through the required imaging area. Simultaneously with the scanning, the DAQ system records the data which is processed afterwards. While in FD-OCT, the ODL is controlled to create a small offset (around 200 μm) between the sample and reference pathlength to separate the signal from DC noise. Due to its fast scanning property, the translation stages can move continuously and record the spectrum data simultaneously. With the signal processing algorithm described in the next chapter, the OCT image can be recovered and finally displayed.

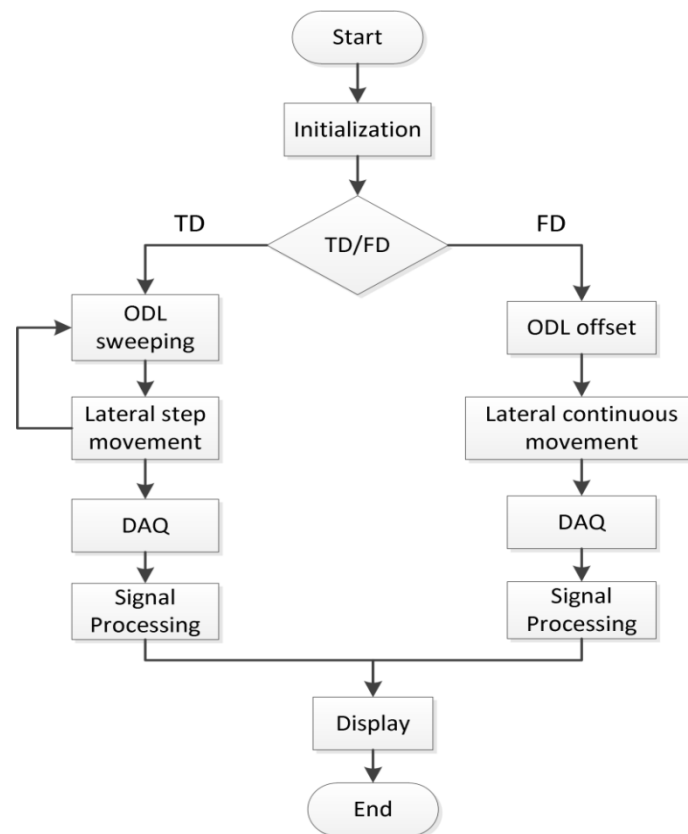


Fig. 3.14: The flow chart for the implementation of OCT measurement.

3.5 Conclusions

In summary, a hybrid TD-FD-OCT system has been built. Generally, from the hardware point of view, TD-OCT has the advantage of a large A-scan range (50 mm in the air) and substantial noise reduction by balanced detection, while FD-OCT system owns its tremendous superiority in fast imaging (1000 A-scans/s) due to no movement of the reference mirror. These two kinds of measurement can be implemented based on the user request, e.g. imaging depth and speed.

The detail of the components and their performance in the OCT system were summarized in Table 3.1. Generally, fiber optic interferometry with a light source centered at 1550 nm is used, expecting a high SNR and thus deep penetration in scattering material. In TD-OCT, an electrical ODL is equipped in the reference arm to sweep the pathlength at 1.7 mm/s, and a balanced detector is applied to receive signal from two inputs for noise reduction. In FD-OCT, a spectrometer with 160 nm spectral range and 512 detector elements is employed, reaching 1000 scans/s and 1.92 mm axial scan range. For both TD and FD-OCT, a pair of translation stages with 6.5 mm/s velocity and 28 mm travelling range, are used to shift the sample beam for the lateral scan. However, it is necessary to point out that the overall selection of the components is based on the cost, specifications, availability in the lab, and operability for coupling into the OCT system. The performance of the OCT system could be much improved by replacing selected components with the higher-performance counterparts, but this would greatly increase the total cost of the OCT system.

References

- [1] D. Stifter, "Beyond biomedicine: a review of alternative applications and developments for optical coherence tomography," *Applied Physics B*, 88(3), 337-357 (2007).
- [2] M. Wurm, K. Wiesauer, K. Nagel *et al.*, "Spectral-domain optical coherence tomography: a novel and fast tool for NDT," *IV NDT in Progress*, (2007).
- [3] P. Liu, R. M. Groves, and R. Benedictus, "Signal processing in optical coherence tomography for aerospace material characterization," *Optical Engineering*, 52(3), 033201 (2013).

- [4] [Ultra high power cooled fiber-coupled superluminescent diode FESL-1550-20-BTF], Frankfurt Laser Company (2008).
- [5] Using ethernet with fiber optics - achieving longer distances and superior noise immunity, http://www.industrialethernetu.com/courses/301_2.htm.
- [6] [Guide to connectorization and polishing of optical fibers], Thorlabs Inc. (2013).
- [7] V. J. Tekippe, D. R. Moore, D. K. Paul *et al.*, "Production, performance, and reliability of fused couplers," International Conference on Fiber Optics and Photonics: Selected Papers from Photonics India'98, 56-61 (1999).
- [8] A. M. Rollins, and J. A. Izatt, "Optimal interferometer designs for optical coherence tomography," *Optics Letters*, 24(21), 1484-1486 (1999).
- [9] R. Ulrich, S. Rashleigh, and W. Eickhoff, "Bending-induced birefringence in single-mode fibers," *Optics Letters*, 5(6), 273-275 (1980).
- [10] P. Perumalsamy, [In-line Fiber Polarizer], Virginia Polytechnic Institute and State University (1998).
- [11] Overview of polarization-maintaining single mode optical fiber, http://www.thorlabs.com/newgrouppage9.cfm?objectgroup_id=1596.
- [12] [OSW12(22)-xxxE series operation manual], Thorlabs GmbH (2012).
- [13] [Operating instructions for optical delay line ODL-650-MC], OZ Optics Ltd. (2011).
- [14] [Operation manual for balanced amplified photodetectors PDB400 series], Thorlabs GmbH (2010).
- [15] B. Liu, and M. E. Brezinski, "Theoretical and practical considerations on detection performance of time domain, Fourier domain, and swept source optical coherence tomography," *Journal of Biomedical Optics*, 12(4), 044007 (2007).
- [16] Ocean optics, <http://www.oceanoptics.com/>.

- [17] M. Wojtkowski, V. Srinivasan, T. Ko *et al.*, “Ultrahigh-resolution, high-speed, Fourier domain optical coherence tomography and methods for dispersion compensation,” *Optics Express*, 12(11), 2404-2422 (2004).

4

Design of Signal Processing

This chapter is partly reproduced from:

- P. Liu, R. M. Groves, and R. Benedictus, “Signal processing in optical coherence tomography for aerospace material characterization,” *Optical Engineering*, 52(3), 033201 (2013).

4.1 Introduction

In chapter 3, the hybrid TD-FD-OCT system was described. The measurement data from this instrument needs to be further processed to reconstruct a cross-sectional or volumetric image. For example, during a TD-OCT measurement, the axial interferogram is modulated by Doppler frequency shifting, induced by the movement of the reference arm. Typically this demodulation is carried out by fixed electronics in an analog way. The general AM (Amplitude Modulated) demodulation method, mixing, is the most used technique [1]. It implements signal multiplication with a reference sinusoidal signal of the correct phase, followed by lowpass filtering. However, sometimes this approach does not generate a perfect signal envelope due to the variation of the carrier frequencies induced by nonlinear sweeping of the reference mirror. Digital signal processing techniques for OCT signal demodulation are rarely studied and the only detailed publication that can be found was published by D. C. Adler in 2004 [2]. Methods such as boxcar averaging, coherence, and Hilbert transform were investigated with simulated data in this paper. However, they did not consider the noise coupled in the signal, which has a large influence on the accuracy of the demodulation.

On the contrary, instead of containing a signal modulation, A-scan data from FD-OCT measurement is in the spectral domain. To recover a depth profile, an additional Fourier transform is needed. Considering that in FD-OCT, the data is normally collected using evenly spaced intervals of wavelength λ , a resampling is necessary, based on Eq. 2.15, to shift the spectral data into an evenly spaced data in the wavenumber k domain, where $k = 2\pi / \lambda$. Besides, as introduced in chapter 2, the lowpass filtering property of the Fourier transform allows in a high level of classical noise and the use of CCD detectors also brings in extra noise, e.g. dark noise. These additional noise source could deteriorate the quality of FD-OCT images.

Therefore, this chapter aims at developing a series of signal processing methods to recover and improve the quality of OCT images so that they clearly reflect the interior structure of a specimen. Due to the different imaging principles, two signal processing strategies were built for the data postprocessing after TD and FD-OCT measurements. Both simulated and experimental data were used to test the developed algorithm. By far, the whole OCT imaging system, including hardware setup, operation system and signal processing, has been improved. Therefore, at the end of this chapter, an evaluation of the integrated OCT system is demonstrated. Two of the most important factors, the axial measurement accuracy and SNR are characterized for both TD and FD-OCT measurement.

4.2 Signal processing in TD-OCT

In TD-OCT a single axial profile of optical reflectivity within the sample is obtained by rapidly translating the pathlength of the reference arm and synchronously recording the magnitude of the resulting interference fringes, as described in chapter 2. From Eq. 2.11 and Eq. 2.23, it can be seen that the amplitude of the interference fringe contains a Gaussian envelope and a cosine carrier with a Doppler shifting frequency, decided by the scanning velocity of reference mirror. However, in an actual OCT system there are two major obstacles for the acquisition of the Gaussian envelope that contains the structural information of the tested sample. Firstly translation stages carrying the reference mirror are commonly available with several types of actuators [3], e.g. DC motor, stepper motor, and server motor that is used in this thesis. All of these motors have some degree of nonlinearity in their motion due to jitter and/or quantization of the scan motion (e.g., a stepper motor moves in discrete steps, giving approximately constant motion.). Therefore due to the nonlinear sweeping of the reference mirror, the carrier frequency, also known as the Doppler frequency, is not perfectly constant but contains small variations during the depth scan. Since the general AM

demodulation requires a reference signal with the same frequency and phase [4], it is not applicable for an OCT signal. The second obstacle is noise. Typically there are two kinds of noise in an OCT system. One is the intrinsic noise from the OCT system [5], e.g. shot noise, thermal noise and relative intensity noise, as discussed in chapter 2. The other is speckle noise, which originates from distorted wavefronts of light returning from the sample that result in randomly appearing constructive and destructive features in the interferogram [6]. These noise contributions are mixed and can acutely degrade the OCT image quality.

In order to extract the OCT envelope and improve the image quality, a succession of signal processing methods have been developed, as shown in Fig. 4.1. Once an axial signal is obtained, bandpass filtering is performed first to reduce excess noise and to remove the DC component. Then three different solutions were evaluated and the optimum one for the customized OCT application was identified. After accumulating a series of processed axial signals, a cross-sectional image can be constructed. To further smooth the image, a 2D median filter is applied before the final image displayed. The detailed signal processing algorithms are introduced below.

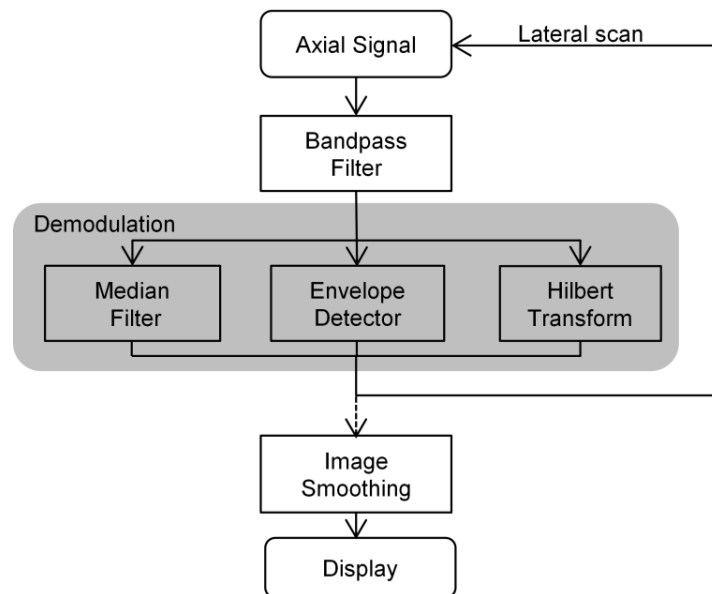


Fig. 4.1: Flowchart for signal/image processing of OCT data from the customized TD-OCT system.

4.2.1 Bandpass Filter

Although a balanced detector is used in the system to improve the signal to noise ratio, residual noise that degrades the quality of OCT images still exists. Since the OCT signal is modulated by a carrier with the Doppler frequency, a bandpass filter can be used as the first

step to remove both the noise and the DC component of the signal. For this application a fourth-order Butterworth filter was designed. Comparing with its counterparts, e.g. Chebyshev filter and the Elliptic filter, the advantages of Butterworth filter are that it has the easiest configuration and the maximally flat magnitude response [7], as shown in Fig. 4.2(b). The fourth order is selected for a fast roll off around the cutoff frequency where the attenuation of magnitude response is accelerated by the increased order. The higher order is not considered since it would largely increase the computation and thus decrease the imaging speed.

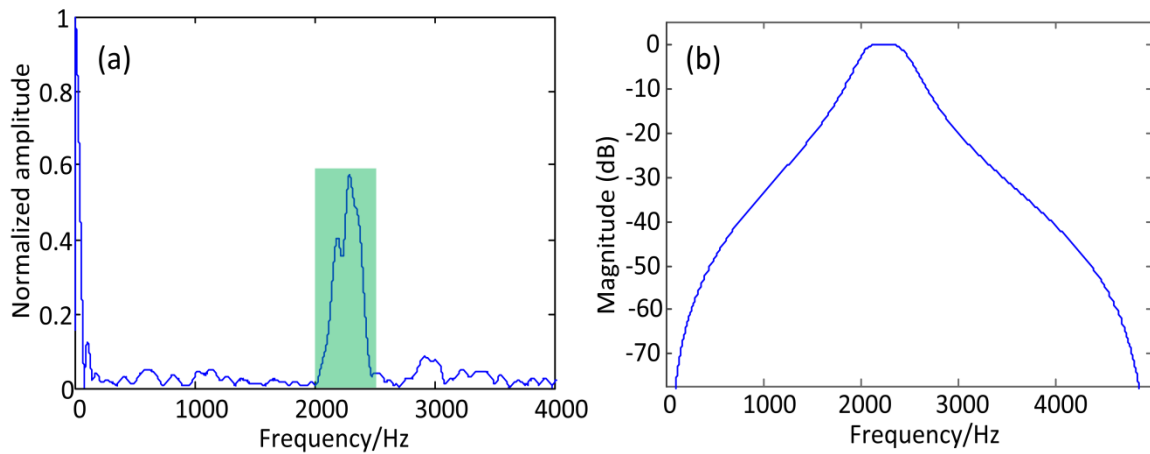


Fig. 4.2: (a) shows the frequency distribution of an A-scan signal from a reflective mirror. (b) is the magnitude response function of a 4th order Butterworth bandpass filter. The passband is set from 2000 Hz to 2500 Hz, indicated by the green box in (a)

The center frequency of the bandpass filter is the Doppler frequency f_d . The FWHM of the filter was chosen initially to match the bandwidth of the light source, $\Delta\lambda$, using the following simple relationship [3]:

$$FWHM = \frac{\Delta\lambda f_d}{\lambda} \quad (4.1)$$

In practice the filter bandwidth is chosen to be larger than the signal bandwidth [8]. A filter bandwidth that is too narrow will widen the signal in the time domain and arbitrarily limit the axial point spread function, however a bandwidth that is too large will let in more noise and reduce the minimum detectable reflectivity from a specimen. Fig. 4.2 (a) shows the frequency distribution of an A-scan signal from a reflective mirror. As indicated by the green box, the interference signal is modulated in a frequency range from 2000 Hz to 2500 Hz, which is thus

set as the passband of the filter. The filtered signal and SNR of TD-OCT measurement are shown in the following sections.

4.2.2 Demodulation

After bandpass filtering, the axial OCT signal can be simply expressed by [2]:

$$I[z] = a[z] \cos(\omega[z]z + \phi[z]) \quad (4.2)$$

where $a[z]$ is the ‘message signal’ which contains the backscattering profile of a sample with regard to depth z . $\cos(\omega[z]z + \phi[z])$ is the carrier that modulates the ‘message signal’ to high frequency. As discussed above, due to the nonlinear sweeping of the reference mirror, the frequency $\omega[z]$ of the carrier has small variations, which makes the general AM demodulation unsuitable. Therefore three demodulation methods which are largely insensitive to variations in the carrier frequency have been investigated. Both simulated and experimental data were used to evaluate the accuracy of the three methods.

The first technique, a median filter, is not a true demodulation method but is extremely rapid due to its low computational complexity. In this method, the envelope can be extracted by collecting the median of the absolute value of the modulated signal in the sliding window. However, the accuracy of this method is quite sensitive to the choice of window length. A small window length can preserve the detailed information in one axial signal but could also allow in noise that deteriorates the signal quality, while the performance of larger window length is the contrary. In the following discussion, the ideal window length is selected based on least mean square error compared with the simulated result.

The second technique, Hilbert demodulation is based on the Hilbert Transform (HT). The analytical signal $I_a[z]$ of a purely real signal $I[z]$ can be expressed as:

$$I_a[z] = I[z] + jI_h[z] \quad (4.3)$$

where $I_h[z]$ represents the ‘Hilbert’ signal which has a $-\pi/2$ phase shift compared with the original signal:

$$\begin{aligned} I_h[z] &= a[z] \cos(\omega[z]z + \phi[z] - \pi/2) \\ &= a[z] \sin(\omega[z]z + \phi[z]) \end{aligned} \quad (4.4)$$

Thus

$$I_a[z] = a[z]e^{j(\omega[z]z + \phi[z])} \quad (4.5)$$

where the axial profile $a[z]$ can be recovered by taking the absolute value of the analytic signal. The flowchart for the Hilbert demodulation is shown in Fig. 4.3.

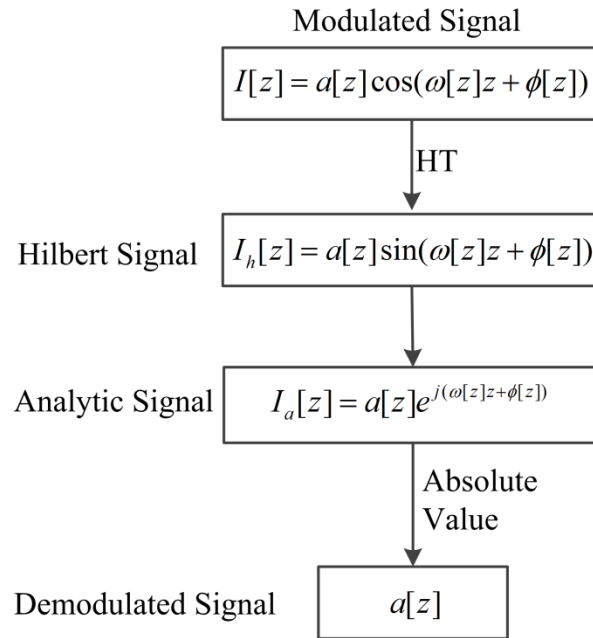


Fig. 4.3: Flowchart for the Hilbert demodulation.

The third technique is an envelope detector, which in analog circuits typically consists of a rectifier and a lowpass filter. In software, it is easy to realize by lowpass filtering the square of the modulated signal. Here the square of the signal can be calculated as:

$$\begin{aligned}
 I^2[z] &= a^2[z]\cos^2(\omega[z]z + \phi[z]) \\
 &= a^2[z]\frac{1 + \cos(2\omega[z]z + 2\phi[z])}{2} \\
 &= \frac{1}{2}a^2[z] + \frac{1}{2}a^2[z]\cos(2\omega[z]z + 2\phi[z])
 \end{aligned} \quad (4.6)$$

After squaring of the signal, it can be seen that half the energy of the modulated signal is pushed up to higher frequencies and half is shifted down towards DC. The axial profile $a[z]$ can be recovered by a lowpass filter and the square root function. The flowchart for the envelope detector is shown in Fig. 4.4.

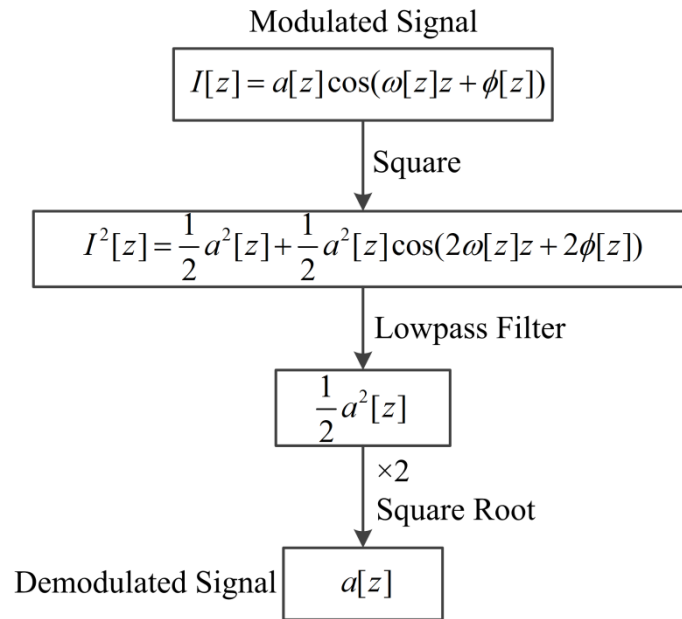


Fig. 4.4: Flowchart for the envelope detector.

To evaluate the accuracy of the three demodulation techniques, a simulated OCT signal was utilized for the testing. According to Eq. 4.2, the envelop signal $a[z]$ was specified as a Gaussian pulse with a peak located in the middle of the signal. Three separate carrier frequencies ($\omega[n]=\pi/8, \pi/6, \pi/4,$) were present consequently during the whole period to simulate the nonlinear sweeping of reference mirror. The simulated signal is shown in Fig. 4.5. In order to be closer to an actual OCT signal, $\xi[n]$, a narrowband noise with a power specified in the range 0-25% of the modulated signal, was added. It was acquired by bandpass filtering of the white noise, where the design of the filter follows the principles mentioned in section 4.2.1 (a 4th order Butterworth filter with a bandwidth from $\pi/16$ to $5\pi/16$).

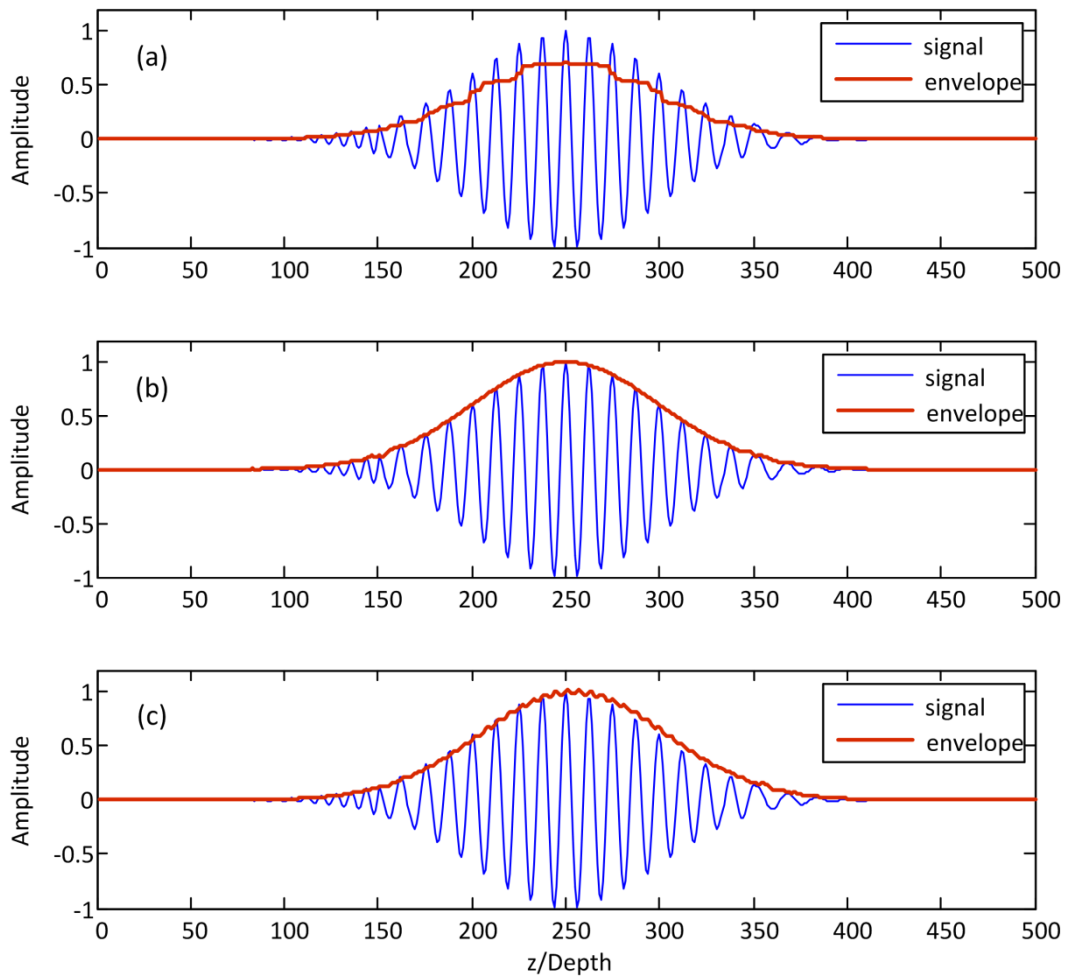


Fig. 4.5: Simulated OCT signal (without noise) and its envelope extracted by median filter (a), Hilbert demodulation (b), and envelope detector (c).

To quantitatively compare the three methods, the mean-square error (MSE) between $a[z]$ and the demodulated message $\hat{a}[z]$ was calculated as:

$$MSE = \frac{1}{N} \sum_{z=0}^{N-1} (a[z] - \hat{a}[z])^2 \quad (4.7)$$

Considering the time delay after lowpass filtering within the envelope detector, a 4th order FIR (finite impulse response) filter with Hanning window was selected, providing a constant group delay with a value of 2. To calculate the MSE, the data after the envelope detector was shifted by 2.

Fig. 4.5 shows the extracted envelop of simulated OCT signal without noise and Fig. 4.6 shows how the MSE of each algorithm varies as a function of the noise percentage added in

the simulated data. It can be seen that although the optimized window length (25 points each) is chosen, the method with a median filter gives the worst accuracy except in the high noise range, more than 20%. The results from the two other methods are quite similar at the very first phase when the noise is less than 2%. However, with an increase of the noise, the method with the envelope detector gives a better performance than that with the Hilbert transform due to the benefit of the lowpass filter which removes the high-frequency noise from the envelope.

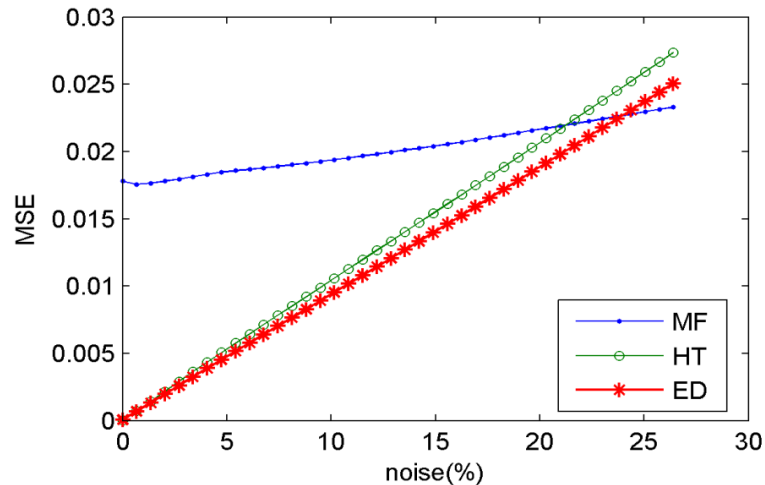


Fig. 4.6: MSE vs. noise percentage for the various demodulation algorithms applied to simulated OCT data. Abbreviations: MF, median filter. HT, Hilbert transform. ED, envelope detector.

Experimental data was also used to evaluate the three methods using a reflecting mirror as the sample. After bandpass filtering, the signals are shown in Fig. 4.7. The red lines in the each image of the figure are the envelopes extracted by the three algorithms. Similar to the results from the simulated data, the performance of the envelope detector and the Hilbert transform are better than that of median filter, and the envelope extracted by envelope detector is smoother than that extracted by the Hilbert transform. Therefore finally the envelope detector was selected as the demodulation method to match with the customized OCT setup.

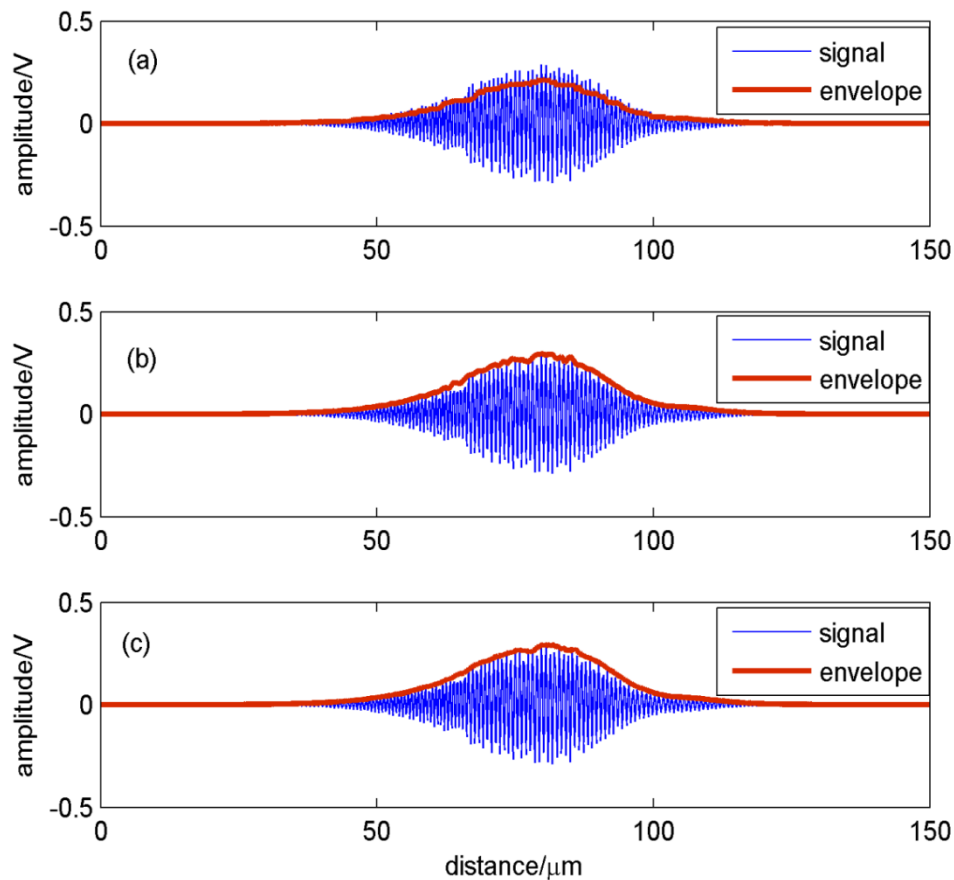


Fig. 4.7: Demodulation of experimental signal by (a) median filter, (b) Hilbert transform and (c) envelope detector. The window size for median filter is optimized to 25. The filter in the envelope detector is a 4th order Hanning window FIR filter.

4.2.3 Imaging smoothing

To suppress the speckle noise, a 2D median filter was used for smoothing the cross-sectional image (a 3D median filter was used for smoothing the volumetric image correspondingly). The value of each pixel was replaced by a median value in a local neighborhood (a $N \times N$ window where $N = 3, 5, 7$, etc.). The median filter, unlike the mean filter, while smoothing out small structural variations, does not blur the edges of regions larger than the window size used [1]. It has been applied to OCT images of different structures [9-11], showing an easy and promising way to remove the speckle noise and improve the image quality.

As an example, an 8-layer woven glass fiber composite was investigated. Fig. 4.8(a) shows the original cross-sectional image of the specimen. The fiber tows are observable as

bright ellipses. However speckles degrade the quality of the image. Fig. 4.8 (b), (c), and (d) are the enhanced images by 2D median filtering with different window sizes, 3×3 , 5×5 , and 11×11 pixels respectively. It can be seen that the image contrast is substantially improved and the structure of the sample is much more obvious. However it is also worth noting that as the window size increases, the image resolution is decreased and some detail structural information is lost. In order to reduce the speckles while at the same time preserving the structural information, an intermediate window size of 5×5 pixels was selected for this application. A detailed investigation of glass fiber composites with OCT is presented in chapter 5.

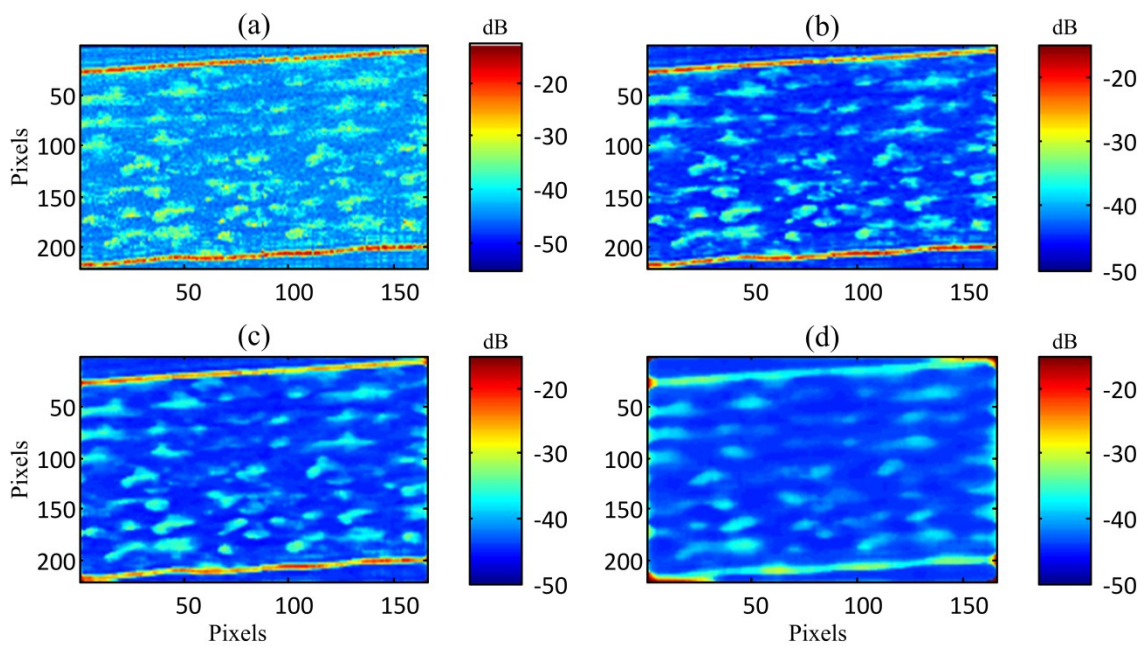


Fig. 4.8: Cross-sectional images taken from a unidirectional tape made of GFRP. (a) Original OCT image. Others are processed by 2D median filter with window size (b) 3×3 , (c) 5×5 , (d) 11×11 . The colorbars indicate the optical reflectivity in logarithm (dB).

4.3 Signal processing in FD-OCT

In FD-OCT system the interference spectrum acquired by the detector array is processed to create a depth dependent profile. As shown in Fig. 4.9, the acquired spectrum is first processed under ‘reflection mode’ of a spectrometer, in order to remove the influence from the optical source and dark noise from the CCD detectors. It is then resampled with regard to evenly spaced intervals of wavenumber, instead of wavelength. With an inverse Fourier transform, one depth profile is recovered and a cross-sectional image can be constructed by

accumulating a succession of depth profiles. The quality of the cross-sectional image can be further improved with a specially designed image smoothing technique. The detailed signal processing algorithms are introduced below.

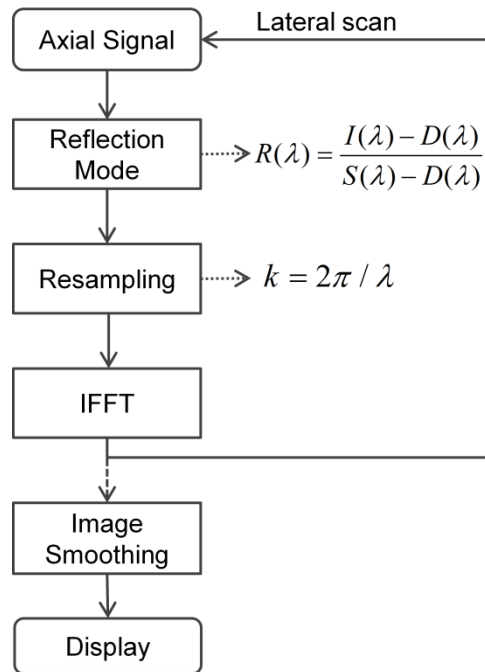


Fig. 4.9: Flowchart for signal/image processing of OCT data from the customized FD-OCT system. $I(\lambda)$ and $Re(\lambda)$ are the original and denoised spectral data. $R(\lambda)$ is the reference intensity and $D(\lambda)$ is the dark noise. λ and k are the wavelength and wavenumber respectively.

4.3.1 Reflection-mode measurement

To remove the influence from the optical source and dark noise the data is measured under the ‘reflection mode’ of the spectrometer expressed as:

$$Re(\lambda) = \frac{I(\lambda) - D(\lambda)}{R(\lambda) - D(\lambda)} \quad (4.8)$$

where $R(\lambda)$ is the reference intensity which is acquired by placing a diffuse reflectance standard (WS-1, Ocean Optics Inc, US) in front of the sample beam. $D(\lambda)$ is the dark noise thermally generated within CCD detectors, which can be obtained by shutting down the optical source. $I(\lambda)$ and $Re(\lambda)$ are the original and denoised spectral data, with examples shown in Fig. 4.10(a) and (b) respectively.

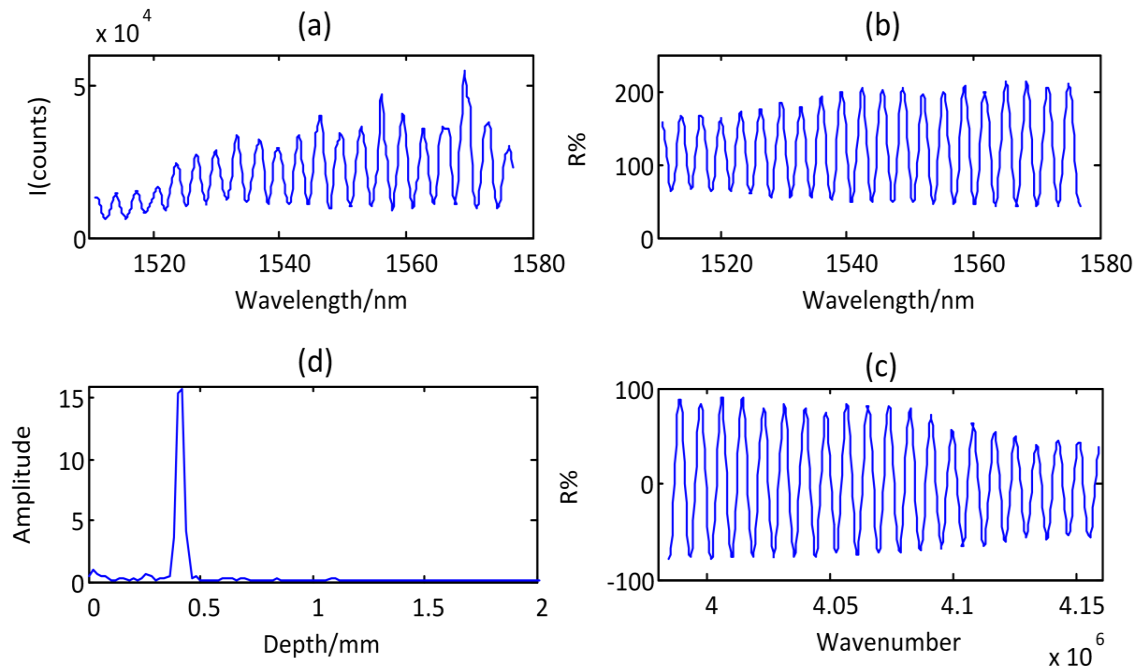


Fig. 4.10: An example of signal processing in FD-OCT by measuring a reflective mirror. (a) One dataset from the spectrometer was processed to obtain (b) ‘reflection mode’ signal based on Eq. 4.8. It was then linearly resampled in (c) with regard to wavenumber. Finally by inverse Fourier transform, (d) one depth profile was created.

4.3.2 Resampling

From Eq. 2.15, it can be seen that the depth profile can be recovered from an inverse Fourier transform of the spectral data. But one requirement is that the spectral data should be evenly spaced in frequency, specifically referring to k -space domain. Since the data is collected using evenly spaced intervals of wavelength λ rather than wavenumber k , which is inversely proportional to wavelength ($k = 2\pi / \lambda$), a resampling process is necessary before Fourier transformation. A comparison of different resampling techniques for OCT can be found in [12]. To balance processing time and image accuracy, a linear resampling was selected for the application. Fig. 4.10(c) shows the results after resampling the denoised spectral data, shown in Fig. 4.10(b).

4.3.3 Inverse Fourier transform

By inverse Fourier transform of the resampled spectral data, one depth profile was finally created, as shown in Fig. 4.10(d). However it should be noted that due to limited spectral data ($N=512$), a direct Fourier transform may result in lobe leakage in an OCT depth signal, as shown by the blue line in Fig. 4.11. Expanded main lobes and side lobes can be observed clearly, which could bring artifacts into an OCT image and prevent weaker reflectors nearby from being detected. To reduce the artifacts, a window function during Fourier transform could be applied. Here a Hanning window was selected for Fourier transform due to its ability to suppress the side lobes and simultaneously to provide a good frequency resolution that decides a narrow width of main lobe [13]. The improved results are indicated by the green lines in Fig. 4.11. It can be seen that with the window function, the main lobe is quickly delayed with regard to the axial distance and the side lobes are greatly reduced, which is required for a high-quality OCT image. The improved SNR of the FD-OCT measurement is calibrated in section 4.5.2.

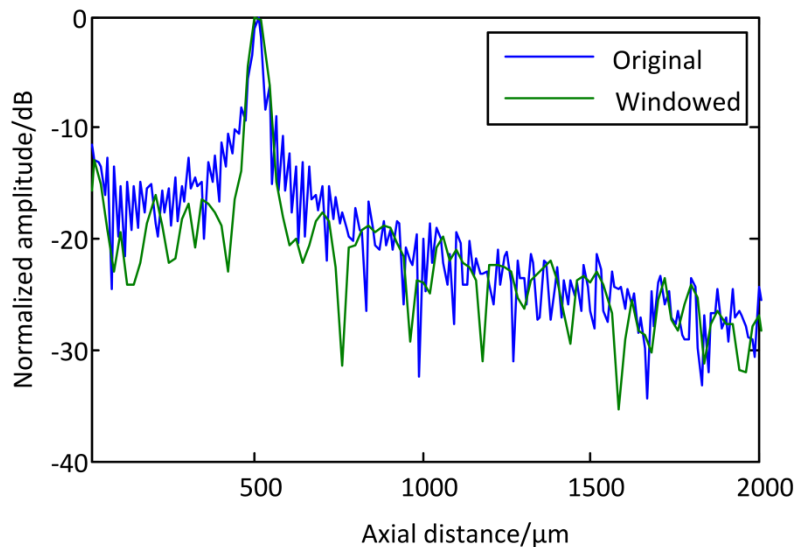


Fig. 4.11: A comparison of recovered depth profile by inverse Fourier transform with no additional processing and Hanning window function respectively.

4.3.4 Axial scan smoothing

In FD-OCT, the reflectors from different depths in a specimen are captured by the spectrometer as signal components with different frequencies. The deeper reflectors contribute to higher frequency components due to larger optical pathlength difference between reference and sample arms, thus an inverse Fourier transform recovers deeper reflectors and localizes them at longer axial distances. However there are some artifacts in the

signal which almost have constant frequency components and show up at the constant locations in a depth profile. An example is shown in Fig. 4.12. Three depth profiles are acquired from an epoxy coating at same spot but with an axial shift of the specimen each time. The two highest peaks in each color indicate the light reflections from the front and back surface of the specimen. It can be seen that the three measurements have axial shifts, which are 300, 338 μm , 413 μm respectively. However, the obvious artifacts, marked by 1-4 in Fig. 4.12, keep their same locations. The same phenomenon can be also found at other positions in depth profiles with careful observation.

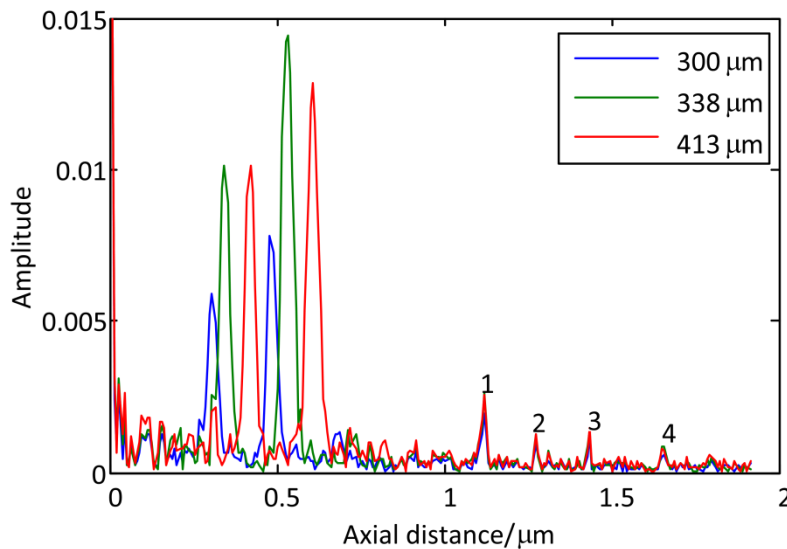


Fig. 4.12: Depth profiles of an epoxy coating with different axial shift of the specimen. The two highest peaks in each color indicate the light reflections from the front and back surface of the specimen. The markers 1-4 are examples of noise components that maintain the same locations.

Therefore, this reminds us that images from FD-OCT could be improved by employing a shifting average. As shown in Fig. 4.13(a), (b), and (c) are cross-sectional images of an epoxy coating recorded with different axial shifts of the specimen. In each image, the first two bright red lines indicate light backreflections from the front and back surfaces respectively. The third light line appears due to the multiple reflections within the sample. Apart from these components, the other features in these images are artifacts as described in Fig. 4.12. To improve the image contrast, the three images in Fig. 4.13(a), (b), and (c) were first aligned so the signals are overlapped but the artifacts are staggered. Then by taking an average of the three aligned images, the artifacts are significantly reduced, as shown in Fig. 4.13(d). The image quality could be further improved by averaging more datasets, but the time cost for additional images should be taken into account.

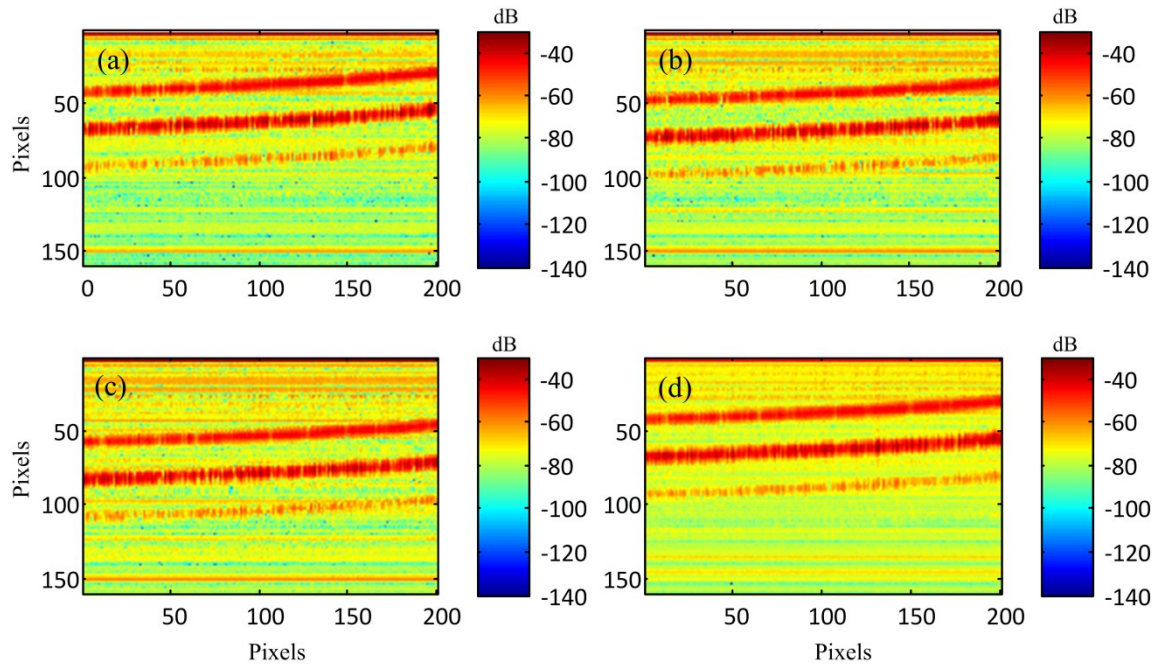


Fig. 4.13: Noise reduction by shifting average. (a)-(c) are cross-sectional images of an epoxy coating with different axial shifts of the specimen. These images are shifted back to align the signals for averaging. The averaged result is shown in (d). The colorbars indicate the optical reflectivity in logarithm (dB) scale.

4.4 Image Display

As shown in Fig. 4.8 and Fig. 4.13, the jet colormap [14], a commonly used colormap in Matlab software (Mathworks Inc., USA), can be used to display the cross-sectional images and this will be used in the rest of the thesis. The increase of the optical reflectivity from the specimen is indicated by the colors from dark (blue) to bright (red). An RGB color image has a 24-bit color level provided by the computer monitor, which is three times higher than an 8-bit gray-scale image. Therefore the use of RGB color images can improve in the differentiation of different structures. Generally an OCT signal has a large variation which could be five orders of magnitude [3], so the logarithm of the signal is normally used to expand the dynamic range of the display. The only drawback in doing this is that the relative variations in signal would be compressed, making it difficult to observe small relative changes in backreflections. Further examples of image display options are introduced in the following chapters.

4.5 System Evaluation

4.5.1 A-scan Accuracy and Linearity

To verify the axial linearity of the TD-FD-OCT configuration, a displacement test was implemented. A reflective mirror, in front of the scanning head, was driven by an actuator (NA23C60-T4, Zaber Inc, Canada) to change the optical pathlength of the sample arm. At the same time, both TD and FD-OCT A-scans were performed continuously. The displacements were calculated by locating interference peaks in the successive A-scans, as shown in Fig. 4.14. It can be seen that with the axial movement of the sample mirror, the displacement calculated by FD-OCT is much more consistent than that with TD-OCT. The measurement accuracy was also quantitatively evaluated by computing the root mean square error (RMSE) by:

$$RMSE = \sqrt{\frac{1}{n} \sum_{i=1}^n (\hat{d}_i - d_i)^2} \quad (4.9)$$

where d_i is the axial displacement of the sample mirror precisely controlled by the actuator. \hat{d}_i is the calculated displacement by the TD or FD-OCT system.

During this test, the RMSE for TD and FD-OCT are 12.4 μm and 10.4 μm , respectively. For FD-OCT the error mostly comes from the misalignment of the movement of the sample mirror and the incident light beam. For TD-OCT there is an extra error from the inconsistent sweeping of the reference mirror in the ODL, which explains the nonlinearity between the practical and measured displacement with TD-OCT, as shown in Fig. 4.14. Further example results of inconsistent A-scan in TD-OCT are shown in the Chapter 5.

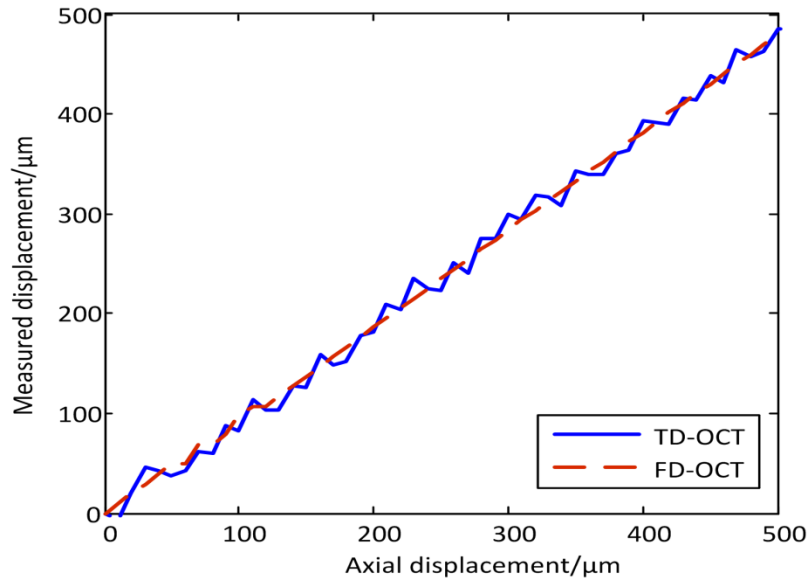


Fig. 4.14: Displacements calculated by TD and FD-OCT during the axial movement of a sample mirror.

4.5.2 Signal to Noise Ratio

SNR is another equivalently important parameter in the evaluation of an OCT system. The practical SNR of the integrated OCT system, SNR_p , was calibrated by A-scans of a reflective mirror using TD and FD-OCT respectively, and can be expressed as:

$$SNR_p = 10 \log\left(\frac{A_s}{A_n}\right) \quad (4.10)$$

where A_s and A_n are the amplitude of the signal peak and root-mean-square of the noise. The noise bins were collected from a signal bandwidth away from the signal peak in the A-scan data.

Fig. 4.15 (a) and (b) are A-scan data from a TD-OCT measurement with an output source power of 10 mW and 20 mW respectively. The calculated SNR increases from 39 dB and 50 dB, which verifies that the higher source power can give a better SNR and thus enables it to detect weak reflections from deeper into the specimen. Fig. 4.15 (c) shows one A-scan data from FD-OCT measurement with 1 ms integration time. The practical SNR is 23.8 dB, and it could be improved to 27.5 dB by increasing the integration time to 10 ms, as shown in Fig. 4.15 (d). The SNR of the FD-OCT should be able to keep increasing with longer integration time, however the increased signal power is not accessible due to the limitation of the photoelectron capacity of the CCD (saturation value).

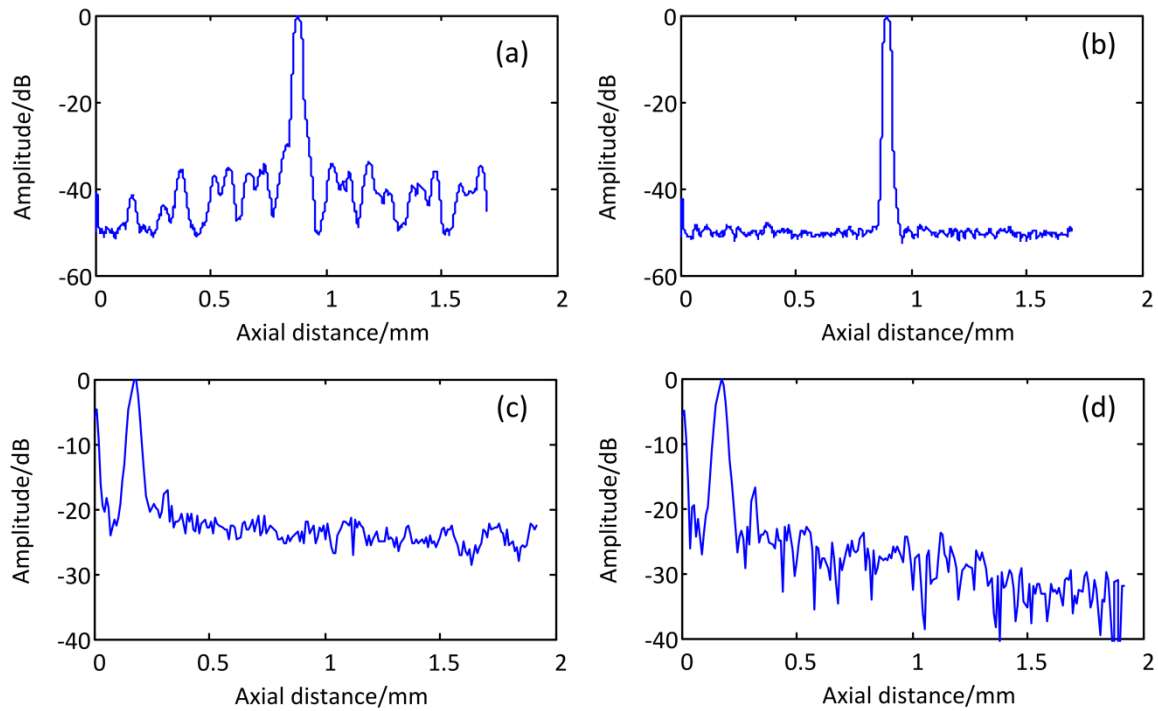


Fig. 4.15: SNR evaluation for the designed OCT system. (a) and (b) are A-scans by TD-OCT measurement of a reflective mirror, with a source power of 10 mW and 20 mW respectively. (c) and (d) are A-scans by FD-OCT measurement of a reflective mirror, with integration times of 1 ms and 10 ms respectively.

Besides, it is worth noting that there is a decay of signal peak with increasing axial distance during FD-OCT measurement, as shown in Fig. 4.16. The test was implemented by shifting the ODL to increase the sample pathlength and acquiring each A-scan simultaneously which are displayed together in Fig. 4.16. The depth-dependent signal drop is caused by optical resolution limits, finite pixel width aliasing at high spatial frequencies, and interpixel cross-talk [15]. Therefore, a compensation for this decay may be needed for measuring highly scattering and thick specimens.

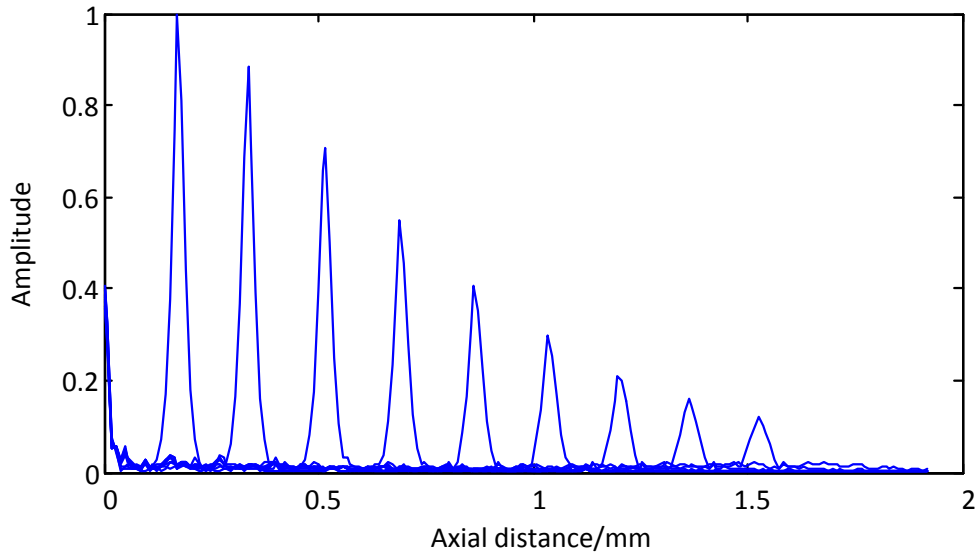


Fig. 4.16: A decay of signal peak with increasing axial distance during FD-OCT measurement of a reflective mirror. The change of axial distance is created by the ODL in the reference arm.

4.6 Discussion

The extraction of each axial envelope signal is the first important step that decides the quality of a TD-OCT image. In this chapter three demodulation techniques, median filtering, Hilbert transform and envelope detector were investigated. A Median filter has minimum computational complexity but the least accuracy since it gives underestimation on each envelope amplitude, as shown in Fig. 4.5 and Fig. 4.7. To eliminate this error during simulation, the underestimated amplitude bias can be calculated and compensated. However, it would be difficult to realize in the experimental data due to the changing signal amplitude and noise under different measurement conditions, and the variations in the signal frequency. To stay the same, bias compensation was not considered during both simulation and experiment. The Hilbert transform can give better performance but is quite sensitive to the noise. The MSE value increases dramatically with the noise growth. The ideal one is the envelope detector, which is realized by lowpass filtering of the autocorrelation of the modulated signal. At first (less than 2% noise) the accuracy of envelope detector is even a little bit lower than that of Hilbert transform due to the influence of the filter (e.g. passband ripple and stopband attenuation), as shown in Fig. 4.5(c). However it shows an advantage as the noise level increases because the lowpass filter in the envelope detector can remove the high-frequency noise and guarantee the demodulation accuracy.

Another equivalently important signal processing aspect is noise reduction. Image averaging is a widely used technique to suppress random additive noise. However it is not suitable for TD-OCT image processing because of its low efficiency caused by the repeated scanning. In the customized design, a bandpass filter and 2D median filter were used before and after the demodulation respectively. The bandpass filter acted as a signal preprocessing to remove the noise and DC component that can largely affect the result of demodulation. The 2D median filter was applied as the final step for further image enhancement. However from Fig. 4.8 the tradeoff between the resolution and speckle reduction using 2D median filter is observable with increased window size. It is noted that to date only limited research has been done in the area of image enhancement and speckle reduction in OCT imaging [9, 16-18]. Most techniques that have been developed trade resolution for reduction of speckle contrast. Further work in this area is needed.

In FD-OCT, although the measurement is under reflection mode to get rid of the influence of the light source and dark noise, the SNR is much lower than TD-OCT, as evaluated in section 4.5.2. A major factor, besides shorter acquisition time, is the Fourier transform function used in FD-OCT, which allows in the low-frequency noise and aliased signal of high spatial frequencies due to limited detector pixels. The shifting average technique introduced in section 4.3.4 could be an effect way to increase the SNR and the image contrast can be further improved with increased averaging times. However, this processing requires additional operations to apply different pathlength offsets and to acquire multiple datasets, which slows down the measurement efficiency. This disadvantage in SNR, combined with the limited depth scan range, narrows down the application range of FD-OCT. In this thesis, examples of FD-OCT applications include characterization of polymer coatings as described in chapter 7.

4.7 Conclusions

This study explored simple but highly effective methods for signal processing in the customized TD-FD-OCT system. In TD-OCT, after comparison, the envelope detector was selected as the ideal method for the demodulation of each axial signal. A bandpass filter and 2D median filter were applied before and after the demodulation, respectively, to reduce OCT system noise and speckle noise. The calculated SNR of TD-OCT reaches 50 dB, which allows the detection of weak reflectors from deep in the specimen. However one drawback is a small nonlinearity during the axial scan.

In FD-OCT, the raw data is first processed under ‘reflection mode’ of a spectrometer, in order to remove the influence from the optical source and dark noise from the CCD detectors. It is then linearly resampled with regard to evenly spaced intervals of wavenumber, instead of wavelength. With an inverse Fourier transform, one depth profile is recovered and a cross-sectional image can be constructed by accumulating a succession of depth profiles. The quality of the cross-sectional image can be further improved with shifting average, as described in section 4.3.4. Although the SNR of FD-OCT is not comparable with that of TD-OCT, the imaging speed and high axial linearity provides FD-OCT with applications in the thickness measurement and microcrack detection of thin films, as discussed in chapter 7.

References

- [1] M. E. Brezinski, [Optical coherence tomography: principles and applications], Academic Press (2006).
- [2] D. C. Adler, [Digital signal processing techniques for optical coherence tomography: OCT and OCT image enhancement], Massachusetts Institute of Technology (2004).
- [3] B. E. Bouma, and G. J. Tearney, [Handbook of optical coherence tomography], Marcel Dekker (2002).
- [4] U. Meyer-Baese, and U. Meyer-Baese, [Digital signal processing with field programmable gate arrays], Springer (2007).
- [5] P. H. Tomlins, and R. K. Wang, “Theory, developments and applications of optical coherence tomography,” *Journal of Physics D: Applied Physics*, 38(15), 2519-2535 (2005).
- [6] J. M. Schmitt, S. Xiang, and K. M. Yung, “Speckle in optical coherence tomography,” *Journal of Biomedical Optics*, 4(1), 95-105 (1999).
- [7] G. Bianchi, and R. Sorrentino, [Electronic filter simulation & design], McGraw-Hill (2007).

- [8] M. R. Hee, [Optical coherence tomography of the eye], Massachusetts Institute of Technology (1997).
- [9] J. Rogowska, and M. E. Brezinski, "Image processing techniques for noise removal, enhancement and segmentation of cartilage OCT images," *Physics in Medicine and Biology*, 47(4), 641 (2002).
- [10] G. J. Tearney, H. Yabushita, S. L. Houser *et al.*, "Quantification of macrophage content in atherosclerotic plaques by optical coherence tomography," *Circulation*, 107(1), 113-119 (2003).
- [11] V. J. Srinivasan, D. C. Adler, Y. Chen *et al.*, "Ultrahigh-speed optical coherence tomography for three-dimensional and en face imaging of the retina and optic nerve head," *Investigative Ophthalmology & Visual Science*, 49(11), 5103-5110 (2008).
- [12] C. N. Copeland, and A. K. Ellerbee, "Analysis of the effects of different resampling techniques for optical coherence tomography," *Proceeding of SPIE 8227*, 82270W-1 (2012).
- [13] A. V. Oppenheim, R. W. Schaffer, and J. R. Buck, [Discrete-time signal processing], Prentice-hall Englewood Cliffs (1989).
- [14] Colormap, <http://www.mathworks.nl/help/matlab/ref/colormap.html>.
- [15] B. Potsaid, I. Gorczynska, V. J. Srinivasan *et al.*, "Ultrahigh speed spectral/Fourier domain OCT ophthalmic imaging at 70,000 to 312,500 axial scans per second," *Optics Express*, 16(19), 15149-15169 (2008).
- [16] M. Bashkansky, and J. Reintjes, "Statistics and reduction of speckle in optical coherence tomography," *Optics Letters*, 25(8), 545-547 (2000).
- [17] M. Pircher, E. Go, R. Leitgeb *et al.*, "Speckle reduction in optical coherence tomography by frequency compounding," *Journal of Biomedical Optics*, 8(3), 565-569 (2003).

- [18] D. C. Adler, T. H. Ko, and J. G. Fujimoto, "Speckle reduction in optical coherence tomography images by use of a spatially adaptive wavelet filter," *Optics Letters*, 29(24), 2878-2880 (2004).

5

OCT for Monitoring the Delamination Growth in Glass Fiber Composite

This chapter is reproduced from:

- P. Liu, R. M. Groves, and R. Benedictus, “3D monitoring of delamination growth in a wind turbine blade composite using optical coherence tomography,” *NDT & E International*, 64, 52-58 (2014)

5.1 Introduction

Introducing a reinforcing fiber (e.g. glass fiber and carbon fiber) within a polymer matrix leads to composite materials with improved mechanical properties, e.g. high strength and stiffness to weight ratio [1]. These advantages of composites attract widespread applications, especially in aerospace and wind energy industries as introduced in chapter 1. However, this growing market also brings the challenge of quality control and health monitoring of composites due to the new forms of defects. For example, in a wind turbine system, the wind turbine blades are one of the key components as a failure of the blade eventually leads to overall breakdown of the system [2]. Currently glass fiber composites are extensively used for the production of wind turbine blades due to their high stiffness and relatively low cost [3-5]. The blades are manufactured either by resin injection techniques or by prepreg technology.

Both manufacturing processes may result in a variety of defects, such as porosity, cracks, debonding, fiber breakage and delamination. Amongst these defects delamination is probably the most frequently occurring damage and thus is of major importance [6]. It appears as a debonding of adjoining plies in laminated composites. During the operation of the wind turbine blade, a delamination crack can propagate under the influence of extra loading by wind and gravity, which may lead to final failure of the structure.

A number of non-destructive testing (NDT) techniques are employed for the inspection of delamination in wind turbine blades. Ultrasonic scanning [7] is primarily applied to study the entire blade surface and subsurface level. However a major drawback is that it is difficult to provide depth feature and high spatial resolution. Moreover, ultrasonic measurements are usually complicated by the requirement of a coupling agent between the transducer and composites. X-ray Computed Tomography (x-ray CT) [8] provides information on the internal structure of the composite material and hence makes it possible to locate inhomogeneities within the depth of the material. The high measurement cost and the difficulty for inline inspection are the main obstacles for it becoming a standard NDT tool in the field of wind turbine blades. Additionally, thermography [9] and shearography [10] have shown potential to be fast tools for delamination inspection. However both of them have limits in sensitivity to delamination defects in thick parts.

Optical Coherence Tomography (OCT) [11] could be an alternative technique due to its microscale resolution and reasonable penetration depth. Whereas a carbon fiber structure renders the composite material opaque, glass-fiber reinforced polymer poses no problem for obtaining 2-3 mm penetration depth for OCT imaging. The aim of this chapter is to use OCT imaging as a novel NDT tool to investigate delamination growth inside a wind turbine blade composite. The tested samples are glass fiber composites used for the spar webs of a wind turbine blade. A tensile test stage coupled with the customized fiber-optical OCT system was built. Then specimens with an interlaminar crack were statically loaded and stepwise scanned by the OCT system. With advanced signal processing, the volumetric images and the 3D crack profiles at successive stages during the propagation of delamination were determined.

5.2 Sample Construction

The material tested was a non-crimp glass-fiber epoxy mixture which is generally used for the spar webs in wind turbine blades. The samples were prepared by V. Sridhar, TU Delft [12]. A total of 16 layers of glass fiber were used. The fiber orientation was $+45^\circ$ and -45° , relative to the length direction of the sample, symmetrically distributed between the layers, as shown in

Fig. 5.1. To initiate the delamination a non-adhesive Kapton film of about 20 μm thickness and 40 mm length was placed in the middle layer during the lay-up process. To prepare the resin Airstone 780E epoxy and 785H hardener were used. After the vacuum infusion process, the resin completely wetted the reinforcement material. It was then placed inside an oven to cure at 75 $^{\circ}\text{C}$ for about 7 to 8 hours. Once it was cured the glass fiber composite was cut into double cantilever beam (DCB) specimens for the tests. The dimensions for each specimen are approximately 220 mm length, 25 mm width, and 4.4 mm thick. Finally each specimen was bonded to a pair of aluminum loading blocks for the tensile test.

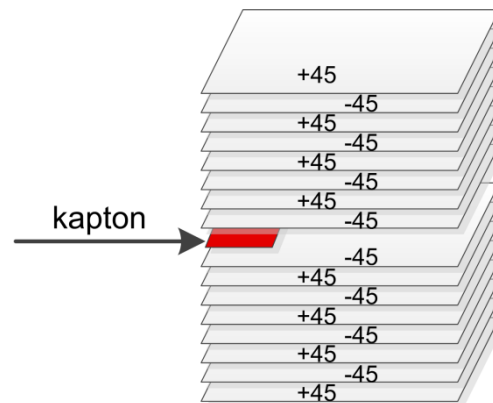


Fig. 5.1: Lay-up configuration of the composite specimen. +45 and -45 indicate the lay-up directions in degrees, relative to the length direction of the sample. Kapton was inserted between the 8th and 9th layers to initiate the delamination.

5.3 Experimental Setup

To carry out the tensile test, a mechanical stage was designed to statically load the sample to extend delamination length. As shown in Fig. 5.2, the rectangular sample was clamped horizontally by a pair of splittable hinges. Each hinge has a removable pin that acts as a joint for its plate. One hinge was attached to a loading cell for tensile measurement and the other was driven by a linear actuator (NA23C60-T4, Zaber Inc, Canada) which can provide a maximum of 950 N thrust and 60 mm travel range. The OCT probe was located in front of the specimen to examine the internal structure. The OCT probe was mounted on a 2D translation stage unit (T-LS28M, Zaber Inc, Canada) by the stainless rods, which enable the distance between the OCT probe and the specimen to be adjusted to focus the light on the specimen for optimized performance. A CCD camera (piA2400-17gm, BASLER AG, Germany) was connected at the back of the specimen to monitor the crack growth from the surface view, since the glass fiber composite is semi-transparent.

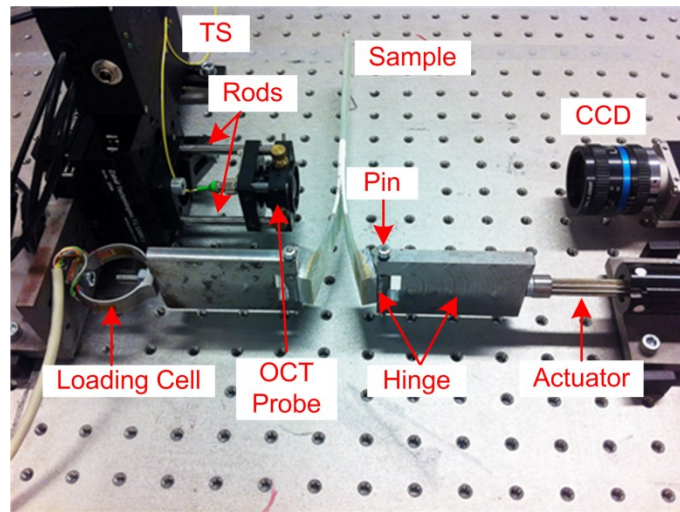


Fig. 5.2: A photograph of the loading setup. The OCT probe and CCD camera monitor the crack growth from the two opposite surfaces of the specimen. TS denotes translation stages.

5.4 Results

5.4.1 Static Test

OCT is a high-resolution imaging technique for examining the interior of scattering media. Therefore of first interest is to evaluate the capability of the customized OCT system for microstructure and defect characterization. After the specimen was clamped on the mechanical stage, a static tensile loading was applied to grow the delamination to approximately 10 mm length as measured from the side view. Then an OCT scan along the delamination crack was performed in the middle of the specimen surface. Using the signal processing algorithm developed in chapter 4, a cross-sectional OCT image was determined, as shown in Fig. 5.3(a).

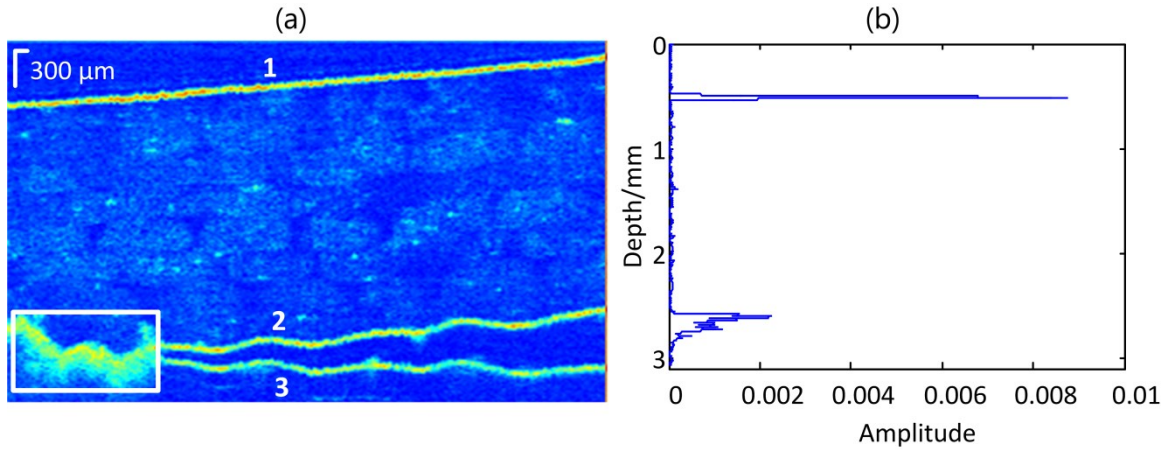


Fig. 5.3: OCT Images from a static test on a delaminated glass fiber composite. (a) A cross-sectional image along the propagation of the delamination. The first bright line indicates specimen surface location, while the second and third bright lines indicate reflections from upper and lower surfaces of the crack. The white square indicates the frontier of the delamination crack. (b) One depth scan signal across the middle of white square in (a).

The width of the image is 15 mm and is composed of 300 A-scans. The first bright line (labeled 1) in Fig. 5.3(a) indicates the location of the front surface of the specimen which was tilted by a small angle to resist strong specular reflections. Below the surface ellipses with lighter contrast are resolved, revealing the distribution of the fiber tows from each layer. The fiber tows are not as pronounced as the surface line. This is largely due to low power reflectivity ($R\%=0.002\%$) from the fiber and resin interfaces which can be simply calculated by:

$$R\% = [(n_1 - n_2) / (n_1 + n_2)]^2 \quad (5.1)$$

where n_1 and n_2 are the refractive indexes of glass fiber and resin which are very close (typically 1.56 for glass fiber and 1.545 for epoxy [13]).

Fig. 5.3(a) also shows that the optical penetration depth in this composite sample can reach 2.85 mm where the fiber tows are still detectable. This depth is deeper than the crack location and hence the OCT system is suitable for the study of this delamination crack. As demonstrated in Fig. 5.3(a), at the lower layer of the structure, around 2.2~2.7 mm, an evident feature is posed. Two bright lines (labeled 2 and 3) run along the image plane, indicating the upper and lower surfaces of the delamination crack which grows from right to left. It can be seen that the delamination does not propagate in a straight line but in a curve along the

tow/resin boundary. Moreover, an interesting phenomenon can be found at the frontier of the delamination indicated by the white square. Along the delamination growth direction, the two bright lines migrate into one with a thickness of 0.3 mm. Fig. 5.3(b) displays a corresponding A-scan signal across the middle of the square in Fig. 5.3(a). It can be seen that multiple reflections occur at the tip of the delamination. A reasonable explanation could be the multiple reflections from the interface between the material and a very small air gap. It also could be the reflections from the bridging fibers in-between the crack. These results will be analyzed in more detail in the following discussion section. Anyway the thick bright line can be used for the frontier detection during the crack propagation, which paved the way for the study of crack growth by the incremental loading test described in next section.

To present the whole delamination in detail, a volumetric image with two side views has been reconstructed as shown in Fig. 5.4(a) and (b). Fig. 5.4(a) shows the start of the delamination in the right surface and the crack propagation in the front surface. On the contrary, Fig. 5.4(b) shows the tip of delamination and the crack propagation from the other side. The arrows in both images indicate the direction of crack growth. Both images have a dimension of 12 mm in length and 6 mm in width, along and vertical to the propagation of the delamination crack respectively. The thickness of the images is approximately 2.5 mm after filtering the signal above the specimen surface, which can be located by tracking the first reflection peak from each A-scan. Similar processing was implemented to remove the signal from the air gap for a better demonstration of the crack. The strong reflectivity from the surface and the crack area are observable as the bright area, but the fiber tows are less visible since the step of lateral scan was increased to 150 μm for imaging efficiency. Nevertheless, similar to the demonstration in Fig. 5.3(a), it can be seen the propagation of the crack is not in a plane from both volumetric images. The bright area is detectable in the right surface of Fig. 5.4(b), indicating multiple reflections at the frontier of delamination.

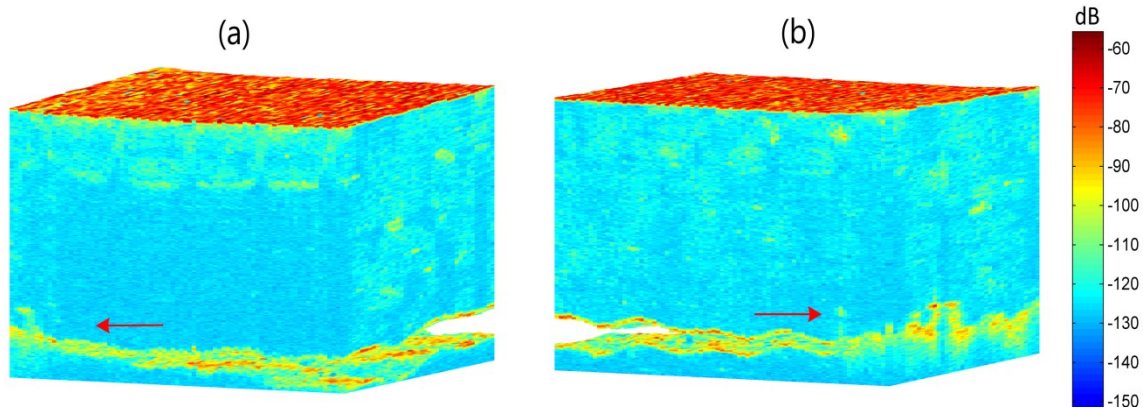


Fig. 5.4: (a) and (b) are the volumetric images of the delamination crack from two side views. The arrows in both images indicate the crack growth direction.

5.4.2 Incremental Loading Test

The static test described in section 5.4.1 proves that OCT has the ability to characterize a delamination crack. To study the behavior of delamination growth, crack profiles need to be monitored during propagation steps. Thus an incremental loading test was carried out on the same specimen but focusing on OCT measurement of the frontier of the delamination crack.

5.4.2.1 Test 1

In Fig. 5.5, (a), (b) and (c) are the volumetric images recorded during the three stages of the delamination growth. As in the cross-sectional image shown in Fig. 5.3(a), the first and second lines indicate surface and the delamination crack respectively. The delamination propagates along the y axis from right to left. The crack lengths shown in the three tomograms are approximately 6 mm, 9mm and 11 mm respectively. However, from these tomograms it is still difficult to understand how exactly the delamination grows within the composite due to the axial resolution and the artifact of multiple reflections described in the previous chapter.

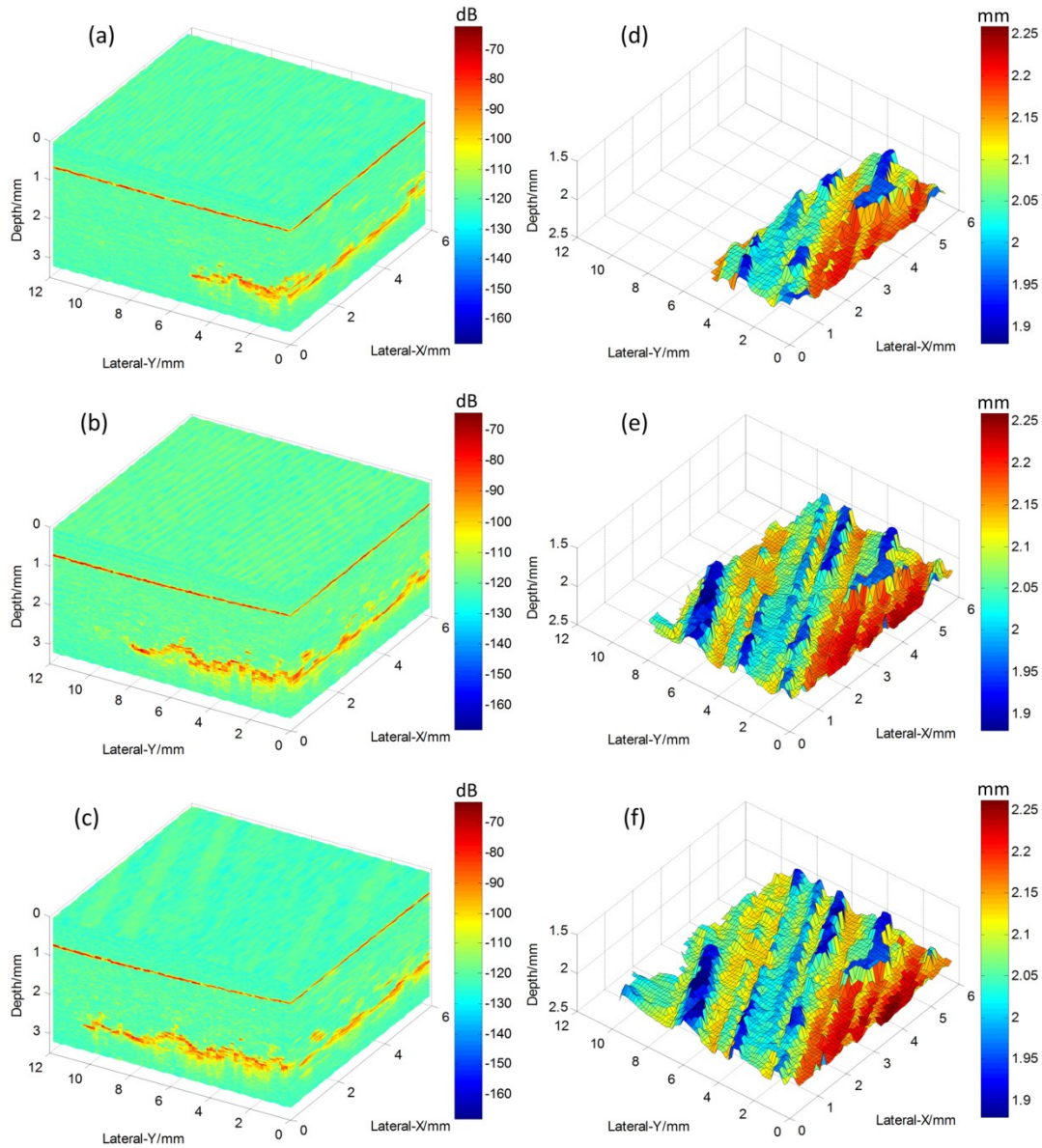


Fig. 5.5: (a), (b) and (c) are the volumetric images in three stages of crack growth. The colorbars indicate the optical reflectivity. (d), (e) and (f) are the crack surface profiles correspondingly. The colorbars indicate the surface height. The 45° color lines indicate the fiber orientation.

Therefore the three tomograms were further processed to reconstruct the crack surface profiles, as shown in Fig. 5.5(d), (e), and (f) respectively. The procedure for acquiring the crack profiles is described by the flowchart in Fig. 5.6. Firstly, each volumetric image was divided into cross-sectional images along the delamination growth direction. In the upper region of each cross-sectional image, the sample surface line can be extracted by peak detection since the first and strongest reflection comes from the surface in each A-scan signal,

as shown in Fig. 5.3(b). While in the lower region, although multiple reflections exist, the first and highest signal peak can be identified as the original reflection from the material and crack interface. Therefore the crack surface can be located in the same way by peak detection in the lower region of the cross-sectional image. Additionally, a threshold was set to find the crack tip location and thus to determine the crack length. Since there is a large reflectivity difference from crack and non-crack areas, as indicated by Fig. 5.3(b), the threshold was simply set as the median reflectivity value from these two areas. By subtracting the axial locations between the crack and sample surface, one crack thickness line was obtained. It was further smoothed by a 1D median filter with a block size of 3 pixels. Finally a 3D crack surface profile was reconstructed by accumulating a series of crack thickness lines from each cross-sectional image.

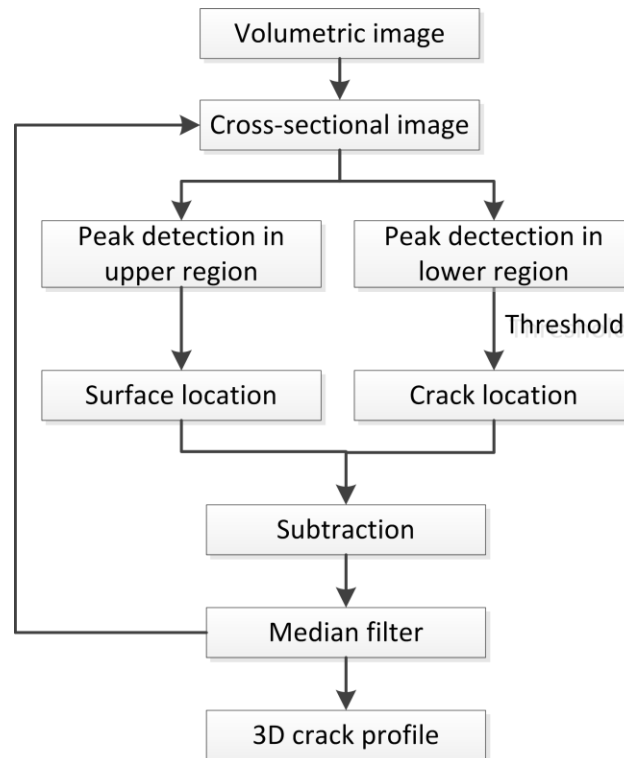


Fig. 5.6: Flowchart of the procedure for extracting the crack profiles.

From the crack surfaces shown in Fig. 5.5, delamination growth within the specimen can be easily observed. The crack lengths in the three stages are approximately 6 mm, 9 mm and 11 mm, which match with the results from corresponding tomograms as discussed above. However crack growth at different lateral locations does not proceed with the same velocity. This can be revealed by the delamination tip which is not in a vertical plane perpendicular to the crack growth orientation, as shown in Fig. 5.5(d), (e), and (f). Besides, a more interesting

observation is the 45° lines in the crack profile images. These 45° lines indicate the fiber orientation in the middle layers. It can be seen that they do not run on the same height but have a variation around 0.35 mm, indicated by the colorbar. The delamination crack grew first 2 mm at a lower layer of 2.25 mm in depth and then went to a high laminate layer with a maximum depth of 1.9 mm. However, it is difficult to estimate if the crack propagated in both the two middle layers since they have the same fiber orientation. A more accurate judgment should combine the results from more pronounced volumetric tomograms that clearly show the fiber layers. However, the cost is the dramatically increased imaging time due to the denser scanning of the sample in the same area.

5.4.2.2 Test 2

A more complete test was performed on a second specimen with the same size and material specification. Four stages of the crack growth were monitored. The force and displacement of the linear actuator are recorded in Table 5.1 and Fig. 5.7. Correspondingly four photographs were captured by the CCD camera at the back surface of the specimen, as shown in Fig. 5.8. The crack profiles at the four stages were achieved by OCT measurement in front of the specimen, as shown in Fig. 5.9. The measurement regions are of the area indicated by the white frames in Fig. 5.8. Each image size is 12 mm along the crack growth orientation and 9 mm in the perpendicular direction.

Table 5.1: Force and displacement record of the actuator during the tensile test

Stage	1	2	3	4
Force /N	36.3	51.0	54.9	51.9
Displacement/mm	0	10.5	14.9	17.4

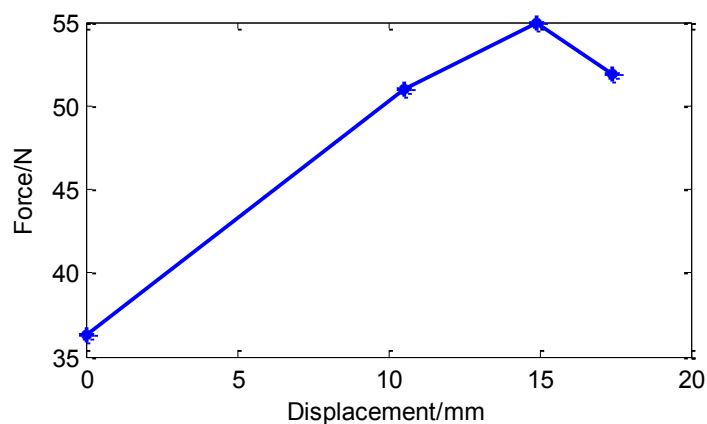


Fig. 5.7: Force and displacement relationship during the tensile test.

Due to the semi-transparency of the specimen, the crack can be detected by the area CCD camera, as shown in the lighter areas in Fig. 5.8. The $\pm 45^\circ$ lines indicate the fiber orientation while the vertical and horizontal lines are the stitches that hold each fiber tow. Besides, the crack growth (from left to right) can be seen via Fig. 5.8(a) to (d) with a roughly 3 mm increase each time. For each stage with nearly same increased crack length, it is noticeable from Table 5.1 and Fig. 5.7 that the relative displacement of the actuator is decreased while the force reaches a maximum at stage 3. The maximum force indicates the critical loading to the fracture toughness [14] of the specimen.

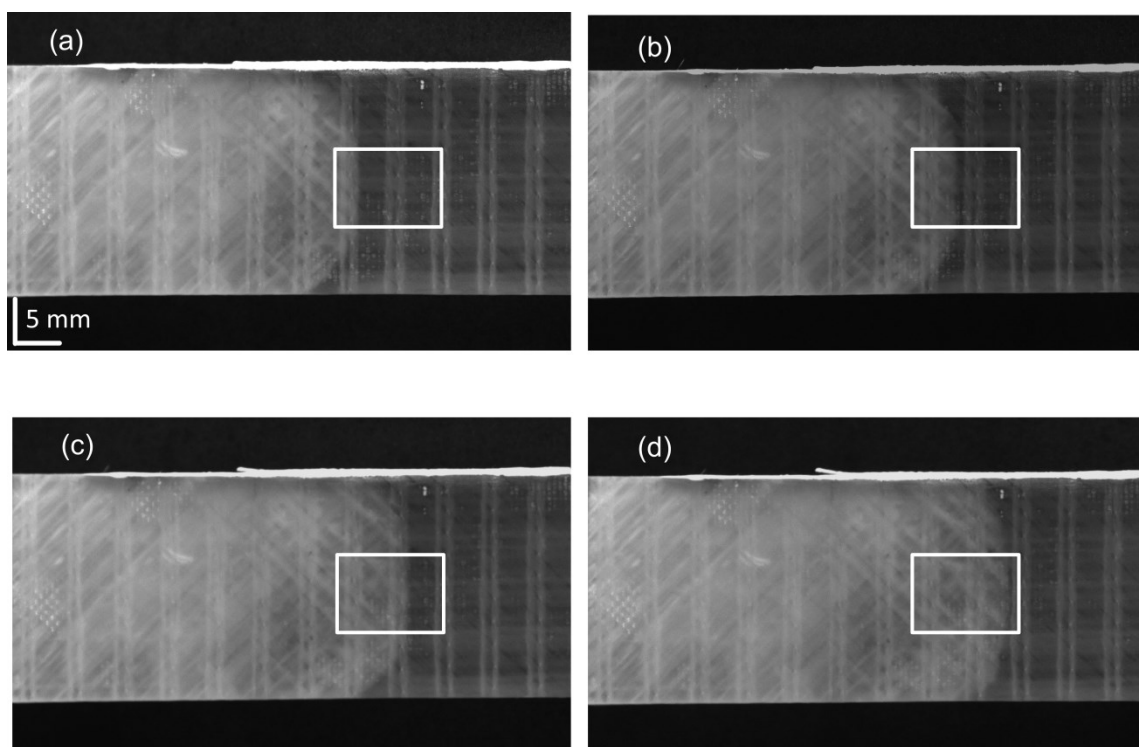


Fig. 5.8: Photographs captured by CCD Camera for four stages of crack growth indicated by the lighter areas. The white squares indicate the OCT measurement area.

Fig. 5.8 could be a good reference to monitor the crack growth from the surface view. However, to precisely track the delamination crack and reconstruct the crack profile, an OCT measurement is necessary. From Fig. 5.9 it can be seen that the crack lengths at the four stages are 2 mm, 5 mm, 8 mm, and 11 mm respectively, which is in good agreement with the results from the CCD camera shown in Fig. 5.8. Fig. 5.9 also clearly shows the tip of the crack is not in a vertical plane, which indicates the speed of the propagation at different locations are not the same. Moreover, the behavior of crack growth under the tensile loading

can be determined. Firstly within a 0 to 3 mm crack length, the delamination crack propagated in a -45° fiber layer. This can be revealed by the -45° lines with blue color. Afterwards the crack at the lower part of the specimen went to the $+45^\circ$ layer underneath the -45° one. This can be revealed by the $+45^\circ$ lines with red color. The deduction also can be proved from the depth range of the crack which is more than 0.35 mm, as indicated by the scale bar in Fig. 5.9. Considering the layer thickness of the specimen is 0.275 mm, it is probable that the crack propagated from one layer to a neighboring one.

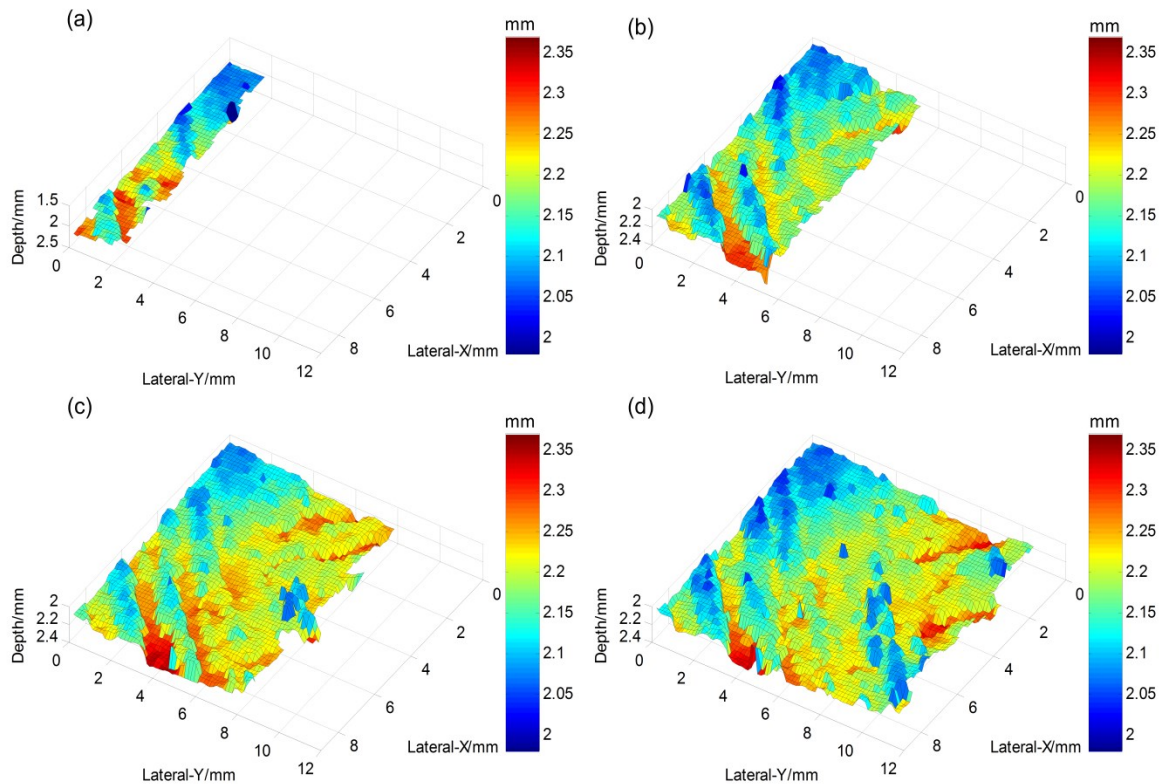


Fig. 5.9: 3D crack profiles at the frontier of delamination measured in four stages of crack growth. The $\pm 45^\circ$ color lines indicate the fiber orientation. The colorbars indicate the surface height.

5.5 Discussion

The results show how an integrated OCT system and image processing technique could be used for structural imaging and 3D monitoring of delamination propagation within a glass fiber composite. The OCT system can perform 3D volumetric images with a resolution of 11 μm (axial) by 20 μm (lateral), which is much higher than an ultrasonic scan. Due to the relatively simple setup and the fiber optic used, a portable OCT prototype may be developed in future. The optical beam travels in the fiber and emits infrared light onto the sample finally

with a power is around 1~2 mW. Therefore unlike X-ray techniques, an in-situ OCT measurement would be safe for the instrument user.

Image processing techniques were developed to show 3D crack surfaces. With incremental loading, the crack tended to migrate from the delamination plane, which is usually referred to as a crack jump [15]. Similar results [12] came out from the parallel study of structural nonlinearity at TU Delft on the same specimen type. Both show that the crack can easily propagate into another layer under monotonic loading and in a fatigue test. The crack jump is one of the most common failure modes recorded when testing multidirectional DCB specimens. Recent studies [16, 17] suggest that a crack jump is mainly decided by the bending stiffness of the crack beam and it can be prevented by optimizing the stacking sequence of the fiber layers. Another observation is the slight difference from the same imaging area in a series of crack profiles. This could be due to the influence from fiber bridging behind the crack tip, as shown in Fig. 5.10. Fiber bridging occurs when fibers are pulled from one side of the delamination plane to the other [18]. With incremental loading, the bridging fibers could shift the fracture surface and finally break. Besides, strong reflections can be detected from intensive bridging fibers closing at the crack surface. This could bring an error into the crack surface search algorithm. Therefore, during the image processing, a median filter was used as the last procedure to suppress the outlying points and minimize the error in the detected crack surface position.

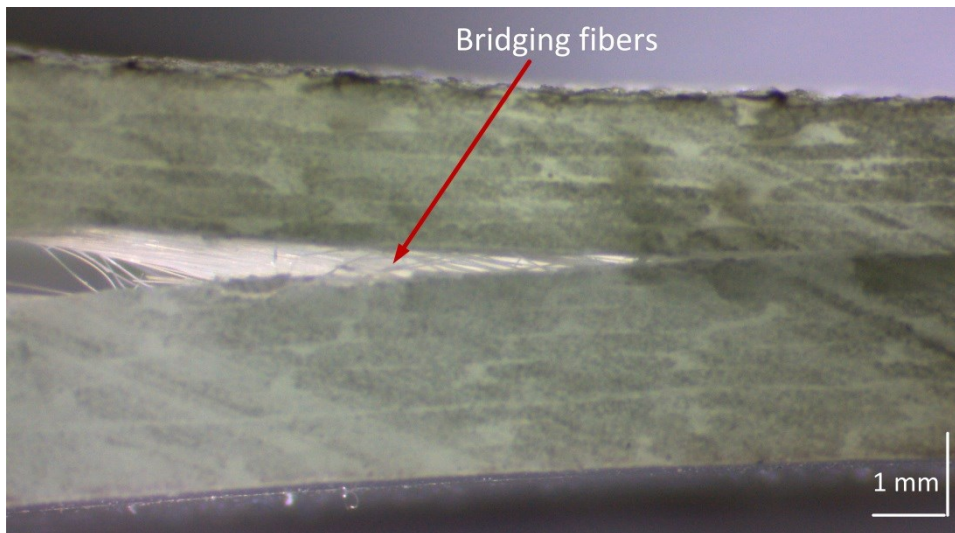


Fig. 5.10: Fiber bridging at the tip of the crack in the tested glass fiber composite.

The type of information found in this study is valuable for the study of delamination growth in glass fiber composite. So far the measurement system is based on TD-OCT that

relies on the movement of reference mirror. FD-OCT has the advantage of high speed imaging but limited depth scan range. Further improvement of the customized OCT system could either modify the current ODL to an advanced one (e.g. grating based ODL as introduced in chapter 2) for fast TD-OCT imaging, or increase the CCD pixel elements for deep FD-OCT imaging. Also the glass fiber composite used for the wind turbine blades are in practice thicker than the specimen tested in this chapter. Therefore an increase in penetration depth is necessary for detecting the delamination that occurs deep in the composite. Optical sources at longer wavelengths, which are less scattering in the composite structure, could be selected to optimize the OCT system for enhanced imaging depth [19].

5.6 Conclusions

This chapter demonstrates the potential advantages of using optical coherence tomography for the study of delamination and its propagation in a glass fiber composite used for a wind turbine blade. OCT can perform high-resolution cross-sectional and volumetric images to characterize the microstructure and the crack within a specimen. With the advanced signal processing techniques, the OCT images can be further processed to reconstruct 3D crack surface profiles, which provide substantial information for the study of crack growth in the composites.

References

- [1] R. E. Shalin, [Polymer matrix composites], Springer (1995).
- [2] I. Amenabar, A. Mendikute, A. López-Arraiza *et al.*, “Comparison and analysis of non-destructive testing techniques suitable for delamination inspection in wind turbine blades,” *Composites Part B: Engineering*, 42(5), 1298-1305 (2011).
- [3] P. Brøndsted, H. Lilholt, and A. Lystrup, “Composite materials for wind power turbine blades,” *Annual Review of Materials Research*, 35, 505-538 (2005).
- [4] D. A. Griffin, and T. D. Ashwill, “Alternative composite materials for megawatt-scale wind turbine blades: design considerations and recommended testing,” *Journal of Solar Energy Engineering*, 125(4), 515-521 (2003).

- [5] S. Habali, and I. Saleh, "Local design, testing and manufacturing of small mixed airfoil wind turbine blades of glass fiber reinforced plastics: part I: design of the blade and root," *Energy Conversion and Management*, 41(3), 249-280 (2000).
- [6] Y. Zou, L. Tong, and G. P. Steven, "Vibration-based model-dependent damage (delamination) identification and health monitoring for composite structures — a review," *Journal of Sound and Vibration*, 230(2), 357-378 (2000).
- [7] E. Jasiūnienė, R. Raišutis, R. Šliteris *et al.*, "Ultrasonic NDT of wind turbine blades using contact pulse-echo immersion testing with moving water container," *Ultrasound*, 63(3), (2008).
- [8] P. J. Schilling, B. R. Karedla, A. K. Tatiparthi *et al.*, "X-ray computed microtomography of internal damage in fiber reinforced polymer matrix composites," *Composites Science and Technology*, 65(14), 2071-2078 (2005).
- [9] C. Meola, G. M. Carlomagno, A. Squillace *et al.*, "Non-destructive evaluation of aerospace materials with lock-in thermography," *Engineering Failure Analysis*, 13(3), 380-388 (2006).
- [10] Y. Hung, "Shearography for non-destructive evaluation of composite structures," *Optics and Lasers in Engineering*, 24(2), 161-182 (1996).
- [11] A. F. Fercher, "Optical coherence tomography," *Journal of Biomedical Optics*, 1(2), 157-173 (1996).
- [12] V. Sridhar, [Combined Numerical & Experimental Methodology for the Detection of Structural Nonlinearity in Composite Wind Turbine Blades], Delft University of Technology (2012).
- [13] G. Elert, [The physics hypertextbook], (2006).
- [14] R. W. Hertzberg, [Deformation and fracture mechanics of engineering materials], Wiley (1996).

- [15] J. Schön, T. Nyman, A. Blom *et al.*, “A numerical and experimental investigation of delamination behaviour in the DCB specimen,” *Composites Science and Technology*, 60(2), 173-184 (2000).

- [16] T. Sebaey, N. Blanco, C. Lopes *et al.*, “Numerical investigation to prevent crack jumping in Double Cantilever Beam tests of multidirectional composite laminates,” *Composites Science and Technology*, 71(13), 1587-1592 (2011).

- [17] T. Sebaey, N. Blanco, J. Costa *et al.*, “Characterization of crack propagation in mode I delamination of multidirectional CFRP laminates,” *Composites Science and Technology*, 72(11), 1251-1256 (2012).

- [18] W. S. Johnson, and P. Mangalgiri, [Investigation of fiber bridging in double cantilever beam specimens], Defense Technical Information Center (1986).

- [19] U. Sharma, E. W. Chang, and S. H. Yun, “Long-wavelength optical coherence tomography at 1.7 μm for enhanced imaging depth,” *Optics Express*, 16(24), 19712-19723 (2008).

6

OCT Elastography for Measuring the Deformation within Glass Fiber Composite

This chapter is reproduced from:

- P. Liu, R. M. Groves, and R. Benedictus, “Optical coherence elastography for measuring the deformation within glass fiber composite,” *Applied Optics*, 53(22), 5070-5077 (2014).

6.1 Introduction

In the area of experimental solid mechanics, deformation and strain measurement of materials and structures subjected to various loadings (e.g. mechanical loading or thermal loading) are important tasks. Aside from the widely used pointwise strain gauge technique, various full-field non-contact optical methods, such as holography [1], speckle interferometry [2], moiré interferometry [3], and digital image correlation (DIC) [4] have been widely accepted and commonly used as powerful tools to analyze the mechanical properties of structures. However, all these techniques mentioned are developed for surface deformation measurement. Due to anisotropy or inhomogeneity of materials such as composites, the measurement of microscopic deformation within the structure is of interest for providing new information about the internal structural behavior under loading. So far, embedded fiber Bragg grating (FBG) sensors [5, 6] have been proved to be well suited for accurate, localized or distributed

strain measurement in composite structures. However a major problem is that this type of technique is not able to provide a full field view of the strain distribution within the material.

Elastography [7] is a non-invasive medical image technique that can map the elastic properties of soft tissue. The local variations of the stiffness inside the tissue can be determined from the elastography maps, known as elastograms, which provide additional clinical information for diagnosis of various diseases. In the past 20 years, elastography has been extensively developed, largely based on ultrasound [8] and magnetic resonance imaging (MRI) [9]. However, the major drawback of ultrasound scanning and MRI are their relatively low spatial resolution. So far with the advance of these techniques, high-frequency ultrasound has improved the imaging resolution to 25 μm [10] and MRI can reach 44 μm [11]. Nevertheless, these methods cannot provide high-resolucional measurement of micromechanical properties in a specimen.

Optical coherence tomography (OCT) is a contactless and non-destructive imaging modality based on the principle of low coherence interferometry. OCT has an inherent spatial resolution of 1~15 μm [12], which is much better than ultrasound and MRI techniques. Optical coherence elastography (OCE), an OCT based elastography was first introduced by Schmitt [13] in 1998. It was used to detect the depth-resolved sample deformation induced by quasi-static compression. Benefiting from the high resolution of OCT, OCE has the potential to evaluate the elasticity of the sample with a spatial resolution as well as sensitivity that are out of the reach of ultrasound and MRI.

Inspired from the OCE applications on biological tissues [14-16], this chapter aims to explore OCE to investigate glass fiber composites under mechanical loadings. The chapter is structured as follows: section 6.2 describes a customized OCT setup, loading system, and the speckle tracking algorithm for displacement measurement. In section 6.3, an evaluation of the designed OCE system is reported for rigid body translation. Then displacement maps are determined by applying the verified OCE technique on glass fiber composites under different mechanical loadings. In section 6.4, the advantages and possible further improvements for the OCE application on glass fiber composites are discussed. Finally, section 6.5 concludes the work of this chapter.

6.2 Methods

6.2.1 Experimental Setup

The specimens investigated in this chapter are glass fiber composites which are also prepared at TU Delft using the same manufacture processing as introduced in chapter 5. These specimens contain 8 layers of $0/90^\circ$ woven E-glass fiber in an epoxy resin. The dimensions of each specimen are 100 mm length, 10 mm width and 2.15 mm thickness. Therefore TD-OCT that has a larger depth scan range is selected for providing the cross-sectional images of the composite specimen. Besides the OCT setup, two loading systems, tension and three point bending were designed, as shown in Fig. 6.1(a) and (b) respectively. During the tensile test, the rectangular specimen was clamped horizontally by two pairs of steel plates and fixed by screws that penetrate both the laminate and specimen. The distance between the two fixture points was 90 mm. Then one pair of plates was attached to a fixed stage, while the other was connected to the post of a linear actuator (NA23C60-T4, Zaber Inc, Canada) that provides tensile loading. In the three point bending test, two rods with a separation distance of 50 mm were in contact with the back surface of the specimen. The same actuator provided the loading from the middle point along the length of the specimen. In both loading systems, OCT lateral scans were symmetrically distributed around the middle of the two fixture points. Pairs of tomograms acquired before and after deformation were then analysed to determine the displacement maps.

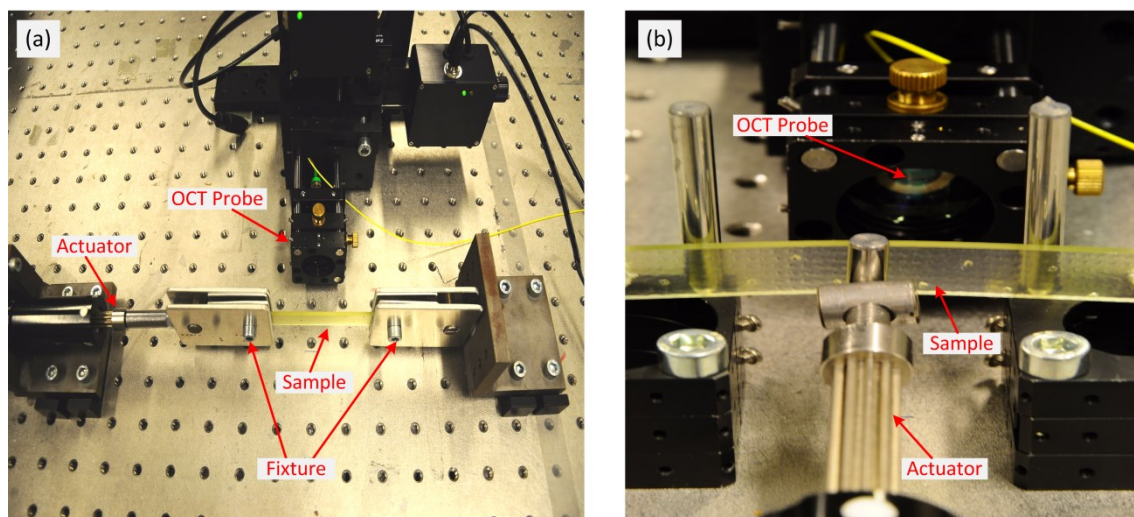


Fig. 6.1: Setup for the OCE application. (a) and (b) are the tensile and three point bending tests on the specimen respectively. The actuator provides linear loading and the OCT probe scans the specimen to acquire pairs of tomograms under the different loading conditions.

6.2.2 Image Processing Techniques

Similar to their ultrasonic counterpart, most OCE techniques rely on speckle tracking [17] to estimate the relative motion of a bulk structure under different loading forces. Phase-sensitive detection [18] is another methodology to measure the internal displacement, but it only works for the Fourier-domain OCT (FD-OCT) platform and cannot measure the lateral displacement. Typically, during speckle tracking, the pair of OCT B-scan images from pre-stressed and stressed specimens are processed with the cross correlation technique. The cross correlation coefficient, $R_{l,k}$, is defined by:

$$R_{l,k} = \frac{\sum_{i=1}^{m_1} \sum_{j=1}^{m_2} (X_{i,j} - \bar{X})(Y_{i+l,j+k} - \bar{Y})}{\sqrt{\sum_{i=1}^{m_1} \sum_{j=1}^{m_2} (X_{i,j} - \bar{X})^2 \sum_{i=1}^{m_1} \sum_{j=1}^{m_2} (Y_{i+l,j+k} - \bar{Y})^2}} \quad (6.1)$$

where \bar{X} and \bar{Y} are the mean pixel values in a predefined subset, $m_1 \times m_2$, on images X and Y respectively. i and j are the axial and lateral locations of a given pixel in image X , while l and k are the corresponding pixel displacements in image Y . Over the search region, an array of correlation coefficients is calculated and its peak value identifies the target destination.

Fig. 6.2 defines the procedure for internal displacement measurement based on the cross-correlation approach. The displacements are estimated pixel by pixel until the processing window moves over the entire pre-stressed image. However, to guarantee the accuracy of the speckle tracking, regions where the magnitude of the interference signals fall below twice the level of the electronic noise are excluded from the analysis. The average of the electronic noise is obtained from the area where the structure is not imaged (e.g. above the specimen surface). A threshold for maximum correlation coefficient is also set to eliminate the pixels which are not able to be tracked correctly. The threshold value is optimized to 0.25 in this chapter by minimizing the difference between the calculated mean displacement and the actual one deduced from the translation of the actuator. Besides, the size of the processing window, $m_1 \times m_2$, is an important parameter in the tracking procedure. An optimization of the window size is discussed in section 6.3.2. Finally a 2D median filter is applied to remove the random noise and thus improve the contrast of the displacement images.

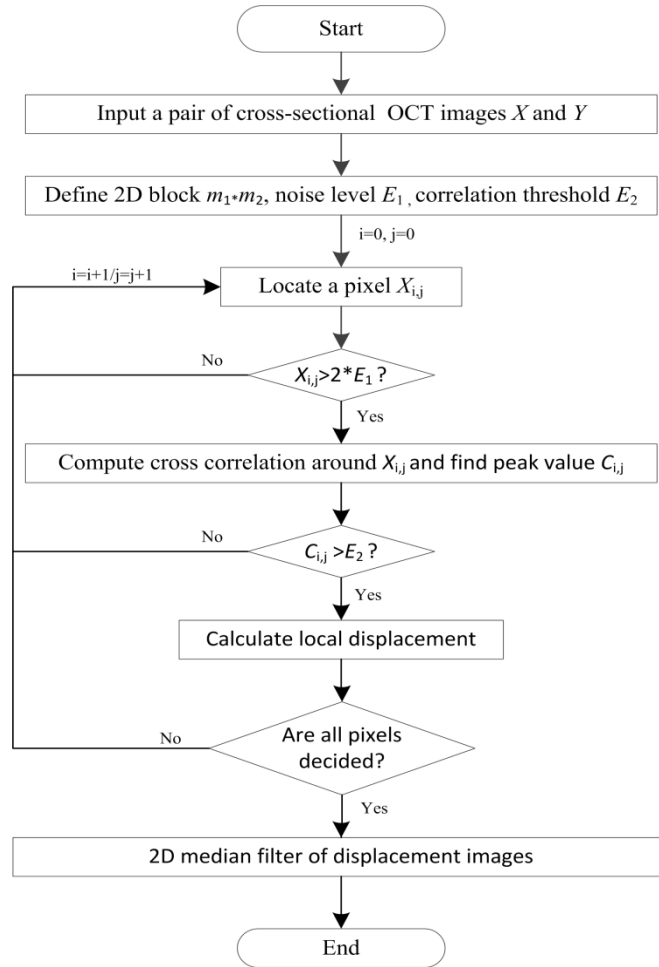


Fig. 6.2: Image processing steps for internal displacement estimation.

6.3 Results

6.3.1 Rigid Body Translation

A test of rigid body translation was introduced to evaluate the OCE system for the glass fiber composite application. A pair of cross-sectional images were obtained before and after the specimen translation and these are shown in Fig. 6.3(a) and (b). Both images are composed of 500 A-scans and image a region of 10 mm in length. Internal structures in the composite are shown by the optical reflectivity in logarithmic scale, as indicated by the colorbar. Two bright lines as well as some lighter irregularly shaped regions can be seen from both images, which indicate the surfaces and the fiber bundles within the specimen respectively. From Fig. 6.3 (a) to Fig. 6.3(b), the entire specimen was translated 6.8 μm axially and 40 μm laterally, equivalent to 2 pixels in two orthogonal directions in the images. However the difference of

the two structural images can be barely observed by eye. With the speckle tracking algorithm, the axial and lateral displacements were calculated, as shown in Fig. 6.3(c) and (d) respectively. Displacements at the edges of the structure images were neglected due to the lack of data for the processing window. The areas without any displacement in Fig. 6.3(c) and (d) indicate the locations without enough tracking speckles due to the weak reflectivity. These mostly occur at resin rich areas.

Table 6.1 summaries the OCE system accuracy by evaluating the percentage error (PE) and root mean square error (RMSE), given by:

$$PE = \frac{|\bar{d} - d|}{d} \quad (6.2)$$

$$RMSE = \sqrt{\frac{1}{MN} \sum_{i=1}^M \sum_{j=1}^N (\hat{d}_{i,j} - d)^2} \quad (6.3)$$

where $\hat{d}_{i,j}$ and \bar{d} are the calculated local and mean displacement respectively. d is the rigid body translation precisely controlled by the translation stages. $M \times N$ is the pixel size of the displacement maps. The areas with zero displacement because of untraceability were excluded from the statistical analysis. From the results summarized in Table 6.1, it is noticeable that the mean displacements in both axial and lateral direction are extremely close to the actual physical translation. The percentage errors are 2.9% axially and 1.5% laterally, and the RMSEs are 3.3 μm and 10.2 μm respectively. The higher RMSE in the lateral direction is due to the larger pixel interval (20 μm) in this direction. Actually the corresponding RMSEs in pixels are 1 axially and 0.5 laterally, which indicates a larger variation of the measured displacements in the axial direction. This can also be deduced from the inhomogeneous displacement map, as shown in Fig. 6.3 (c). The higher axial measurement error could be attributed to the nonlinear sweeping of the reference mirror in the OCT setup, as evaluated in chapter 4. The nonlinear sweeping mainly exists at the startup of the reference motor where acceleration occurs, so the A-scans could have some misalignment, which brings an extra measurement error in the axial direction.

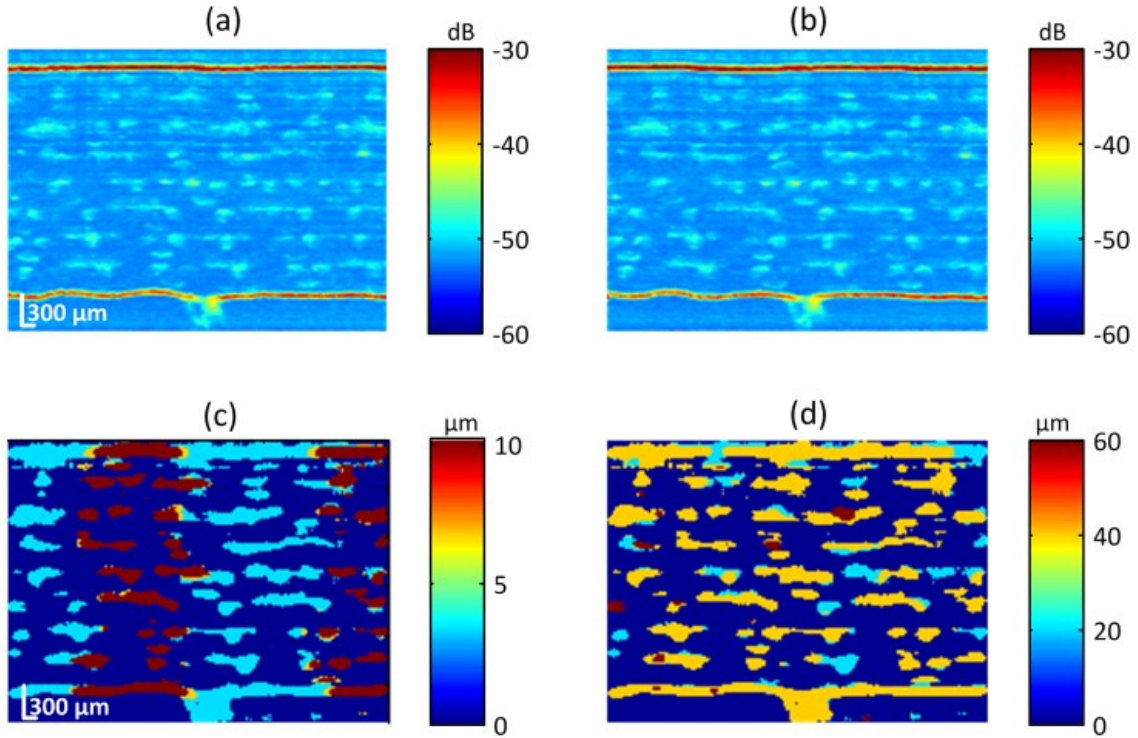


Fig. 6.3: OCE evaluation with a test of rigid body translation. (a) and (b) are a pair of structural images before and after translation respectively. (c) and (d) are the calculated displacement maps in the axial and lateral directions respectively.

Table 6.1: OCE system accuracy analysis

Orientation	$\bar{d} / \mu\text{m}$	$d / \mu\text{m}$	PE	RMSE / μm
Axial	6.6	6.8	2.9%	3.3
Lateral	39.4	40	1.5%	10.2

6.3.2 Tensile Test

In the tensile test experiment, the specimen was stretched by 500 μm between the clamps, precisely controlled by the actuator (99.94% accuracy). Two cross-sectional images were recorded before and after the loading, as shown in Fig. 6.4. Both images were obtained from 500 A-scans in the same spatial region of 10 mm length, in the middle of the specimen along the stretching direction. The pair of images were processed to calculate the lateral displacement. For this research, the influence of processing window size for cross correlation was also investigated. Fig. 6.5 shows the calculated lateral displacement with processing window sizes of 20*20, 30*30, 40*40, 60*30, 50*50 and 80*40 pixels (depth by lateral). The

unsquared window sizes were selected considering the structural images are 1000*500 pixels (depth by lateral) overall. Larger window sizes were not used in this study due to the fact that they would not be able to track the small particles in the images [19].

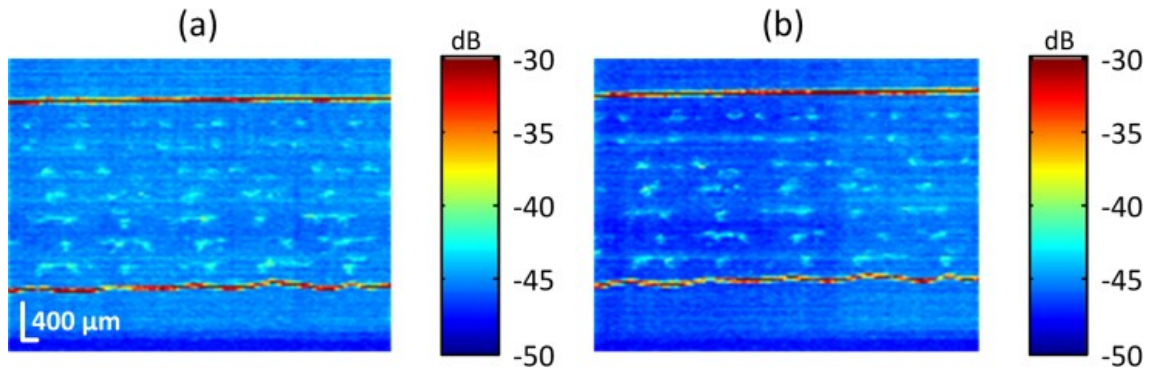


Fig. 6.4: A pair of cross-sectional images of a glass fiber composite before (a) and after (b) deformation. Both images were acquired from the same spatial location over a 10 mm length, composed by 500 A-scans.

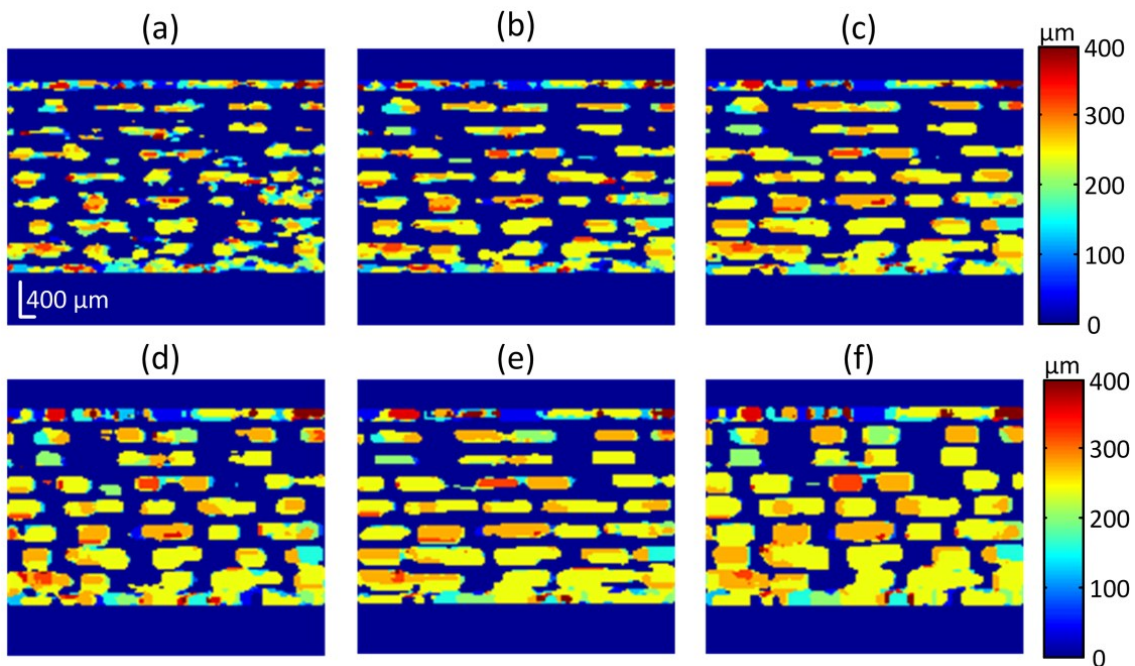


Fig. 6.5: Lateral displacement maps with a processing window size (axial by lateral) of (a) 20*20, (b) 30*30, (c) 40*40, (d) 60*30, (e) 50*50, and (f) 80*40. The areas with background color indicate where the signal-to-noise ratio is too low for the displacement calculation.

The mean displacements at different lateral locations can be calculated by averaging each axial line of the displacement maps. As an example, Fig. 6.6(a) shows the average displacement when a 50*50 window size was applied for the correlation process. It can be seen that the calculated displacements are quite close to 250 μm , which is the theoretical average displacement of the imaging area located in the middle of the sample. The theoretical displacement is calculated based on the assumption that the specimen is isotropic and that the stress is applied uniformly in the lateral direction, so the local lateral displacement d_l should be proportional to its physical distance to the fixed end of the specimen Δl , given by:

$$d_l = \frac{500}{90000} \Delta l \quad (6.4)$$

where 500 μm and 90,000 μm , are the overall loading displacement and distance respectively. To compare the measurement accuracy, the mean displacement and the RMSE were calculated for each window size, as shown in Fig. 6.6(b) and (c). It can be seen that with a processing window size of 50*50, the calculated mean displacement is closest to the theoretical value and the RMSE reaches minimum. In this way the ideal window size can be determined and the same parameters were used for the rest of this study.

However, it is also noted, from Fig. 6.6(a), that it is difficult to observe the tendency of the variation in displacement with regard to the lateral distance. A major factor is the small displacement variation (approximately 55 μm based on Eq. 6.4), relatively low lateral resolution and pixel interval (20 μm) in the OCT images. Displacements of a fraction of a pixel are impossible to be precisely tracked with current approach. More detailed considerations of the measurement accuracy are discussed in section 6.4.

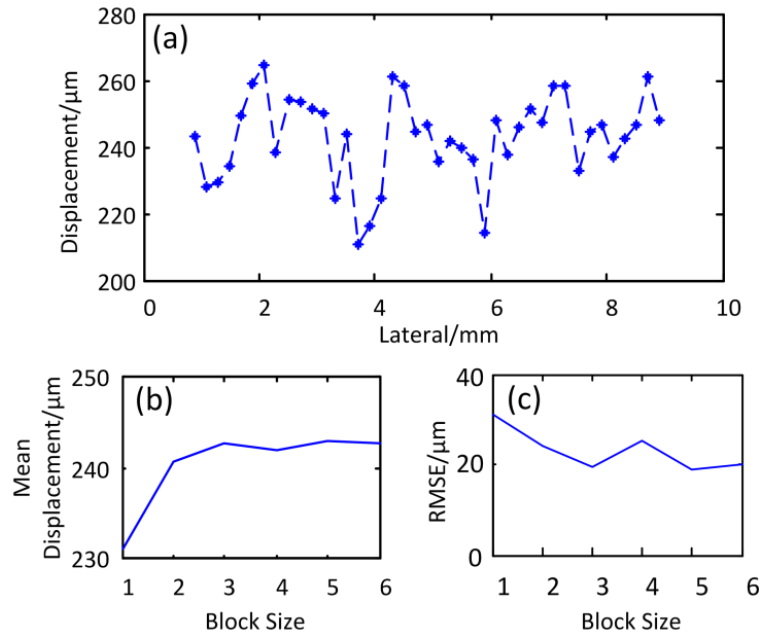


Fig. 6.6: The mean displacement with regard to the lateral location, calculated by averaging each axial line of the displacement maps. (b) and (c) are the mean and RMSE of the lateral displacement with regarding to the increased window size. Specifically, the block sizes 1 to 6 represent window sizes of 20×20 , 30×30 , 40×40 , 60×30 , 50×50 , and 80×40 respectively.

6.3.3 Three Point Bending

A three point bending experiment [20] could be an ideal example to test the axial deformation of structures with OCE. In this study, incremental transverse loadings with $250 \mu\text{m}$ steps were applied. The cross-sectional images, with 15 mm length symmetrically distributed around the loading point, were acquired for each loading condition. They were processed further to calculate axial displacement maps, as shown in Fig. 6.7. The white frames indicate the location of the loading post. Fig. 6.8 displays the average axial displacement under each loading condition. It can be seen, from Fig. 6.7 and Fig. 6.8, that both the local and the integral axial displacements increase to around $200 \sim 250 \mu\text{m}$ each time with incremental loading. The brightest areas in Fig. 6.7, corresponding to the peak regions in Fig. 6.8, indicate the locations with the largest displacement. They are in the middle of the imaging area, which is in a good agreement with the lateral location of the loading post where the largest displacement theoretically occurs. However, it is worthy of note that the distribution of the displacement is not exactly symmetrical. Also as shown in Fig. 6.7, the maximum axial displacements measured by OCE under the incremental loadings are $238 \mu\text{m}$, $476 \mu\text{m}$, and $680 \mu\text{m}$ respectively, which are slightly less than the physical translations ($250 \mu\text{m}$, $500 \mu\text{m}$, and $750 \mu\text{m}$ respectively) of the loading actuator. A most reasonable explanation is due to a

small symmetrical error from the setup and the loading. The OCE accuracy and the anisotropic structure of the composite could also contribute to the phenomenon.

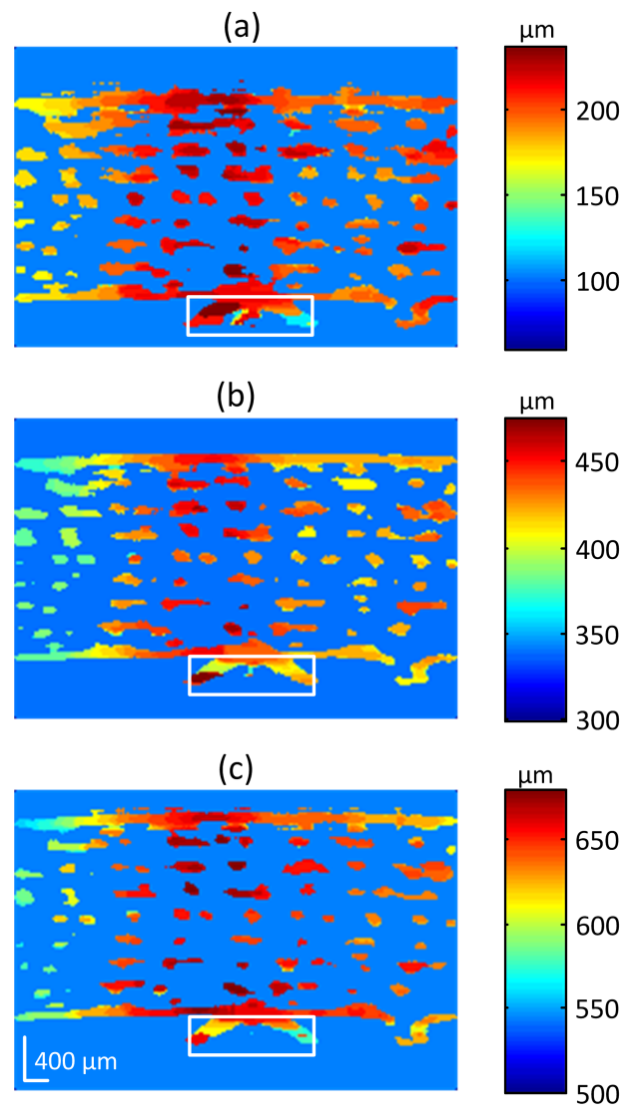


Fig. 6.7: Axial displacement maps from one cross-sectional structure of the glass fiber composite under a three point bending test. The white frames indicate the location of the loading actuator. The incremental axial translation increases by 250 μm for each successive image (a-c).

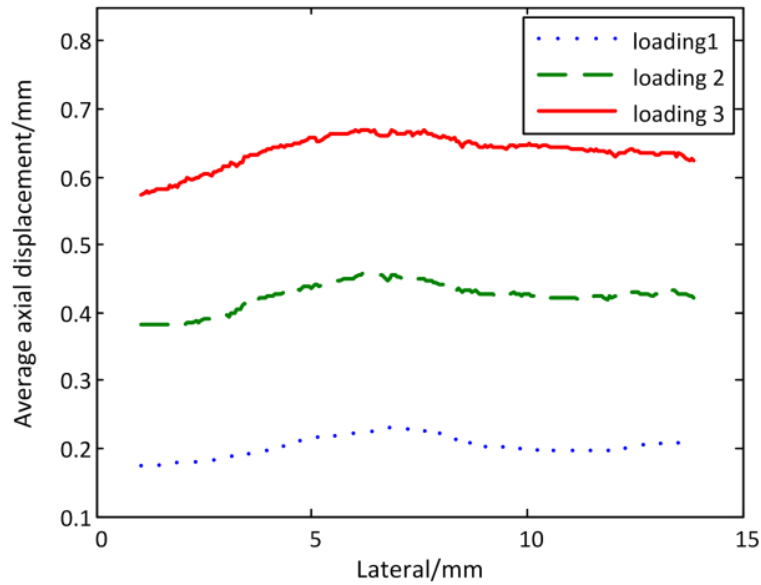


Fig. 6.8: The average axial displacements along the lateral direction obtained from the three loading conditions with 250 μm incremental axial translation of the actuator.

6.4 Discussion

OCE provides information on the internal deformation of materials based on OCT structural images. Therefore the additional contrast provided by elastography may improve the ability of OCT to characterize the structure of materials. In this study, OCE was applied to a glass fiber composite under three different translation or mechanical loadings. From the results shown in section 6.3, the first observation is that compared with OCT images, the displacement maps of OCE have better image contrast which more clearly show the internal structure of the composite specimen. The OCT images rely on the depth-resolved optical reflectivity from the specimen. Due to the extremely close refractive indexes of the glass fiber and the resin (both of which are close to 1.55 [21]), the reflections from inside the glass fiber composite have a low intensity, resulting in an interference signal just above the noise level, as shown in Fig. 6.3(a) and (b), as well as in Fig. 6.4. While in OCE, the speckle pattern, instead of the reflectivity is tracked to quantify the displacement from the OCT images. Therefore in Fig. 6.3(c) and (d), as well as Fig. 6.5, the structure of the glass fiber composite is much more clearly shown. So with this enhanced image contrast, OCT based elastography can be further applied to characterize defects, such as microcracks and delaminations within the glass fiber composite.

However, it has to be pointed out that the OCE spatial resolution is lower than OCT due to the use of the processing window and this resolution decreases with the growing size of the window, as shown in Fig. 6.5. The larger window sizes tend to average out differences in

displacements in a region, resulting in less noisy displacement maps but with reduced spatial resolution. From Fig. 6.6(b) and (c) it can be seen that statistically the measurement accuracy improved dramatically when increasing the window sizes from 20*20 to 40*40. The measured mean displacement improved from 231 μm to 243 μm , equivalently to a drop in percentage error from 7.6% to 2.8%. The RMSE decreases from 31 μm to 20 μm correspondingly. Afterwards, there is no significant improvement from further increasing the window size. Finally a size of 50*50 was found to be a good compromise between measurement accuracy and spatial resolution.

Besides processing window size, the measurement accuracy could also be affected by the OCT image noise, out-of-plane displacement, and speckle decorrelation [22]. For the OCT image noise, a threshold was set to filter out the areas with low signal-to-noise ratio (SNR), which indicate resin-rich areas and areas outside the specimen. These areas in the OCT images are excluded from the displacement calculation. The out-of-plane displacement is not studied in this chapter, but it is possible to determine it using a similar speckle tracking technique or digital volume correlation (DVC) on pairs of volumetric OCT images [23]. The most troublesome factor is speckle decorrelation. The cross-correlation approach of OCE has a limited ability to track the deformations which are either too small or too large. For example, when the speckle motion is only a fraction of a pixel, the cross-correlation approach cannot track the shift robustly even with various smoothing techniques [24]. At the other extreme, the relative positions of the scatterers that form the speckle patterns change gradually when the deformation increases, which results in gradual speckle decorrelation. However, unlike speckles in soft tissues that are easily decorrelated by a small deformation on the order of the OCT spatial resolution [25], speckle patterns from composites can endure much larger displacements as presented in this chapter. An explanation could be that the areas with fiber reinforcement are stiffer than the polymer matrix areas. So the areas with fiber bundles, where speckles occur, behave more like rigid bodies that translate without deformation. That is why speckles can still be tracked after a displacement of hundreds of micrometers. Nevertheless, speckle decorrelation is an inevitable phenomenon during the loading test of a specimen. An improvement to the tracking accuracy and measurement range [26, 27] could be a direction for future work.

As the results in Fig. 6.7 illustrate, a sequence of displacement maps from a glass fiber composite under gradually increasing loading can provide sufficient information to observe the structural variations or even to deduce the regional stiffness by a knowledgeable observer without further processing. However, to estimate a sample's depth-resolved elastic properties

quantitatively, the local strain needs to be calculated based on the displacement maps. Currently, the method of least squares (LS) has proved to be a robust approach for the strain estimate in OCE [28]. A set of displacement data in a neighboring region is used to calculate local strain from least-squares fitting. However, unlike biological tissues that can provide consecutive scatters in a cross-sectional area, optical reflections within glass fiber composite only occur at the fiber-resin interfaces, resulting in discrete speckle patterns separated by the resin-rich areas in OCT images. Consequently, displacement maps, as shown in section 6.3, can only display the local results discretely, which makes it difficult to estimate the strain distribution. A possible solution is to mix small inclusions with epoxy to track the displacements from the resin as well, but care must be taken to minimize the influence of the inclusions on the composite elastic properties.

6.5 Conclusions

This study explored the use of optical coherence elastography for the deformation measurement of glass fiber composites, for the first time to the best of our knowledge. The developed OCE system can track internal displacements in the range from a few micrometers to hundreds of micrometers. The cross-sectional displacement maps clearly show the structural features and structural variations, which could provide supplementary understanding of the mechanical properties of glass fiber composites.

References

- [1] R. Rowlands, and I. Daniel, "Application of holography to anisotropic composite plates," *Experimental Mechanics*, 12(2), 75-82 (1972).
- [2] J. Butters, and J. Leendertz, "Speckle pattern and holographic techniques in engineering metrology," *Optics & Laser Technology*, 3(1), 26-30 (1971).
- [3] D. Post, B. Han, and P. Ifju, [*Moiré interferometry*], Springer (1994).
- [4] T. Chu, W. Ranson, and M. Sutton, "Applications of digital-image-correlation techniques to experimental mechanics," *Experimental Mechanics*, 25(3), 232-244 (1985).

- [5] Y. Okabe, S. Yashiro, T. Kosaka *et al.*, "Detection of transverse cracks in CFRP composites using embedded fiber Bragg grating sensors," *Smart Materials and Structures*, 9(6), 832 (2000).
- [6] J. Botsis, L. Humbert, F. Colpo *et al.*, "Embedded fiber Bragg grating sensor for internal strain measurements in polymeric materials," *Optics and Lasers in Engineering*, 43(3), 491-510 (2005).
- [7] J. Ophir, I. Cespedes, H. Ponnekanti *et al.*, "Elastography: a quantitative method for imaging the elasticity of biological tissues," *Ultrasonic Imaging*, 13(2), 111-134 (1991).
- [8] C. L. De Korte, G. Pasterkamp, A. F. Van Der Steen *et al.*, "Characterization of plaque components with intravascular ultrasound elastography in human femoral and coronary arteries in vitro," *Circulation*, 102(6), 617-623 (2000).
- [9] A. Manduca, T. E. Oliphant, M. Dresner *et al.*, "Magnetic resonance elastography: non-invasive mapping of tissue elasticity," *Medical Image Analysis*, 5(4), 237-254 (2001).
- [10] Q. Zhou, S. Lau, D. Wu *et al.*, "Piezoelectric films for high frequency ultrasonic transducers in biomedical applications," *Progress in Materials Science*, 56(2), 139-174 (2011).
- [11] L. Massey, M. Miranda, L. Zrinzo *et al.*, "High resolution MR anatomy of the subthalamic nucleus: Imaging at 9.4 T with histological validation," *Neuroimage*, 59(3), 2035-2044 (2012).
- [12] B. E. Bouma, and G. J. Tearney, [Handbook of optical coherence tomography], Marcel Dekker (2002).
- [13] J. M. Schmitt, "OCT elastography: imaging microscopic deformation and strain of tissue," *Optics Express*, 3(6), 199-211 (1998).
- [14] J. Rogowska, N. Patel, S. Plummer *et al.*, "Quantitative optical coherence tomographic elastography: method for assessing arterial mechanical properties," *British Journal of Radiology*, 79(945), 707-711 (2006).

- [15] H.-J. Ko, W. Tan, R. Stack *et al.*, “Optical coherence elastography of engineered and developing tissue,” *Tissue Engineering*, 12(1), 63-73 (2006).
- [16] B. F. Kennedy, K. M. Kennedy, and D. D. Sampson, “A Review of Optical Coherence Elastography: Fundamentals, Techniques and Prospects,” *IEEE Journal of Selected Topics in Quantum Electronics*, 20(2), 1-17 (2014).
- [17] D. D. Duncan, and S. J. Kirkpatrick, “Processing algorithms for tracking speckle shifts in optical elastography of biological tissues,” *Journal of Biomedical Optics*, 6(4), 418-426 (2001).
- [18] R. K. Wang, S. Kirkpatrick, and M. Hinds, “Phase-sensitive optical coherence elastography for mapping tissue microstrains in real time,” *Applied Physics Letters*, 90(16), 164105 (2007).
- [19] J. Rogowska, N. Patel, J. Fujimoto *et al.*, “Optical coherence tomographic elastography technique for measuring deformation and strain of atherosclerotic tissues,” *Heart*, 90(5), 556-562 (2004).
- [20] A. W. Christiansen, J. Lilley, and J. B. Shortall, “A three point bend test for fibre-reinforced composites,” *Fibre Science and Technology*, 7(1), 1-13 (1974).
- [21] G. Elert, [The physics hypertextbook], (2006).
- [22] C. Sun, B. Standish, B. Vuong *et al.*, “Digital image correlation-based optical coherence elastography,” *Journal of Biomedical Optics*, 18(12), 121515-121515 (2013).
- [23] J. Fu, M. Haghighi-Abayneh, F. Pierron *et al.*, [Assessment of corneal deformation using optical coherence tomography and digital volume correlation], Springer (2013).
- [24] K. Parker, M. Doyley, and D. Rubens, “Imaging the elastic properties of tissue: the 20 year perspective,” *Physics in Medicine and Biology*, 56(1), R1 (2011).
- [25] C. Sun, B. Standish, and V. X. Yang, “Optical coherence elastography: current status and future applications,” *Journal of Biomedical Optics*, 16(4), 043001 (2011).

- [26] S. J. Kirkpatrick, R. K. Wang, and D. D. Duncan, "OCT-based elastography for large and small deformations," *Optics Express*, 14(24), 11585-11597 (2006).

- [27] V. Y. Zaitsev, L. A. Matveev, G. V. Gelikonov *et al.*, "A correlation-stability approach to elasticity mapping in optical coherence tomography," *Laser Physics Letters*, 10(6), 065601 (2013).

- [28] B. F. Kennedy, S. H. Koh, R. A. McLaughlin *et al.*, "Strain estimation in phase-sensitive optical coherence elastography," *Biomedical Optics Express*, 3(8), 1865 (2012).

7

Further Non-destructive Testing Applications

This chapter is partly reproduced from:

- P. Liu, R. M. Groves, and R. Benedictus, “Optical Coherence Tomography for the Study of Polymer and Polymer Matrix Composites,” *Strain*, 50(5), 436-443(2014).

7.1 Introduction

Optical coherence tomography (OCT) is a non-destructive, contactless and high-resolution imaging method, which allows the acquisition of one-, two- or three-dimensional depth-resolved image in situ and in real time. Currently OCT is not only an already well-established diagnostics technique for biomedicine applications, it has also received increasing attention in non-destructive testing (NDT) field. For example, in industry, OCT has shown potential to improve productivity by inline quality control in the monitoring of the manufacture of multiple-layered plastic foils [1]. The detected parameters include thickness, homogeneity, and possible inclusion of air or impurities. In the field of artwork conservation, OCT also starts to play an important role for scientific research. The structural imaging of artworks, e.g. paintings and porcelain, provides substantial information for historical research and restoration treatment [2]. Nevertheless, as stated in chapter 1, the development of OCT in the NDT field is much lagging behind of its biomedical counterparts. Both the OCT techniques and its applications in the NDT field need to be further explored.

In chapters 5 and 6, glass fiber composites have been studied with the designed OCT system. This chapter aims to demonstrate some further NDT applications. It is organized as follow: section 7.2 focuses on the characterization of polymer coatings, including microcracks and thickness measurement. Section 7.3 studies both front and back faces of a wooden panel painting. This includes structural imaging, defects examination in paint layers and 3D surface reconstruction of a wooden knot. Finally, section 7.4 summarizes the chapter.

7.2 Defects and Thickness Measurement of Polymer Coatings

7.2.1 Introduction

Polymer coatings have been widely used in engineering fields due to their advantages including light weight, good processibility and chemical stability [3]. For example, epoxy coatings are extensively employed for corrosion protection of steel pipes and metal containers used in the gas and oil industry, water pipelines, beverage cans, etc. In aerospace engineering, polymer coatings are used to protect aircraft from corrosion, impact, and lightning [4, 5]. Traditional coatings for the aerospace industry were developed for aluminium substrates. Since composites substrates play an increasingly important role in new airplane designs, new challenges arise for the coating industry. One of the main challenges concerning coatings on composites is the appearance of cracks in the coating which occur at much lower strain levels than on aluminum substrates [6]. Those cracks occur due to the ductile-brittle transition [7] of the coatings and the substrates. Another initiator of the crack forming is known to be residual stresses due to differences in expansion coefficients. Therefore, this section aims to demonstrate the quality assessment of polymer coatings using OCT, including the detection microcracks and the measurement of the thicknesses of polymer coatings.

7.2.2 Detection and measurement of microcracks

The first sample investigated was an epoxy coating with a painted carbon fiber composite as the substrate. As shown in Fig. 7.1, the dimension of the specimen is 100 mm long and 10 mm wide. The light stripers indicate the microcracks within the coating. These cracks have different width and some of them are hardly visible by naked eye. The image at the bottom of Fig. 7.1 shows an enlarged view from the area indicated by the red square. The arrow which crosses two microcracks indicates the OCT scan line.

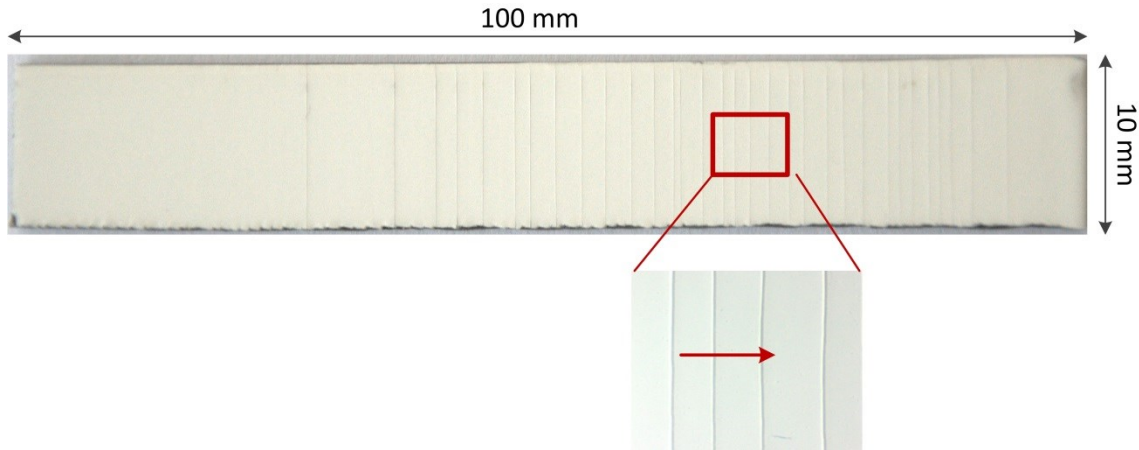


Fig. 7.1: (a) an epoxy coating on a carbon fiber composite substrate and (b) an enlarged image from the area indicated by the red square. The dark stripes indicate microcracks in the polymer coating. The arrow indicates the OCT scanning area.

During this test, both TD-OCT and FD-OCT measurements were implemented. As shown in Fig. 7.2, the cross-sectional structural images were obtained from the same area which has a size of 1.1 mm in depth by 3 mm in width, comprising to 150 A-scans. The sample was tilted by a small angle during the measurement to avoid the strong surface specular reflection, partially indicated by the upper bright lines in the both images. The lower bright area in each image indicates reflectors from the surface and in the subsurface of the substrate. By a comparison analysis of the two images from different measurements, two cracks, indicated by arrows in the Fig. 7.2 can be identified based on the discontinuity of the surface reflection lines. The first one is more obvious due to the larger size of crack, which is approximately 40 μm in width. The second crack is more ambiguous since weak reflections from the surface of the coating still can be detected. This is because the lateral resolution, decided by the beam size in the customized OCT system is 20 μm , and this limits the ability to detect smaller cracks.

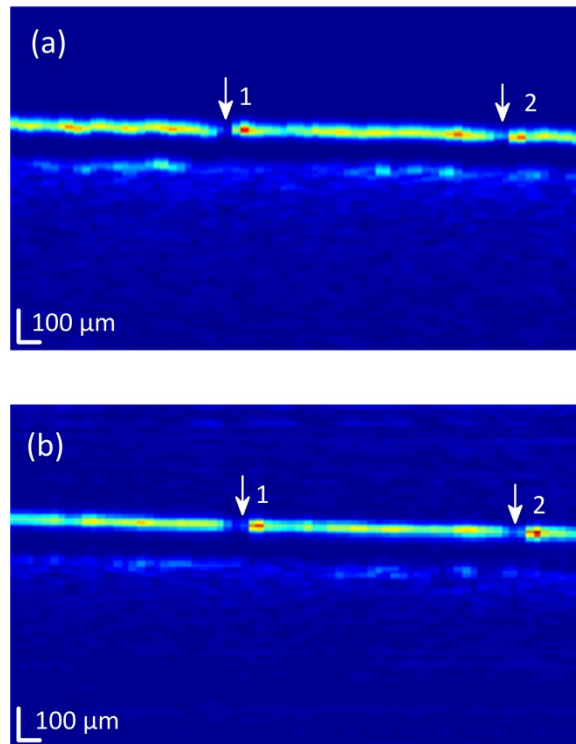


Fig. 7.2: Cross-sectional images taken from an epoxy coating on a carbon fiber composite measured by (a) TD-OCT and (b) FD-OCT. The arrows indicate the locations of microcracks within the coating.

7.2.3 Thickness Measurement

The second sample is a transparent Epikote Resin 1001 coating on a substrate of 99.5% pure AA1050 aluminum alloy. Fig. 7.3 (a) is a cross-sectional image acquired by fast FD-OCT measurement. The two bright lines indicate reflections from the front and back surfaces of the coating respectively. Compared with the carbon fiber composite shown in Fig. 7.2, it can be seen that the substrate of aluminum alloy in this application is more reflective rather than scattering. Therefore the thickness of this coating is easier to measure as it is determined from the distance between the two reflections, taking the coating refractive index of 1.55 into account. The refractive index was determined by calculating the ratio of the optical thickness, measured by OCT, to the real physical thickness measured by a thickness gauge (PosiTector 6000 FS, DeFelsko Corp, US). Fig. 7.3 (b) is one A-scan signal taken from the location of the dashed line in Fig. 7.3 (a). By calculating the distance between the two peaks the estimated thickness is 121 μm , very close to a thickness of 117 μm measured by a thickness gauge at the same spot.

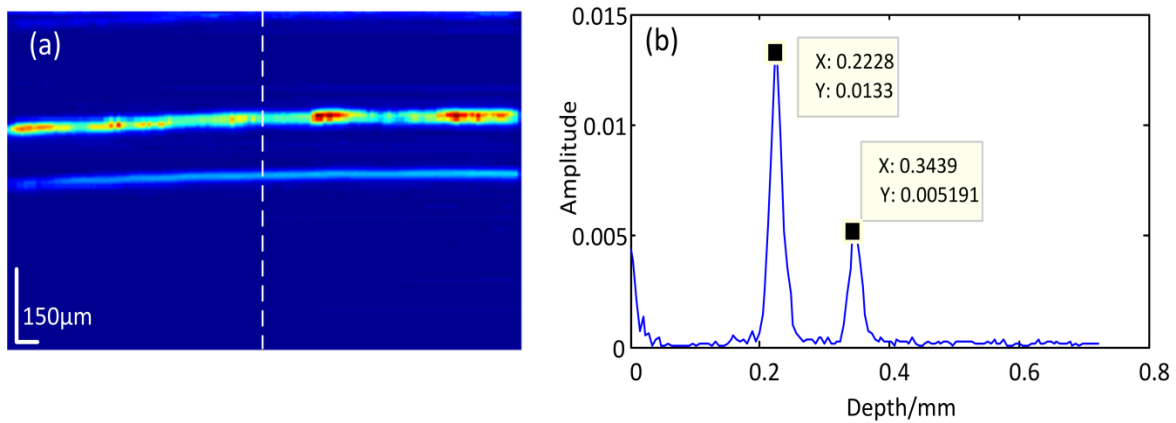


Fig. 7.3: (a) A cross-sectional and (b) an A-scan signal (taken from the dashed line in (a)) from an epoxy coating with alumina alloy substrate. The thickness of the coating can be determined by measuring the distance between the two reflection peaks from the front and back surfaces of the coating.

7.2.4 Discussion

The results presented in section 7.2.2 show that OCT is able to detect microcracks with a minimum width of 20 μm in a polymer coating. The detection of smaller cracks would be possible with an improved lateral resolution using an objective with high numerical aperture (NA), which is usually referred to as an Optical Coherence Microscope (OCM) [8]. However one should bear in mind that there is always a tradeoff between the beam size and the focal depth. The focal depth should be sufficient to encompass the entire axial scan range. Otherwise, tracking the focal depth by translating the focal lens along with the axial scan is necessary, as introduced in chapter 2.

The performance of TD-OCT and FD-OCT can be evaluated and compared based on results presented in Fig. 7.2. The imaging speed is always one of the most important characteristics of a measurement system. For TD-OCT it takes 3 seconds to record each A-scan and more than 7 minutes to record the complete cross-sectional image. While in FD-OCT even with a 20 ms integration time set for the CCD detectors to maximize the sensitivity, only 3 seconds was needed to display the whole layer structure, which is 150 times faster than TD-OCT. Moreover, due to the nonlinear sweep of the reference mirror discussed in chapter 4, TD-OCT suffers from image distortion in the axial direction. This is revealed by the relatively rough coating surface in Fig. 7.2 (a) imaged by TD-OCT, compared with Fig. 7.2 (b) obtained by FD-OCT. In FD-OCT this is not an issue as no mechanical movement is needed to record the A-Scan.

Besides, it is worth noting there is high amplitude signal at the beginning of the A-scan as shown in Fig. 7.3 (b). It is a disturbing term besides the source spectrum, denoted by the mutual interference of all backreflected waves and is located around the depth $z = 0$, as introduced in chapter 2. Therefore in FD-OCT an offset of 200 μm to the surface of the sample is necessary to separate it from object signal [9]. The drawback of this processing is that it further limits the detectable depth in FD-OCT. Taking the customized OCT system as an example, only a depth of only 1.11 mm is achievable in a polymer-based material with 1.55 average refractive index, which limits the application of FD-OCT for relatively thick materials such as glass fiber composites as discussed in chapters 5 and 6.

For the thickness measurement, the slightly difference in results between OCT and the thickness gauge could be caused by measurement errors in both instruments. The thickness gauge (PosiTector 6000 FS, DeFelsko Corp, US) has an measurement uncertainty of $\pm 2 \mu\text{m}$ [10] and OCT could have an error up to 11 μm , which is decided by the axial resolution of the customized OCT system in the polymer coating. The prime step for thickness measurement in OCT is to locate the signal peaks, as shown in Fig. 7.3(b). Thus a higher axial resolution (for a narrower bandwidth of the interference signal) and enhanced SNR (for fewer ripples in the signal peaks) should improve OCT accuracy for thickness measurement.

It is needed to point out that currently most thickness gauges used for coating thickness measurement are based on magnetic or eddy current principles [10] which require a metal substrate and are difficult to use for the measurement of multiple-layer coatings. Some advanced thickness gauges¹ based on ultrasonic methods can break this limitation [11], but they cannot provide high spatial resolution as one point measurement needs a surface area in millimeter range. However OCT does not have all these limitations. It only requires the coating to be penetrable for light and a small refractive index difference between the coating and substrate or two neighboring coatings. Besides, the thickness distribution can also be easily observed from a cross-sectional OCT images. These advantages could push OCT to become an effective tool for semi-transparent coating thickness measurement.

¹ E.g., QuintSonic 7 (ElektroPhysik GmbH, Germany) enables measurement of up to 5 coatings in a single operation. The measurement range is from 10 to 7500 μm with an accuracy of 4 μm [11].

7.3 Study of Front and Back Faces of a Wooden Panel Painting

7.3.1 Introduction

The conservation of artwork is an important topic in preserving cultural heritage. Therefore, diagnosis techniques for structural and chemical deterioration are needed to monitor the condition of objects for their preservation. Currently, increasing attention is being given to OCT in artwork diagnostics and restoration. Besides high resolution and reasonable penetration depth, OCT is non-invasive and can be used in situ, which are probably the two most important advantages over sampling collection due to conservation ethics [12]. A review paper in this field has been published in 2011 by Targowski [2]. OCT has been used to evaluate the structure of paintings [13-15], historical glass [16, 17], and other semi-transparent objects, e.g. jade [18], porcelain and faience [19]. During the examination of paintings, the thickness of the varnish layer is interesting and is easy to detect due to its transparency. However, because of high absorption or scattering, the paint and substrate layers are difficult to analyze. Szkulmowska et al. [20] performed a systematic study on the applicability of OCT to the imaging of paint layers. They analyzed 47 commonly used pigments with two OCT systems working at center wavelengths of 1550 nm and 823 nm respectively. As expected, the OCT system working at longer wavelength is better suited for this type of application since 22 of the selected paints are penetrable for the 1550 nm light source while only 16 paints are penetrable for the 823 nm light source.

The aim of this section is to characterize a wooden panel painting using OCT with a 1550 nm light source. The study focuses on both front and back faces of the painting. This includes structural imaging of varnish and paint layers, the evaluation of defects, e.g. crack and loss of structural layers, and 3D reconstruction of a knot with drilled holes. The achievements and deficiencies of the current OCT system for this painting application, together with further improvements are discussed at the end of this section.

7.3.2 Sample Description

The painting shown in Fig. 7.4 is a specimen for research, manufactured by conservators at the by National Gallery of Athens, Greece. As shown in Fig. 7.5, the painting has a wooden panel as the substrate. Materials such as rabbit skin glue, canvas, and gesso were prepared consequently above the wood before reaching the paint layer. Nearly half of the painting surface was covered by a thin layer of gold lying on a bole, while the other half area was overlaid by red and green pigments mixed with egg yolk, as shown in Fig. 7.4. Above the

pigment and gold layers, a varnish layer was added for protection from dust and other atmospheric contaminants.



Fig. 7.4: Photograph of a wooden panel painting for OCT measurement.

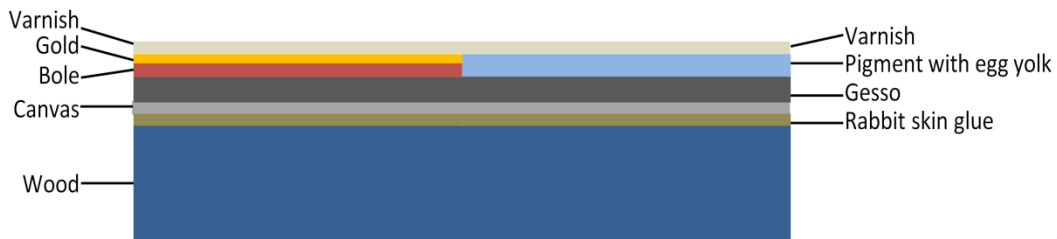


Fig. 7.5: Stratigraphy of a wooden panel painting for OCT measurement.

To simulate the degradation during aging, the painting was thermally treated following the oxidative type of ageing, in which the sample was heated in an oven with maximum air recycling. Currently the defects of the painting include crack and loss of pigment, as shown in the two enlarged images at the right of Fig. 7.6. The OCT testing will focus on these areas and on areas with different paints, indicated by the three arrows with labels (a), (b) and (c) shown in Fig. 7.6.

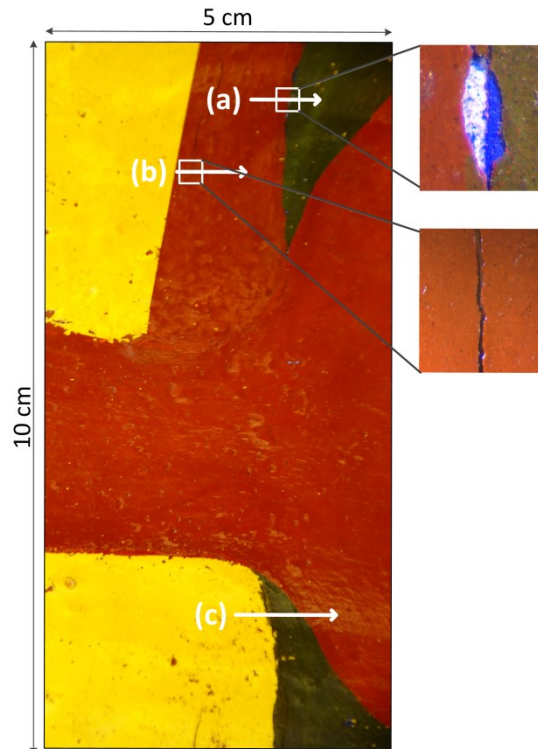


Fig. 7.6: A thermally aged wooden panel painting. The white arrows indicated by (a), (b) and (c) are the OCT scanning regions. The two enlarged images on the right are the areas indicated by white squares of two defects of the painting: a crack and loss of pigment.

7.3.3 Front Face Characterization

The three white arrows in Fig. 7.6 indicate the OCT scanning regions. Scanning line (a) and (b) with a length of 8 mm, go through the areas which are covered by red and green pigments and have the defects stated above. Scanning line (c) on the other edge of the painting travels across the areas of gold, green and red pigments respectively, with a length of 15 mm. The OCT cross-sectional images from these three regions are shown in Fig. 7.7. The optical reflectivity along the depth of the specimen is displayed by false color with logarithm scale.

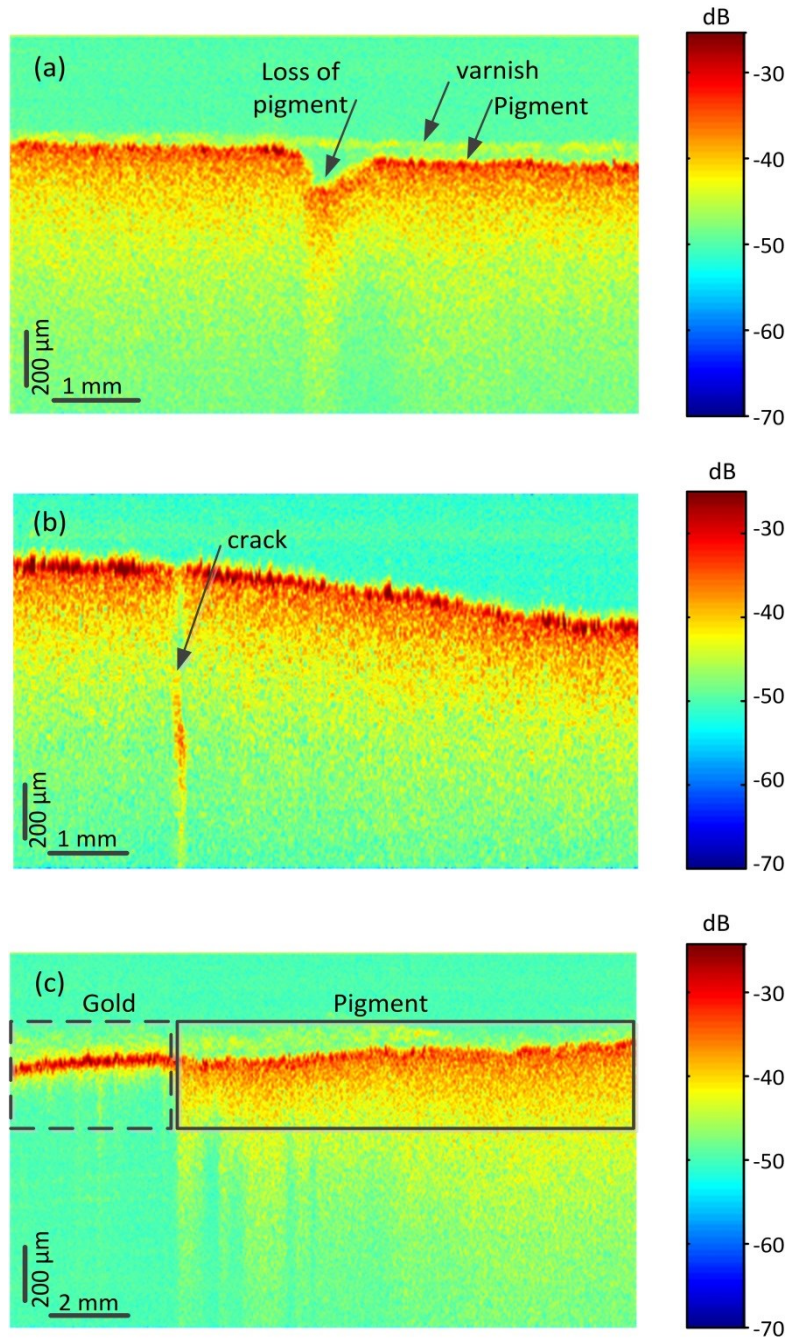


Fig. 7.7: Cross-sectional images from the regions indicated by white lines in Fig. 7.6.

The first observation regards the varnish layer, shown as the strip between the first and second bright lines in Fig. 7.7(a). These bright lines indicate the light reflections from the front and back surfaces of the varnish layer. Taking an average refractive index of 1.5 into account [21], the estimated thickness of the varnish layer is approximately 20-40 μm , which is not evenly distributed. However, this type of observation becomes difficult in Fig. 7.7(b) and (c). It is noticed that the first light line indicating the reflectivity of the varnish front surface in

Fig. 7.7(a) has disappeared in Fig. 7.7(b) and is discontinuous in Fig. 7.7(c). One possible reason is that the varnish layer was lost during conservation. It could also be that the thickness of the varnish layer in these areas is below the axial resolution of the OCT imaging.

The second observation, by comparing the different imaging areas, is that the gold layer is more reflective than green and red pigments. This can be seen from Fig. 7.7(c). The gold surface is indicated by the brightest line in the area pointed out by the black dashed square. Under the gold layer, the image gives no sign of detectable reflection. This means the light from the current OCT system is strongly reflected by the gold, which limits the penetration to deeper layers of the sample. However, at the areas with green and red pigments as shown in the black solid square in Fig. 7.7(c), light not only strongly reflects on the surface of the pigment, but also goes into the substrate layers. However, due to the dense speckles, it is difficult to tell the actual penetration depth and the layer interfaces underneath the pigments.

The last observation is about the defects of the painting. At the arrow in Fig. 7.7(a), a notch with 800 μm width at the paint surface and 100 μm depth can be observed. This is coincident with the fact that no pigment layer exists at the area in the micrograph shown in Fig. 7.6. Another defect is a crack observed in Fig. 7.6. Indicated by the arrow in Fig. 7.7(b), the crack can be identified where a strong reflection comes from deep in the painting structure, instead of the paint surface. The depth of the crack is approximately 300 μm and can be easily determined from the cross-sectional image. However the width of the crack is difficult to measure quantitatively since weak reflections still can be detected above the crack at the height level of the paint surface. This indicates the crack width could be smaller than the lateral resolution of the OCT image which is 20 μm .

7.3.4 Back Face Characterization

The painting tested in section 7.3.3 is based on a wooden panel. On the back surface of the panel as shown in Fig. 7.8, the textile and a knot can be clearly seen. In order to release residual stresses in the knot region of the painting, 7 drill holes were made in the knot. The task of this research is to reconstruct the 3D surface of this knot area and to check if the drill holes damage other layers of the painting.

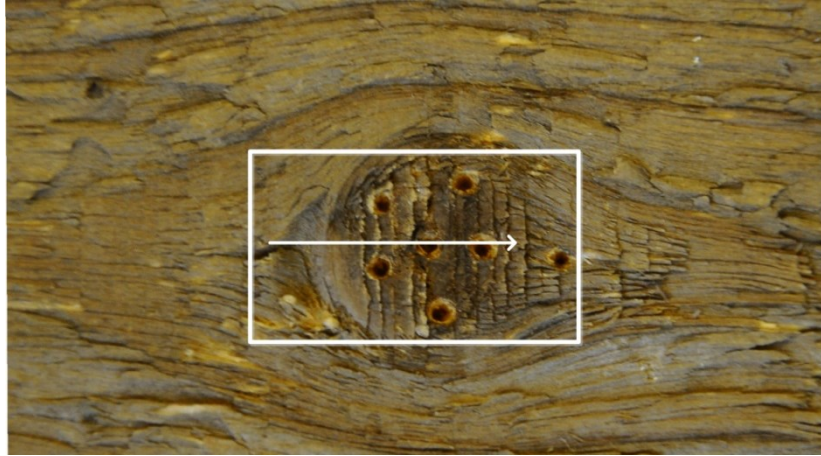


Fig. 7.8: A wooden panel used as painting substrate. The white arrow and square indicate the OCT scanning line and area where a knot with drilled holes exists.

Fig. 7.9 shows one cross-sectional image of the wooden panel at the region where the arrow in Fig. 7.8 is located. It can be seen that the wooden sample is partly penetrable by OCT, but the interior structure is barely observed due to the dense speckles. However, the brightest line from left to right can show the surface profile of the wooden panel. The label '1' indicates the area of a notch with a maximum 2 mm width and 1 mm depth. The labels '2' and '3' indicate two drill holes which the scanning line passes across. It is noted that the hole with label '2' has a width of 1 mm and a depth of 1.5 mm, while the hole with label '3' has a width of 1.5 mm and a depth that is out the range of the cross-sectional image. A more detailed 3D surface profile is needed for a comprehensive understanding of the knot area of the wooden panel.

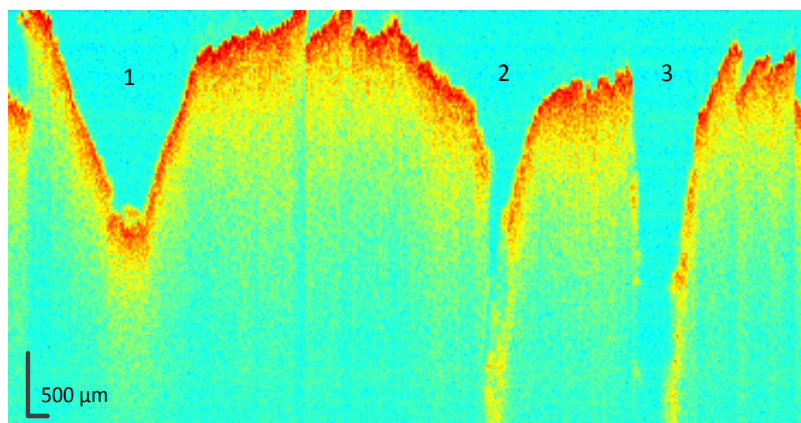


Fig. 7.9: A cross-sectional image obtained from the region where the arrow in Fig. 7.8 is located. The label '1' indicates the notch of the knot, and the label '2' and '3' indicate two drill holes.

Fig. 7.10 demonstrates the 3D surface profile from the area indicated by the square in Fig. 7.8. Due to the relatively large axial scanning range, TD-OCT was used for this application. The image size is 24 mm in length and 12 mm in width. It was obtained by 3D OCT imaging followed by locating the first interference signal peak in each A-scan signal. In Fig. 7.10, besides the surface texture, the notch and 7 drill holes can be clearly seen. The deepest notch and drill hole with regard to the highest knot surface are 2 mm and 3.7 mm in depth respectively. Considering the 10 mm thickness of the wooden panel, the drill holes have not penetrated the wooden layer and should not affect the painting directly. However the residual stress in this area and its influence for the painting conservation is still an unknown question.

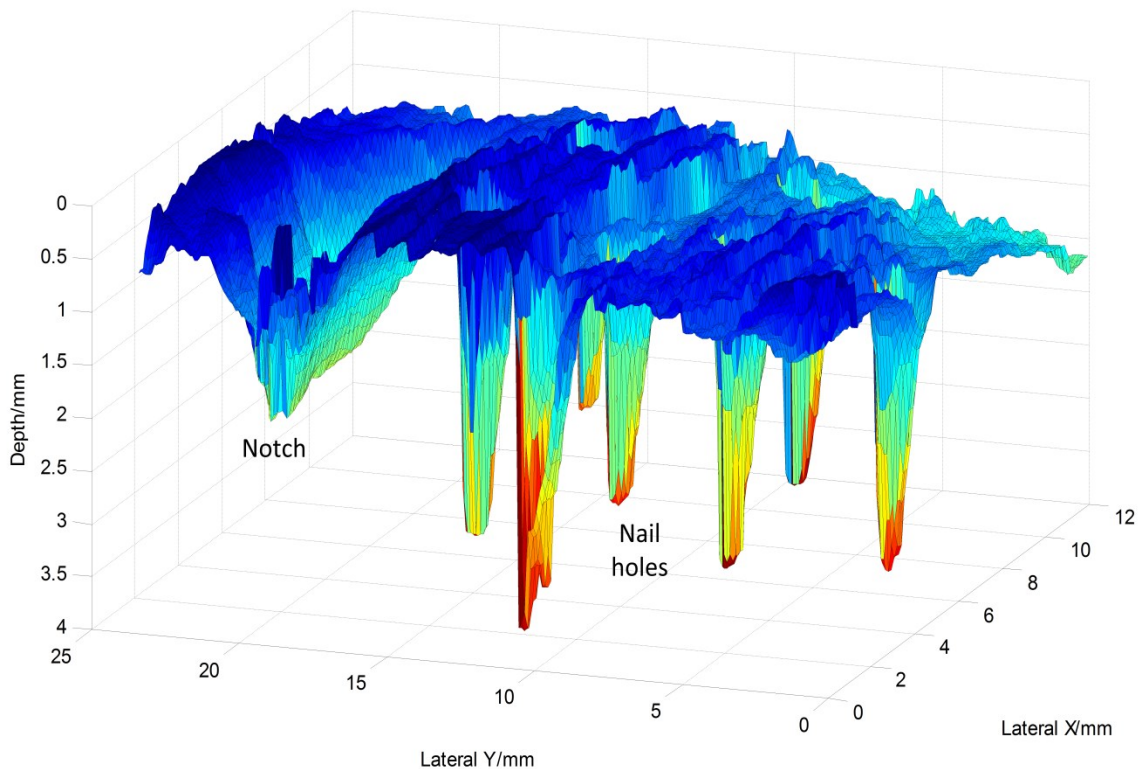


Fig. 7.10: A 3D surface profile from the area indicated by the square in Fig. 7.8.

7.3.5 Discussion

As the results in section 7.3.3 show, the current OCT system is able to detect the varnish layer and some defects, e.g. crack and loss of varnish and pigment layers. However structural imaging of the paint layers could still be difficult. Even with the longer wavelength (1550 nm) light source employed for the OCT system, the gold layer of the painting is not penetrable. The layers of green and red pigments can be penetrated, but the speckles caused by strong

interior scattering bring artefacts and blur the layer edges. Recently a paper published by Liang et.al [22] shows that the best spectral window for the OCT imaging of subsurface structure of paintings is around $2.2 \mu\text{m}$ where a good balance between light scattering and absorption is found. However, one of the challenges in building an OCT system in this spectral window is looking for a stable and cost-effective light source. According to Eq. 2.16, OCT working at longer wavelengths needs a light source with much broader bandwidth to achieve the same depth resolution as the ones using visible sources.

Fig. 7.11 demonstrates one A-scan signal from the cross-sectional image shown in Fig. 7.7(a). Obviously it is difficult to correspond reflection peaks with the stratigraphy of the painting since the amount of signal peaks shown in Fig. 7.11 is more than the amount of the painting layers. Moreover, some of these signal peaks appear randomly during each A-scan and construct high-contrast and dense speckles in the cross-sectional images. These speckles largely deteriorate the OCT image quality and hinder the structure detection of the painting. In chapter 4, a median filter is selected as the last step to suppress the speckle noise in glass fiber composites. However, it is not effective in the painting application due to the dense speckles. Further improvement in speckle reduction is still needed.

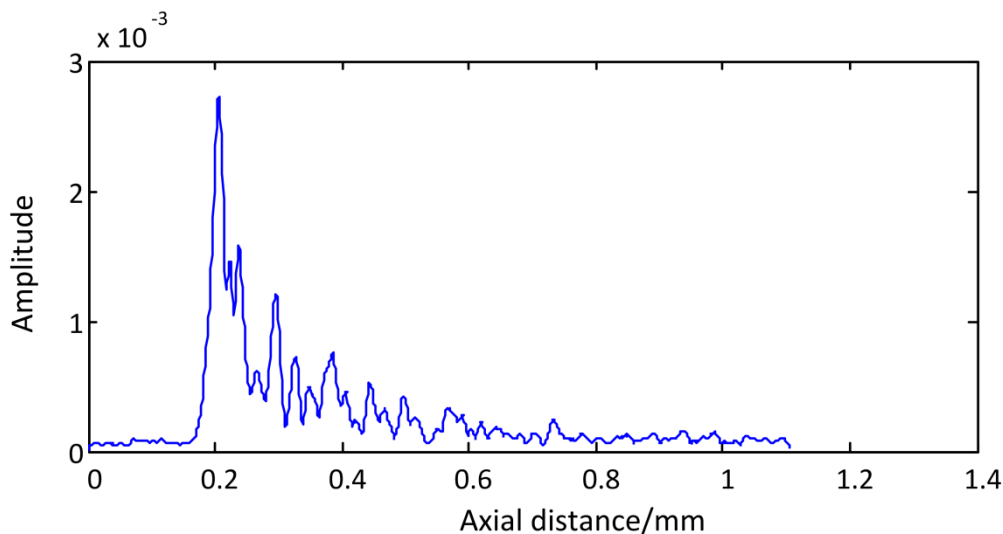


Fig. 7.11: One A-scan signal from the cross-sectional image shown in Fig. 7.7(a).

OCT can be used to reconstruct the surface profile of a specimen due to a fact that no matter whether the specimen is penetrable by light, the reflection from the surface of the specimen can always be detected. Therefore the axial location of the first reflection peak in each A-scan decides the height of each surface spot and thus a surface profile can be built with 3D OCT scan. The accuracy of the surface height measurement is decided by the axial

resolution of the implemented OCT system, which is 17 μm in the air. The results presented in section 7.3.4 show that OCT could be an effective 3D scanner for the reconstruction of an object surface profile. However, in the current OCT system, both TD and FD-OCT measurement is implemented pointwisely on the surface. For real-time 3D surface profile measurement, full-field OCT (FF-OCT), which acquires an en face image in one shot could be more suitable for this type of application.

7.4 Conclusions

In summary, this chapter has demonstrated OCT as a novel NDT tool to investigate polymer coatings and a wooden panel painting. Both quantitative and qualitative information of the coating specimens such as thickness, microstructure and defects have been obtained successfully. Improvements in axial and lateral resolutions are still needed to increase the accuracy in coating thickness measurement and to detect microcracks with less than 20 μm width, respectively. For the characterization of the painting, the varnish thickness and defects such as crack and loss of pigments were determined from the cross-sectional images. To obtain a structural image that can clearly show the painting stratigraphy, an OCT system working at a longer wavelength combined with speckle reduction techniques are requested. At the back face of the painting, the wooden panel was characterized by 3D surface reconstruction of a knot with drill holes. The information such as depth of the notch and drill holes was obtained. To realise real-time 3D surface profile measurement, a full-field OCT is needed due to its fast en face imaging.

References

- [1] G. Hanneschläger, A. Nemeth, C. Hofer *et al.*, “Optical coherence tomography as a tool for non destructive quality control of multi-layered foils,” Proceedings of the 6th NDT in Progress, (2011).
- [2] P. Targowski, and M. Iwanicka, “Optical Coherence Tomography: its role in the non-invasive structural examination and conservation of cultural heritage objects—a review,” Applied Physics A, 106(2), 265-277 (2011).
- [3] R. A. Ryntz, and P. V. Yaneff, [Coatings of polymers and plastics], CRC Press (2003).

- [4] J. H. Osborne, K. Y. Blohowiak, S. Taylor *et al.*, "Testing and evaluation of nonchromated coating systems for aerospace applications," *Progress in Organic Coatings*, 41(4), 217-225 (2001).
- [5] G. Bierwagen, "Next generation of aircraft coatings systems," *Journal of Coatings Technology*, 73(915), 45-52 (2001).
- [6] M. Westwood, J. Webster, R. Day *et al.*, "Oxidation protection for carbon fibre composites," *Journal of Materials Science*, 31(6), 1389-1397 (1996).
- [7] G. Swallowe, [Ductile-brittle transition], Springer (1999).
- [8] J. Schmitt, S. Lee, and K. Yung, "An optical coherence microscope with enhanced resolving power in thick tissue," *Optics Communications*, 142(4), 203-207 (1997).
- [9] B. E. Bouma, and G. J. Tearney, [Handbook of optical coherence tomography], Marcel Dekker (2002).
- [10] PosiTector 6000 FS coating thickness gauge,
<http://www.defelsko.com/p6000/og/p6000.php?g=FS&m=1>.
- [11] QuintSonic 7 coating thickness gauge,
<http://www.elektrophysik.com/products/coating-thickness/quintsonic-7.html>.
- [12] H. Liang, M. Cid, R. Cucu *et al.*, "En-face optical coherence tomography: a novel application of non-invasive imaging to art conservation," *Optics Express*, 13(16), 6133-6144 (2005).
- [13] P. Targowski, M. Iwanicka, L. Tyimińska-Widmer *et al.*, "Structural examination of easel paintings with optical coherence tomography," *Accounts of Chemical Research*, 43(6), 826-836 (2009).
- [14] H. Liang, B. Peric, M. Hughes *et al.*, "Optical coherence tomography for art conservation and archaeology," *Optical Metrology*, 661805-661805-12 (2007).

- [15] H. Liang, M. Gomez Cid, R. Cucu *et al.*, "Optical coherence tomography: a non-invasive technique applied to conservation of paintings," *Proceeding of SPIE*, 5857, 58570W-58570W-9 (2005).
- [16] P. Targowski, B. Rouba, M. Góra *et al.*, "Optical coherence tomography in art diagnostics and restoration," *Applied Physics A*, 92(1), 1-9 (2008).
- [17] H. Liang, B. Peric, M. Hughes *et al.*, "Optical coherence tomography in archaeological and conservation science - a new emerging field," *Proceeding of SPIE*, 7139, 713915-713915-9 (2008).
- [18] M. L. Yang, C. W. Lu, I. J. Hsu *et al.*, "The use of optical coherence tomography for monitoring the subsurface morphologies of archaic jades," *Archaeometry*, 46(2), 171-182 (2004).
- [19] M. L. Yang, A. M. Winkler, J. K. Barton *et al.*, "Using optical coherence tomography to examine the subsurface morphology of chinese glazes," *Archaeometry*, 51(5), 808-821 (2009).
- [20] A. Szkulmowska, M. Góra, M. Targowska *et al.*, [Applicability of optical coherence tomography at 1.55 μm to the examination of oil paintings], Springer (2007).
- [21] R. S. Berns, and E. R. de la Rie, "The effect of the refractive index of a varnish on the appearance of oil paintings," *Studies in Conservation*, 48(4), 251-262 (2003).
- [22] H. Liang, R. Lange, B. Peric *et al.*, "Optimum spectral window for imaging of art with optical coherence tomography," *Applied Physics B*, 111(4), 589-602 (2013).

8

Conclusions and Recommendations

As stated in chapter 1, the aim of this thesis is to use OCT as a novel NDT technique for material structure characterization and damage detection. Besides an overview of the OCT fundamentals and developments, the thesis is mainly driven by three tasks: instrument design, signal processing, and applications. The following conclusions and recommendations are organized with these three aspects.

8.1 Conclusions

8.1.1 Conclusions from Instrument Design

A hybrid TD-FD-OCT system working at 1550 nm wavelength has been built. TD-OCT has the advantage of a large A-scan range (50 mm) and high SNR (50 dB), while FD-OCT system has tremendous superiority in fast imaging (1000 A-scans/s) due to no movement of the reference mirror. These two kinds of measurement can be implemented based on the user request in the integrated OCT system, e.g. improved imaging depth or speed.

In more detail, a fiber-optic interferometry was used with a light source centered at 1550 nm, where light is less scattering in polymer-based materials and thus a deeper light penetration can be expected. The axial resolution, decided by the wavelength and bandwidth of the light source is 17 μm in the air and 11 μm in the polymer-based material (considering 1.55 average refractive index of the specimen). The lateral resolution, determined by the beam size, is 20 μm with 1.24 mm depth of focus. In TD-OCT, an electrical ODL was equipped in the reference arm to sweep the pathlength at 1.7 mm/s, and a balanced detector was applied to

remove the excess noise in an interference signal. In FD-OCT, a spectrometer with 160 nm spectral range and 512 detector elements was employed, which can reach 1000 scans/s and 1.03 mm depth scan range. For both TD and FD-OCT, a pair of translation stages with 4 mm/s velocity and 28 mm travelling range, were used to shift the sample beam for the lateral scans.

8.1.2 Conclusions from Signal Processing

In TD-OCT, A bandpass filter was designed to separate the interference signal from the DC photocurrent and noise. Afterwards, the envelope detector was selected as the ideal method to extract the envelope of the band-limited interference signal. As the last step, a 2D median filter was implemented to reduce the speckle noise. The calculated SNR of TD-OCT reaches 50 dB, which allows the detection of weak reflectors from deep in the specimen.

In FD-OCT, the raw data was firstly processed to remove the influence from the optical source and dark noise from the CCD detectors. It was then linearly resampled to evenly spaced intervals of wavenumber, instead of wavelength. With an inverse Fourier transform, one depth profile was recovered and a cross-sectional image was constructed by accumulating a series of depth profiles. The quality of cross-sectional images can be further improved by merging multiple images with different pathlength offsets. Although the SNR of FD-OCT is not comparable with that of TD-OCT, the imaging speed and high axial linearity targets FD-OCT applications in thickness measurement and microcrack detection in thin films.

8.1.3 Conclusions from Applications

The designed OCT system was first applied to the study of glass fiber composite. TD-OCT was used for a large depth scan and its penetration depth in the tested glass fiber composites could be as deep as 2.85 mm. The fiber tows are observable and could be as pronounced as the microscope image if there is an obvious difference of refractive index between the glass fiber and polymer matrix. To test the defects in a glass fiber composite for a wind turbine blade, a delamination was first observed in both 2D cross-sectional and 3D volumetric images. The delamination crack was found to propagate initially along the fiber tow/resin boundary. Multiple reflections detected at the tip of the delamination could be caused by the bridging fibers that exist between the delamination crack and still connect the upper and lower layers of the composite. For a better understanding of the delamination and its propagation, the glass fiber composite has also been tested by incremental loading. High-resolution volumetric

images obtained by OCT were further processed to reconstruct 3D crack surface profiles, from which a full field 3D view of the delamination crack was given. The $\pm 45^\circ$ lines in the crack surface profiles indicate the fiber orientations. They were also used for the prediction of crack jumps.

Besides, the study explored the use of optical coherence elastography (OCE) for deformation measurement of glass fiber composites, for the first time to the best of our knowledge. The developed OCE system based on speckle tracking was first evaluated by a test of rigid body translation. Then experiments were implemented for a set of glass fiber composites under tensile test and three point bending. The results show that OCE can measure internal displacements of a glass fiber composite in the range from a few micrometers to hundreds of micrometers. The cross-sectional displacement maps clearly show the structural features and structural variations, which could provide supplementary understanding of the mechanical properties of glass fiber composites.

Additionally, some further NDT applications were selected. The integrated OCT system was used to characterize polymer coatings. Both quantitative and qualitative information from the specimens, such as thickness, microstructure and defects were obtained successfully. By comparing analysis results from TD and FD-OCT measurements, two microcracks in an epoxy coating were identified from the discontinuity of the surface reflection lines in the OCT cross-sectional images. The superiority of FD-OCT in imaging speed 150 times faster than TD-OCT was also observed during this testing, and the speed ratio could reach 3000 when using the minimum spectrometer integration time of 1 ms. With a cross-sectional image from an FD-OCT measurement, the thickness distribution of another epoxy coating was characterized by measuring the distance between the two reflection peaks from front and back surface of the coating. Compared with the traditional coating thickness gauge, OCT has the advantages in high spatial resolution and multiple-layer coating measurement.

The OCT system was also used to investigate a wooden panel painting. At the front face of the painting, the varnish thickness and defects such as cracks and loss of pigment were determined from the cross-sectional images. Additionally, it was noted that the gold layer is much more reflective than the green and red pigments. At the back face of the painting, the 3D surface profile of a knot of the wooden panel was reconstructed. Information such as depth of the notch and drill holes was obtained.

8.2 Recommendations

8.2.1 Recommendations for Instrument Design

OCT developments in NDT field, similar to its biomedical counterparts, follow one general principle: to obtain more information in less time. ‘More information’ from a sample first requires a deeper penetration and a higher resolution, which are mainly dependent by the light source. As reviewed in chapter 2, OCT systems using near-infrared light source centered at 1.55 μm or even longer wavelength have the advantage of deeper penetration due to less light scattering in a material. However they are mostly at the cost of lower axial resolution, which is proportional to the square of the light center wavelength and inverse proportional to the bandwidth of the light source. Following this direction, further OCT developments should use novel light sources at 2 μm or even longer wavelengths with ultra-broad bandwidth. Furthermore, if a swept light source in the demanded wavelength range is reliable, swept source OCT (SS-OCT) is recommended to obtain the information in ‘less time’. As new generation technology, SS-OCT has a similar high imaging speed to FD-OCT, but without the drawbacks inherent to FD-OCT, e.g. imaging depth limitation due to the limited number of pixels in CCD devices, and loss of sensitivity with depth.

Another direction of recommendation could be reductions in complexity, size, and cost of an OCT system. Currently most commercial OCT systems are bulky and table mounted, limiting the portability of the instruments. Due to the need of in situ imaging, e.g., for an industrial test or artwork conservation, a compact and robust system, such as handheld OCT is essential for this type of applications. As the first step, the OCT probe could be separately designed as a handheld device that can easily reach a specimen in a production line or under some mechanical testing.

8.2.2 Recommendations for Signal Processing

Speckle noise reduction is still the most important task during the signal processing of OCT data. Although OCT is characterised by superb spatial resolution, it is sometimes difficult to reveal the layered structure due to speckle noise. A median filter could be an easy way to remove some speckles, but it is not effective when the speckles densely exist in an OCT image. Besides, the loss of some detailed information provided by the original OCT image is inevitable as the image resolutions are decreased during the filtering processing.

An additional research on speckle reduction is required to obtain OCT images with high structural contrast. One direction is to understand the relationship between the scattering

properties of materials and the speckles in OCT images. Light scattering within a sample can be simulated and analysed comparably with corresponding OCT images, which could help us to understand the origin of speckles. Another direction is looking for new speckle reduction techniques. Advanced signal processing algorithm should be introduced.

8.2.3 Recommendations for Applications

With the development of SS-OCT as recommended above, OCT applications in NDT field could be in real time and in situ. Based on the results presented in this thesis, one suggestion for further applications could be combining OCT with dynamic mechanical testing for material characterization. For instance, an OCT prototype can be placed next to a fatigue machine to monitor the delamination growth in glass fiber composites. Another example is utilizing OCT to monitor the interior 3D displacement and strain of a specimen under loading test. However, this requires further development of the elastography technique that enables fast tracking of both small and large displacements. Another suggestion for further application is related with some in situ measurement. The portable OCT system can be bought into a museum for artwork conservation. It can also be used in industry on a production line for the quality assessment of materials such as polymer coatings and glass fiber composites. Additionally, more experimental work is still needed to explore OCT applications to a variety of scattering materials. OCT could benefit more materials as a novel NDT tool for structural imaging and health diagnosis.

Samenvatting

Optical coherence tomography (OCT, vertaling: optische coherentietomografie), is een niet-invasieve en contactloze beeldvormingsmethode met een hoge resolutie, waarmee twee- of driedimensionale dwarsdoorsnedes gemaakt kunnen worden van troebele media. In de afgelopen 20 jaar is OCT uitgebreid toegepast en doorontwikkeld voor de biomedische diagnostiek, maar toepassingen in *non-destructive testing* (NDT, vertaling: niet-destructief onderzoek) zijn tot heden achtergebleven.

Het doel van deze thesis is om OCT te gebruiken als een nieuwe niet-destructieve techniek om materiaalstructuren te karakteriseren en schade te detecteren. Naast een overzicht van de fundamentele en ontwikkelingen van OCT, richt deze thesis zich ook op drie andere onderwerpen: instrumentontwerp, signaalverwerking en toepassingen.

Allereerst is er een geïntegreerd OCT systeem ontwikkeld waarin gebruikt wordt gemaakt van een bron met een golflengte van 1500nm. Dit systeem combineert tijdsdomein (TD) en frequentiedomein (FD) OCT zodat beide type metingen met één instrument gedaan kunnen worden. Het voordeel van TD-OCT is dat diepere A-scans gemaakt kunnen worden met een hoge signaal-ruisverhouding, terwijl FD-OCT-metingen veel sneller gedaan kunnen worden door het ontbreken van een bewegende referentiespiegel. Eén van deze twee meettechnieken kan gekozen worden afhankelijk van de eisen van de gebruiker van dit hybride systeem, zoals goede dieptesresolutie of hoge meet snelheid.

Voor de TD-OCT is een envelop-detector gekozen als de ideale methode voor het demoduleren van het signaal. Een bandfilter en een tweedimensionale mediaanfilter worden respectievelijk voor en na de demodulatie toegepast om de *speckle* of korrelige ruis van het systeem te verminderen. De FD-OCT data worden eerst bewerkt zodat de invloed van de lichtbron en van zogenaamde *donkere ruis* van de *charge-coupled device* detectoren (CCD, vertaling: ladinggekoppeld component) verminderd worden. De data worden daarna lineair verschaald om uniforme intervallen van golfgetallen in plaats van golflengtes te verkrijgen. Met behulp van een fouriertransformatie kan het diepteprofiel achterhaald worden en kan een dwarsdoorsnede geconstrueerd worden, door een serie van diepteprofielen te combineren.

De voornaamste toepassing van het ontworpen OCT-systeem betrof glasvezelcomposieten: voor modellen van dat materiaal kan de microstructuur als twee- of driedimensionale dwarsdoorsnedes in beeld worden gebracht. In het onderzoek werd nadruk gelegd op de ontwikkeling van delaminatie in glasvezelcomposieten die gebruikt worden voor windturbinevleugels. Het materiaal werd onderworpen aan stapsgewijze belasting. Afbeeldingen van een volume van de monsters werden gemaakt en verder bewerkt om de driedimensionale oppervlakteprofielen van de barsten in beeld te brengen. Hiermee kon de groei van breuken in composieten bestudeerd worden. Daarnaast werden de OCT metingen aangevuld met zogenaamde *optical coherence elastography* (OCE, vertaling: optische coherentie-elastografie) om deformaties in glasvezelcomposieten te onderzoeken; voor zover bekend is dit de eerste keer dat dit gedaan is. Dit systeem, gebaseerd op de beweging van *speckle*, werd getest door eerst een referentiemeting te doen met een bekende lineaire verplaatsing van een testobject. Daarna zijn er metingen gedaan op glasvezelcomposieten die werden onderworpen aan trekproeven en driepuntsbuigproeven. De resultaten lieten zien dat OCE gebruikt kan worden om interne verplaatsingen in glasvezelcomposieten van groottes variërend van enkele micrometers tot honderden micrometers te meten.

Naast de genoemde toepassingen worden ook andere toepassingen gepresenteerd in de thesis, zoals metingen aan de dikte en de beschadigingen van polymeercoatings en de karakterisering van de microstructuur van een schilderij op een houten paneel. De resultaten van deze metingen laten zien dat het ontworpen OCT systeem ook potentiële andere toepassingen heeft. Aanbevelingen over verdere ontwikkelingen van het ontwerp van het OCT systeem en mogelijke verdere toepassingen worden aan het einde van de thesis gepresenteerd.

Acknowledgements

The research presented in this thesis was carried out in the Aerospace NDT Laboratory of TU Delft, Faculty of Aerospace Engineering of TU Delft. It is a multidisciplinary work which cannot be completed without the support of many people. I wish to thank all of those who contributed to this research.

I want to give my deepest thank to my promoter Prof. dr. ir. Rinze Benedictus who gave me the freedom and encouragement to perform my research. I very much appreciated that he trusted my judgement and approved the budgets I needed for the optical components, which was curial during the instrument development. I would like to express my sincere gratitude to my copromotor Dr. Roger M. Groves for his daily supervision. Honestly it was a huge challenge for me to start this novel project almost from scratch. Thanks to Roger who showed a lot of patience with me, discussed every question I had, and continuously encouraged me on every progress I made. I had pleasure and privilege to work with a supervisor who always can give me timely suggestions and feedback on my work and manuscripts. Thank you, Roger.

This research project could not have been accomplished without the sponsorship of China Scholarship Council (CSC). Special thanks go to CSC and its staff for the valuable support.

During my early stage of the instrument development, I contacted several optical and mechanical component suppliers and received a lot of practical advices on how to improve my system. So I would like to thank the technical support particularly from Thorlabs GmbH, OZ Optics Ltd., Ocean Optics Inc., and Zaber Technologies Inc. I am also very grateful that Dr. David Stifter (Johannes Kepler University, Austria) could share his experience with me on building a first OCT instrument. Although we did not know each other before, he kept supporting me with his knowledge. I appreciate his selfless help.

I would like to express my gratitude to all committee members who have dedicated part of their time to review this thesis and participated in the defence. I am sincerely grateful to Prof. P. Targowski and Prof. L. J. van Vliet for their corrections and suggestions on how to improve the thesis.

The Aerospace NDT Laboratory probably is the most mysterious place within the Aerospace Structures and Materials Laboratory since it is usually ‘sealed’ for safety reasons. However, people working inside are quite active and new ideas come up all the time to make the material testing possible with different NDT techniques. I am proud to be one member in the lab and to work together with my labmates: Nick, Eduardo, Pedro, Henk, Beril, Raf, Maria, Andrei, Vassilis, Donghang, Victor, Guyonne, Rafael. Thank you for all the help in the lab and your feedback on my presentations and manuscripts. Especially, I am thankful to Vishal for the preparation of my specimens and Liesbeth for the translation of my thesis summary. My thanks also go to lab technicians, Berthil, Hans, Frans, and staff working in the workshop who gave necessary help on my experimental setup.

The 4-years study at TU Delft could not have been fun and successful without my colleagues in the Structure Integrity & Composites Group. First I want to thank the group secretary Gemma van der Windt for managing all the paper work in extremely efficient manner. I also thank her and Mayank for organizing all the wonderful sports and dinner events. My officemates: Rafiullah, Salim, Mehdi, Macos, Chongxin, Hao, Yao, Nikos, Lucas, Leila, Adrian F, and Cornelis, thank you for all the support and fun. I enjoyed the nice atmosphere in the office. My thanks also go to Gustavo, Adrian L and Ilias who have been managing the GS meeting. I am grateful to all the colleagues who paid attention on my work and gave me suggestions on the GS or other occasions.

In the past 4 years, my life in Delft could not be more satisfying, which mainly thanks to a large Chinese community here. I want to thank all of my colleges and friends used to live in ‘Professor’ streets where we started our life in the new environment nearly at the same time and had a lot of happy memories. Special thanks to Linfeng, Yong, Jiang, Yihui, Shuhong, Lilan, Jianbin, Tiantian and Wuyuan for all the parties, BBQs and travelling together. I am also thankful to the people who live in the ‘doctor’ building where I have been living for two years. I thank Xiaoyu, Mo Li, Xinyuan, Haiqiang, Meng Wei, Zhou Zhou, Yongjia, Jia Yan, Lei, Huajie, Zhang Lu and Wandong for all the dinners, jokes and even beers, although I always drink the least:). Meanwhile, my thanks go to Tian, Chu Jing, Ligu, Huayang, Bishang, Jacqueline, Wang Lu, Xiaojia, Shuanghou... for all your friendship.

My last but certainly not least thank goes to my family. I am grateful to have parents who support me in all my choice. They have always cared about my work and life a lot, shared my joys and sorrows, and pushed me forward. Dr. Yan Ni, it was amazing to meet you in Delft and we now build a small but a warming family, which I believe is the most dreamlike experience in my life. Thank you for your love, patience and encouragement, which make this journey easy and enjoyable.

About the Author

The author was born on the 10th September 1985 in Jurong, Jiangsu province of China. After graduating from the high school in June 2004, he moved to Nanjing to study at the Nanjing University of Aeronautics and Astronautics, Faculty of Mechanical and Electrical Engineering. The author obtained his B.S. degree in June 2008. With the granted University scholarship, he subsequently started his master study in the same Faculty under the supervision of Prof. dr. L. Yue. He graduated on June 2010 on the topic “Virtual Instrument for Vibration Analysis on Rotating Machinery”. This work has been published in the Journal of Mechanical Science and Technology for Aerospace Engineering.

In September, 2010 the author moved to the Netherlands to start his PhD research in TU Delft with the sponsorship of China Scholarship Council. His work was carried out in Aerospace NDT Lab, Structural Integrity and Composites group, under the supervision of Prof. dr. ir R. Benedictus and Dr. R. M. Groves. During the 4-years period of PhD study, the author conducted activities on optical instrumentation and its application on material characterization, which resulted in the present PhD dissertation.

On October 1, 2014, the author was appointed as a researcher in the Structural Integrity and Composites group. His work is focused on fiber-optic instrumentation for Non-destructive testing.

List of Publications

Journal

- [1] P. Liu, R. M. Groves, and R. Benedictus, "Optical coherence elastography for measuring the deformation within glass fiber composite," *Applied Optics*, 53(22), 5070-5077 (2014).
- [2] P. Liu, R. M. Groves, and R. Benedictus, "3D monitoring of delamination growth in a wind turbine blade composite using optical coherence tomography," *NDT & E International*, 64, 52-58 (2014).
- [3] P. Liu, R. M. Groves, and R. Benedictus, "Optical Coherence Tomography for the Study of Polymer and Polymer Matrix Composites," *Strain*, 50(5), 436-443(2014).
- [4] P. Liu, R. M. Groves, and R. Benedictus, "Signal processing in optical coherence tomography for aerospace material characterization," *Optical Engineering*, 52(3), 033201 (2013).

Conference Proceedings

- [1] P. Liu, R. M. Groves, and R. Benedictus, "Non-destructive evaluation of delamination growth in glass fiber composites using optical coherence tomography," *SPIE Smart Structures and Materials + Nondestructive Evaluation and Health Monitoring*, San Diego, US (2014).
- [2] P. Liu, R. M. Groves, and R. Benedictus, "Quality assessment of aerospace materials with optical coherence tomography," *SPIE Photonics Europe*, Brussels, Belgium (2012).

Conference Presentations

- [1] P. Liu, R. M. Groves, and R. Benedictus, "Optical coherence tomography of the front and back Faces of a wooden panel painting," Photon 14, London, UK (2014).

- [2] P. Liu, R. M. Groves, and R. Benedictus, "P. Liu, R. M. Groves, and R. Benedictus, "Optical coherence elastography for measuring the deformation and strain within glass fiber composite," 16th International Conference on Experimental Mechanics, Cambridge, UK (2014).

- [3] P. Liu, R. M. Groves, and R. Benedictus, "Optical coherence tomography for the study of polymer and polymer matrix composites," PhotoMechanics, Montpellier, France (2013).

- [4] P. Liu, R. M. Groves, and R. Benedictus, "Comparative analysis of digital demodulation approaches in optical coherence tomography," Photon 12, Durham, UK (2012).